Advancing Marine Renewable Energy Monitoring Capabilities

James Joslin

A dissertation
submitted in partial fulfillment of the
requirements for the degree of

Doctor of Philosophy

University of Washington

2015

Reading Committee:

Brian Polagye, Chair

Andy Stewart

Brian Fabien

Program Authorized to Offer Degree:
Department of Mechanical Engineering

University of Washington

Abstract

Advancing Marine Renewable Energy Monitoring Capabilities

James Joslin

Chair of the Supervisory Committee:
Dr. Brian Polagye
Department of Mechanical Engineering

Marine renewable energy is poised to contribute substantially to electricity generation over the coming decades. Marine resources are abundant, but generation options must harness these resources in an economically-competitive manner at acceptable environmental and societal cost. This economic pressure also applies equally to the environmental monitoring of early demonstration projects that is needed to reduce risk uncertainty and inform sustainable commercial developments. Consequently, a new suite of flexible, yet cost-effective, capabilities are required. This thesis presents applied research underpinning the development of the Adaptable Monitoring Package (AMP) and Millennium Falcon deployment vehicle, a system that can widen the aperture of the observable environmental interactions at wave and current energy sites.

The AMP and Millennium Falcon deployment vehicle provide a cabled, yet reconfigurable, instrumentation platform. By incorporating a flexible suite of instrumentation into a shrouded body with a single wet-mate connection, the AMP has the power and data bandwidth afforded to cabled deployments, but maintains the ease of recovery and redeployment associated with autonomous packages. Instrumentation included in the initial AMP implementation allows for monitoring of marine animal interactions, noise levels, current profiles, turbulence, and water quality in the near field of marine energy converters. The Millennium Falcon deployment vehicle, along with the docking station and launch platform, provides the

support infrastructure for deployment and recovery of the AMP in the energetic conditions that are typical of marine energy sites. Future potential for instrument integration and algorithm development makes the AMP well-suited to face the evolving needs of environmental monitoring around marine energy converters.

Development of the AMP and deployment system requires several pieces of new knowledge across the spectrum of ocean engineering. First, because the instrumentation mix defines the envelope for subsequent hydrodynamic optimization, the size and spacing constraints of the instruments needs to be defined. However, prior to this thesis, the utility of optical cameras to provide quantitative information in tidal energy environments had not been established, nor had the practical constraints on camera-light separation beneath the photic zone. Without this information, the benefits of including an optical camera system in an instrumentation package are uncertain. Consequently, the initial investigation focused on developing and evaluating the performance of a new stereo-optical camera system. With this sub-system defined, hydrodynamic analysis and optimization could proceed, through a series of laboratory experiments and vehicle simulations. These suggests that a deployment system built around the capabilities of a low-cost inspection class ROV can be effective, even in energetic environments.

Optical systems have been previously deployed around marine energy converters, but not used quantitatively and are anecdotally described as having poor endurance due to biofouling. However, optical systems can provide real-time stereographic imagery to detect and characterize targets in the near field (< 10 m) of marine energy converters in a manner more compelling and accessible than sonar imaging. Given public and regulatory concerns about the potential for marine energy converters to injure or kill marine animals, readily-interpreted and objective observations of the "last meter" of interaction are essential. A method for optimizing the stereo camera arrangement is given, along with a quantitative assessment of the systems ability to measure and track targets in three dimensional space.

Optical camera effectiveness is qualitatively evaluated under realistic field conditions (i.e., at a tidal energy site) to determine the range within which detection, discrimination, and classification of targets is possible. These field evaluations inform optimal system placement relative to a marine energy converter to satisfy the objectives of environmental studies. These tests suggest that the stereographic cameras will likely be able to discriminate and classify targets at ranges up to 3.5 m and detect targets at ranges up to, and potentially beyond, 4.5 m, provided that significant (e.g., 1 m) camera-light separation is maintained. Results are also presented from a four-month field test of the prototype stereo-optical camera system. A combination of passive (copper rings and ClearSignal antifouling coating) and active (mechanical wipers) biofouling mitigation measures are implemented on the optical ports of the two cameras and four strobe illuminators. Biofouling on the optical ports is monitored qualitatively by periodic diver inspections and quantitatively by metrics describing the quality of the images captured by cameras with different anti-fouling treatments. During deployment, barnacles colonized almost every surface of the camera system, excepting the optical ports with fouling mitigation measures. The effectiveness of the biofouling mitigation measures suggests that deployments of up to four months are possible for optical camera systems, even during conditions that would otherwise lead to severe fouling and occlusion of the camera optical ports. In combination, these studies demonstrate the quantitative benefit of optical camera systems and measures to extend their endurance, suggesting that they can serve a valuable role in an integrated instrumentation package.

At the level of the overall package, the critical question is whether an underwater vehicle that can be deployed without a specialized surface vessel is capable of performing the necessary operations to connect the AMP to a docking station on the seabed. Answering this question requires simulation of the system in turbulent currents, including control actions to maintain orientation and heading. However, the AMP and Millennium Falcon deployment vehicle have complex geometries that complicate the determination of the hydrodynamic

coefficients needed for simulation. The second part of the thesis focuses on the dynamic equations of motion for a generic underwater vehicle and methods to identify the hydrodynamic coefficients of interest during the vehicle design process. Computational fluid dynamic (CFD) simulations provide a fast and economical method for numerically estimating the lift and drag forces acting on the vehicle. However, experimental validation is required and traditional methods often require prohibitively expensive test facilities. Further, CFD simulations are not able to predict added mass, which can be significant for underwater vehicles. Free-decay pendulum experiments are used to experimentally verify the CFD results (ANSYS Fluent) for drag and quantify added mass. Results are presented for benchmark geometries (cube and sphere), followed by an analysis of a commercially available inspection class ROV for both a quarter-scale rapid prototype model and full-size vehicle. Comparison between analytical solutions, simulations, and experiments provides insight into the applicability of these methods and considerations for the effects of scaling and geometric simplifications.

With the hydrodynamic coefficients established, a dynamic stability analysis of the AMP and Millennium Falcon is presented. A commercial code (ProteusDS) simulates the dynamic response of the system using the previously determined hydrodynamic coefficients. Deployment operations are simulated with time-varying, three-dimensional current forcing generated from turbulent current data from a tidal energy site. Control forces required to maintain heading, surge velocity, and depth are compared to system thrust capacity. The maximum mean current for which deployment operations are possible is predicted and system stability evaluated. Sensitivity studies of the model input parameters demonstrate the importance of including turbulence in dynamic simulations and accurately characterizing hydrodynamic coefficients. These simulations predict that the system is deployable in mean currents up to 0.7 m/s, which is sufficient to conduct instrumentation package deployment at a tidal energy site.

Each of these sections contributes novel methods and results to the broader field of

ocean engineering, as well as establishing the foundation for the development of the AMP. Continued development of the AMP will investigate instrument integration to expand the monitoring capabilities of individual instruments and autonomous deployments to simplify system maintenance. Once deployed around marine energy converters, the AMP will enable a wide range of environmental studies that will advance the sustainable development of marine renewable energy.

TABLE OF CONTENTS

LIST OF FIGURES

LIST OF TABLES

ACKNOWLEDGMENTS

Thanking everyone who has helped and supported me over the last four years of graduate school is a daunting task. All of my friends, family and co-workers have helped lead me in some way to where I am today. Inevitably there will be important people that I neglect to mention here, but please accept my apologies and next time that we see each other, let me make it up to you with a beer. For now, if you choose to read on, hopefully you will see your influence in my work and have a better understanding of what has kept me busy at the university.

As a doctoral student, I have been exceptionally fortunate to have secure funding throughout my time at UW. The majority of my research has been supported by the US Department of Energy under DE-FG36-08GO18179-M001 and Public Utility District No. 1 of Snohomish County. The Mechanical Engineering Department and UW School of Engineering have also helped fund my time as a student through the Students First Fellowship, Purvis Family Fellowship, and Louis and Katherine Marsh Fellowship. Without this funding, I would not have enjoyed my time as a graduate student nearly as much as I have.

Brian Polagye, my faculty adviser and committee chair deserves my greatest thanks and recognition. When I first interviewed as a perspective student, Brian's own advisor, Dr. Malte told me that Brian was a rising star and that by working with him I could not help but succeed myself. Brian has been an excellent mentor providing a balance of support and freedom that is rare. At the same time, Brian has been a good friend, encouraging his students to maintain a work-life balance. I could not imagine having a better adviser for my PhD and look forward to working and climbing with Brian for many years to come.

Working with all of my committee members has been continually rewarding and a true

pleasure. Jim Thomson coordinated the field testing of the camera system and has been involved with my research since the beginning. Although he has not been as personally involved with the development of the AMP, Jim always has provided excellent advice and guidance. Andy Stewart has overseen the design and testing of the AMP and has been the most involved with my research (other than Brian) over the last two years. As a result of his recent involvement, Andy has also been instrumental in helping me investigate commercialization opportunities post graduation. Professor Brian Fabien was most helpful with the dynamic analysis in Chapter 5 but also helped to prepare me for the qualifying exam by teaching the dynamics class that I took my first fall at UW. Finally, I would like to thank Alex Horner-Devine for agreeing to be my Graduate Student Representative.

I would also like to acknowledge all of the members of the Northwest National Marine Renewable Energy Center and in particular the Marine Renewable Energy lab at UW. Chris Basset led the way as Brian's first PhD student and I look forward to his imminent return to Seattle. Teymour Javaherchi helped to get me started on the CFD analysis of the AMP. Rob Cavagnaro and Nick Stetzenmuler started in Brian's lab at the same time as I did and we all quickly became close friends. Trevor Harrison, Paul Murphy, Emma Dewitt-Cotter, Hannah Ross, Ben Strom, Dom Forbush, Caleb Bowman and Chris Fisher have all helped to grow the lab into a fun and exciting working community.

In addition to working with amazing students and faculty, I have also had the pleasure of working closely with many of the engineering staff in ME and APL. Michelle Hickner has been a great coffee and lunch buddy and, together with Bill Kuykendall, is always available to offer lab support in ME. At APL, Joe Talbert, Alex de Klerk, Ben Rush, Paul Gibbs, Trina Litchendorf, Tim McGinnis, and Chris Siani have all been instrumental in the design, fabrication, and field testing of all of these systems.

Outside of the University, there are many people that have helped guide me toward marine energy. In particular, I would like to thank all of the wonderful people that I have

had the privilege to sail with, especially Laura Nelson, Seth Murray, and Dusty Smith. I could never have imagined that signing up to sail with SEA in 2007 would have led me this far and I am eagerly awaiting my next opportunity to be back aboard the Seamans. To all of my adventure partners, I thank you for your inspiration and hope that we can get outside together again soon. Most of my achievements are due to the confidence and experience that I have gained from sailing, climbing, kayaking, and rafting.

My family has always offered unwavering support and guidance. One of the best parts of moving to Washington for graduate school has been how often I get to see them. Thank you Mom, Dad, Katy, John, Lisa, and Vijay.

Most importantly, I want to thank Virginia. She was my original inspiration to apply to graduate school and has supported me ever since. I do not tell her often enough how wonderful it has been to spend the last five years of our lives together. I hope that I can give you the same support you have given me for many years to come.

Chapter 1

INTRODUCTION

Concerns about climate change and limited energy resources have spurred development of renewable energy. With the energy portfolio of the United States dominated by petroleum, natural gas and coal (83% of primary energy) [USE, 2014] there is a desire to reduce carbon dioxide emissions from energy generation. In the state of Washington, the Energy Independence Act passed in 2006 requires 15% of electricity generation to come from renewable sources (excluding conventional hydropower) by the year 2020 [*Goltz et al.*, 2011]. While there are many forms of renewable energy currently under development, most are associated with resources that vary widely by region and climate. In the Pacific Northwest, marine energy in the form of the strong tidal currents in Puget Sound and ocean waves off the Pacific coast represent vast, unharnessed resources.

Marine renewable energy is an emerging industry that has seen substantial growth over the last decade. Offshore wind farms have been operating in the European North Sea since 2002 and continue to grow in size and reliability [*Henderson and Witcher*, 2010; *Perveen et al.*, 2014]. Similarly, deep water developments are beginning to take shape further offshore in Europe and the United States [*Breton and Moe*, 2009; *Failla and Arena*, 2015]. Although wave and tidal current technologies are not as advanced as wind, demonstration projects are entering the water around the world every year, with financing recently concluded for the first turbine array in the Pentland Firth, Scotland [*Cornelius et al.*, 2014]. Every project that is deployed provides valuable insight to the technology developers, regulatory agencies, and the public that help shape the industry. Over the coming years, the development of marine renewable energy promises to hold many challenges. These will be addressed most efficiently through the collaboration of the businesses in industry, researchers in academia,

and regulatory agencies in government.

Social and regulatory mandates require that the development of new resources, like marine renewable energy, be environmentally sustainable. At the same time, the cost of developing new resources must be minimized for the price of energy to compete with current sources. These cost restrictions apply both to the development of energy marine energy converters (MECs) and the monitoring methods infrastructure that supports them. Monitoring of early demonstration projects can provide information about the operation and performance of MECs and their interactions with the surrounding environment. Understanding these interactions and the changes that can occur in an environment due to the deployment of new technologies is crucial to sustainable development. By identifying negative interactions at the early stages of development, mitigation measures can be implemented prior to scaling up for commercial deployments.

Performing environmental monitoring of marine energy demonstration projects involves many engineering challenges due to the energetic conditions typical of tidal current and wave energy sites [*Polagye et al.*, 2014]. These locations are of interest because of their high resource intensity, but the loads generated by the currents and wave action pose a significant risk to expensive monitoring instrumentation. Corrosion and biofouling increase risk for long term deployments that are necessary to understand environmental changes. In addition, the difficulty of deploying and recovering instruments at these sites elevates the risk of losing instruments entirely. For all of these reasons, the development of new methods to increase instrumentation reliability and survivability, while decreasing the cost of monitoring are of general interest to the industry and regulatory agencies.

One example of environmental studies comes from Admiralty Inlet, Puget Sound, Washington, where autonomous platforms were deployed with an evolving suite of instrumentation from 2009 to 2013 [*Polagye and Thomson*, 2013]. These deployments collected data on currents, ambient noise levels, water quality, and marine animals in the inlet as a background characterization for a proposed tidal energy demonstration project. Similar platforms have been deployed to characterize sites off the Oregon coast for the Pacific Marine Energy Center

and internationally. In Orkney, Scotland the Flowbec 4-D sonar platform has been deployed for monitoring at tidal and wave energy test sites [*Williamson et al.*, 2015]. These autonomous platforms allow for rapid deployment and recovery but are generally limited by the power and data storage requirements of the instruments. Several cabled instrumentation platforms are in development to increase instrumentation bandwidth and allow real time monitoring. These include an instrumentation "pod" deployed at the European Marine Energy Center (EMEC) [*EMEC*, 2013] and the Fundy Advanced Sensor Technology (FAST) platform under construction for deployment in the Bay of Fundy, Canada [*Daborn et al.*, 2014; *Steiner-Dicks*, 2014]. Although these platforms are cabled to shore, the cable must be connected on the surface which complicates recovery and redeployment. While these platforms have demonstrated the capabilities of current instrumentation, they have similarly shown the need for new innovative instrumentation and deployment methods.

The systems described in this thesis are developments in response to these identified needs. As a result, the research described in the following chapters spans several levels of the system design (e.g., component instrumentation design to overall system hydrodynamics) and mechanical engineering topical areas (e.g., optics and biofouling to fluid dynamics). This interdisciplinary breadth is a necessity for advancing marine renewable energy instrumentation.

A detailed motivation for each element of this research is presented in the introduction of the corresponding section of the thesis. Overall, development of these systems is motivated by the instrumentation needs for conducting environmental monitoring at marine energy sites. To establish this understanding, Chapter 2 provides a brief background into the potential environmental impacts of marine renewable energy, the instrumentation used to monitor for these impacts, and the areas where further development is required. Much of the information in this chapter is summarized from two expert workshops [*Polagye et al.*, 2011] and [*Polagye et al.*, 2014].

Chapter 3 provides system descriptions for the components and capabilities of the instrumentation system and deployment vehicle shown in Figure 1.1. The primary system

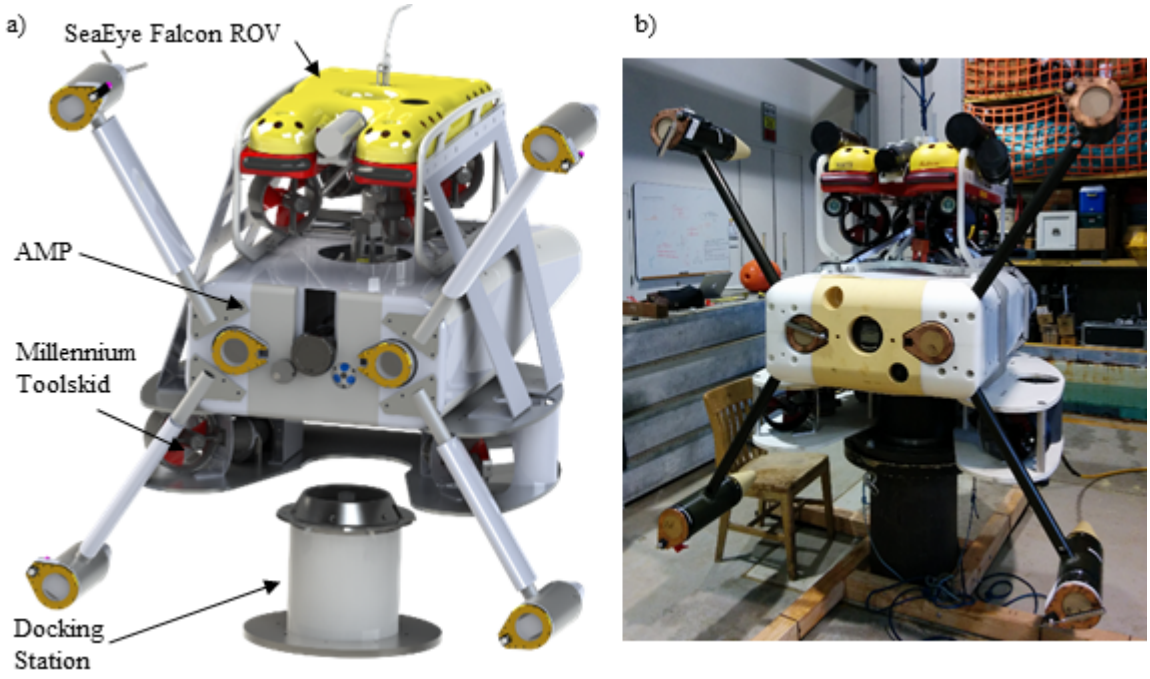

Figure 1.1: AMP and Millennium Falcon deployment vehicle from the (a) conceptual solid model and (b) physical prototype

is referred to as the Adaptable Monitoring Package, or AMP, and is an integrated instrumentation package that houses a flexible suite of monitoring instrumentation in a single streamlined body. When deployed for long-term monitoring, the AMP is cabled to shore via a wet-mate connector that provides gigabit data bandwidth and up to one kilowatt of power. This data and power connection allows real-time operation of instruments to monitor for marine animal interactions, noise levels, current profiles, turbulence, and water quality. By incorporating a wet-mate cable connection into a custom docking station, the AMP gains this high bandwidth while maintaining the ease of recovery associated with autonomous platforms. The Millennium Falcon deployment vehicle is being developed concurrently with the AMP as a means to recover and redeploy the AMP from the docking station for instrument maintenance and reconfiguration. Built around a low-cost "inspection-class" ROV, the system is deployable from an unspecialized research vessel. The custom "Millennium" tool skid adds the thrusters, actuators, cameras, and lights needed to deploy the AMP in the

energetic currents of marine energy sites. Both the AMP and deployment ROV are designed to enable a broader range of monitoring capabilities at acceptable cost. The information presented in Chapters 2 and 3 has been presented and published in the proceedings of the *5th International Conference on Ocean Energy 2014* in Halifax, Nova Scotia, Canada, and is cited as:

> Joslin, J., B. Polagye, and A. Stewart, Development of an Adaptable Monitoring Package for Marine Renewable Energy, *5th International Conference on Ocean Energy (ICOE)*, Halifax, Nov. 3-6, 2014.

The least-defined AMP component at the initiation of this research was the stereo-optical camera system described in Chapter 4. Subsystem specifications are needed to establish the overall constraints on instrumentation package size and orientation. Since stereo-optical monitoring has not been used as a quantitative tool in prior marine energy projects, development and evaluation of this subsystem is a necessary precursor to evaluating and optimizing the AMP and Millennium Falcon's hydrodynamic performance (Chapter 5). The development and evaluation of this system in presented in two parts, mirroring its publications. First, the development and optimization of the stereo-optical camera system is presented in Section 4.1. This system uses off the shelf components in a configuration that provides compelling capabilities to detect, discriminate, and characterize marine animal behavior at marine renewable energy sites. Laboratory experiments and field trials are used to optimize the stereographic layout of the system and evaluate the system's capabilities at a potential marine energy site in Admiralty Inlet, Puget Sound, WA. This work is published in the *SPIE Journal of Applied Remote Sensing*:

> Joslin, J., B. Polagye, and S. Parker-Stetter, Development of a stereo-optical camera system for monitoring tidal turbines, *SPIE J. Appl. Remote Sens.*, 8(1), 083633, doi:10.1117/1.JRS.8.083633, 2014.

The second part of the camera system development, presented in Section 4.2, describes the biofouling mitigation methods implemented on the camera optical ports. To test the system's endurance in the marine environment, the prototype camera system is deployed for four months at Sunset Bay, Puget Sound, WA with a combination of passive and active biofouling mitigation measures. Throughout the deployment, a novel approach is used to monitor and quantify the biofouling of the camera optical ports and degradation of image quality over time. This work is published by the *Marine Technology Society Journal*, and is cited as:

> Joslin, J. and B. Polagye, Demonstration of biofouling mitigation methods for long term deployments of optical cameras, *MTS Journal*, 49(1), 88-96, 2015.

With the instrumentation spacing constraints determined, the next question in the system development is if the AMP can be deployed by a low-cost vehicle. This depends on whether system hydrodynamic performance can be optimized to the point that turbulent currents can be overcome during system deployment without relying on "work-class" ROV thrust capacities. Chapter 5 covers the hydrodynamic analysis of the AMP and Millennium Falcon deployment and is divided into two sections. Section 5.1 is a development of the methodology used to estimate the hydrodynamic coefficients of a generic underwater vehicle. Computational fluid dynamics simulations are combined with free-decay pendulum experiments to measure the added mass and drag of the vehicle. These methods are used to analyze the Falcon ROV to demonstrate their applicability to the general field of marine robotics. Hydrodynamic coefficients for the full system are used to inform the system design and evaluate options prior to construction of the first full-scale system. This work is in review for publication in the *Journal of Ocean Engineering* and will be cited as:

> Joslin, J., B. Polagye, and A. Stewart, Hydrodynamic coefficient analysis of an open framed underwater vehicle, *J. Ocean Eng.*, in review.

To complete the hydrodynamic analysis of these systems, Section 5.2 presents a dynamic stability analysis during deployment operations in turbulent currents. Dynamic simulations, using previously determined hydrodynamic coefficients, are performed using a commercial code (ProteusDS, Dynamic Systems Analysis Ltd., Victoria, BC, Canada) and time-varying, three-dimensional currents. Turbulent current data from a compliant mooring deployment in Admiralty Inlet, Puget Sound, WA [*Thomson et al.*, 2013] is used to generate current forcing representative of a potential tidal energy site. Simulated controller actions determine the thrust force required to maintain heading, headway, and depth. An operational limit for deployments is predicted as a function of the mean current velocity by comparing the required control force to the vehicle thrust capacity. Sensitivity studies investigate the importance of model parameters to predicting this operational limit. In practice, this limit will be used to choose dates and times for deployments of the AMP at marine energy sites when hydrodynamic conditions are favorable for operations. This work is in preparation for submission to the *Journal of Applied Ocean Research* and will be cited as:

> Joslin, J., B. Polagye, A. Stewart, and B. Fabien, Dynamic Simulation of a Remotely-operated Underwater Vehicle in Turbulent Currents for Marine Energy Applications, in preparation.

The hydrodynamic conditions used in the analysis presented in Chapter 5 are developed from tidal current and wave energy site data in Appendix A. The analysis of data from Admiralty Inlet, Puget Sound, Washington and the PMEC North Energy Test Site off of Newport, Oregon provides loading cases for tidal and wave energy sites, respectively. Initial design optimizations performed with CFD simulations are described in Appendix B. These steady-state simulations are used to evaluate and compare loads on design features in uniform flows.

Chapter 6 presents a summary of the contributions made in each section and a look into the future environmental monitoring potential created by the AMP. The methods developed

are widely applicable across marine industries and will contribute to the specific development of an environmental monitoring system for marine renewable energy.

Chapter 2

BACKGROUND: ENVIRONMENTAL MONITORING FOR MARINE RENEWABLE ENERGY

2.1 Introduction

To understand the need for environmental monitoring of marine energy converters, one must first understand the environmental impacts of concern. Recent workshops [*Polagye et al.*, 2011, 2014] have prioritized research areas by the risk, significance, and uncertainty of potential impacts and identified the instrumentation suitable for evaluating those impacts. *Polagye et al.* [2014] describes the need for advances in current instrumentation technologies along with the supporting infrastructure. This chapter summarizes the findings of these workshops as a motivation for this exam document.

2.2 Potential Environmental Impacts

Environmental effects of marine energy converters (MECs), such as wave or tidal energy converters (WECs or TECs, respectively), can be described in terms of interactions between stressors and receptors. Stressors are the factors that occur due to the installation and operation of a MEC and receptors are the elements of the marine environment that are affected by stressors [*Boehlert et al.*, 2008; *Boehlert and Gill*, 2010; *Polagye et al.*, 2011]. Stressor-receptor interactions considered by *Polagye et al.* [2011] for TECs are shown in Figure 2.1 and ranked as a function of the significance that the potential impact would have if it were to occur, the probability of the impact occurring, and the current level of uncertainty surrounding that impact. Together, these first two factors define the risk associated with the potential impact and the current level of uncertainty helps to determine the priority level for study. The high priority potential impacts observable at the pilot scale include dynamic

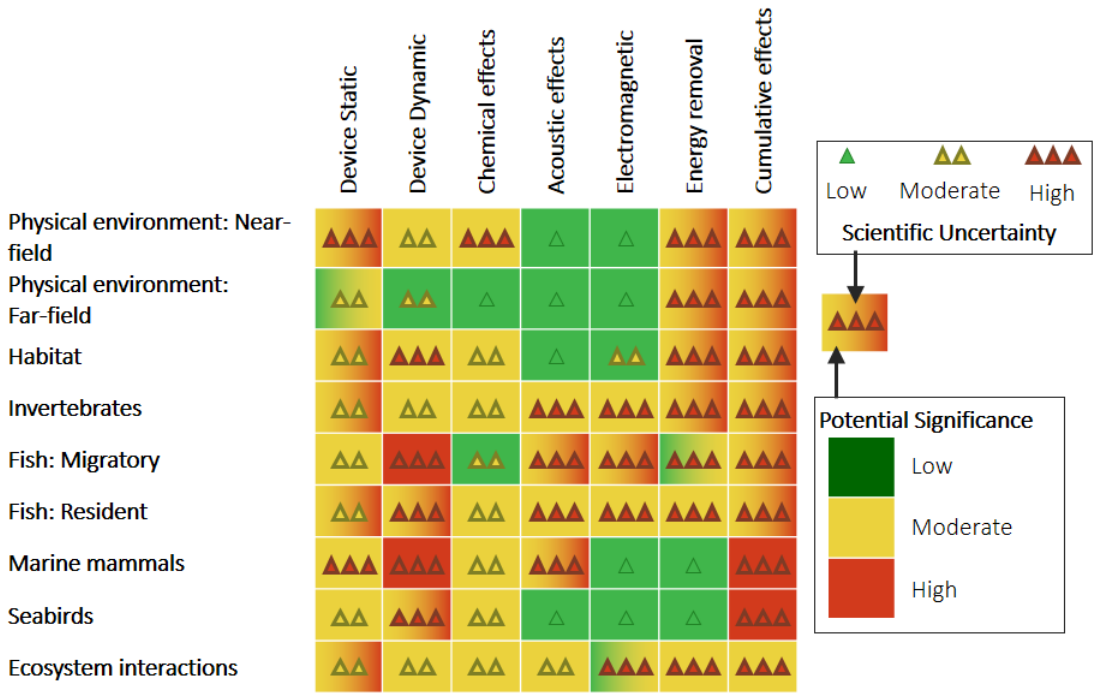

Figure 2.1: Potential environmental impacts of tidal energy converters ranked by their significance and uncertainty [*Polagye et al.*, 2011]

interactions between marine animals and MECs (e.g., collision, strike, and evasion), reef effects of MECs, and behavioral changes caused by converter sound.

The objective of environmental monitoring, as discussed in *Polagye et al.* [2014], is to collect sufficient information about an environmental risk to either identify and mitigate impacts or responsibly "retire" the risk by proving it insignificant. Decisions regarding the handling of these risks are made by regional or national resource agencies based on the scientific information available and regulatory mandate. The potential of "retiring" risks would allow monitoring missions to evolve over time and could reduce the cost of MEC deployment.

2.3 Current Monitoring Instrumentation and the Desired Needs for Marine Energy

Capabilities of currently available instrumentation to satisfy monitoring goals around marine energy sites, along with the desired advances for future research, are discussed in *Polagye et al.* [2014]. The most common instruments currently used to conduct environmental monitoring include acoustic Doppler current profilers and velocimeters, optical and acoustical cameras, multi-beam sonars, hydrophones, fish tag receivers and cetacean click detectors. Deployment methods are generally site specific but may be from a surface or bottom mounted platform and may last for a few hours up to several months. The lack of standardized monitoring methods often makes comparison of site and technology data difficult.

Collecting sufficient information to monitor for risks with low probability of occurrence but severe outcomes (e.g., animal mortality due to collision) is the greatest challenge to current instrumentation. Theoretically, the most expedient approach to monitoring for these rare interactions is through spatially comprehensive and temporally continuous data collection. Even if the cost of instrumentation required for spatially comprehensive monitoring is neglected, the volume of data produced through this type of approach would likely result in a "data mortgage", whereby data are collected at a rate faster than they can be processed. For monitoring plans that require species level taxonomic classification of marine animals (e.g., optical or acoustical imaging), this problem is particularly acute. Neither pure hardware nor pure software solutions are likely to be practical, but integrated instrumentation packages may be a viable approach [*Polagye et al.*, 2014]. For example, an instrument with omnidirectional, real-time target detection capabilities (e.g., a localizing hydrophone array listening for marine mammal vocalization) could be used to trigger an instrument with higher-bandwidth and lower-aperture that requires archival data collection for interpretation (e.g., optical camera). While some instrument integration is currently in development, many future possibilities exist which suggests that instrumentation packages should be adaptable to support a wide range of instrument combinations.

One benefit of deploying monitoring instrumentation in the vicinity of MECs is the availability of the converter's power export cable to shore. Such cables often also contain one or more communication fibers. If the instrumentation can be connected to the export cable, ancillary circuits can provide sufficient power and data bandwidth to operate a wide range of instruments that would be otherwise infeasible for autonomous deployments. Through the shore connection, instruments can be operated in real time with targeted sampling and data processing to meet monitoring plan objectives. While this addresses the power and data bandwidth limitations of traditional autonomous deployments, maintenance of the instrumentation becomes more difficult. For experimental monitoring technologies, ease of maintenance is particularly important due to the high probability of malfunction or need for adjustment after relatively short periods (e.g., several weeks between maintenance interventions). Possible maintenance options for cabled instrumentation and their respective challenges include:

- *Diver intervention*: extremely short working windows at depth; human safety concerns; high cost

- *ROV intervention*: short working windows; difficult to make more than minor modifications once deployed

- *Converter recovery*: high cost (up to $1 M per intervention for some site-converter combinations); operational risk of converter damage

- *Subsea winch with umbilical and slip ring* (enable package maintenance on surface without disconnecting from converter): high cost; winch failure during recovery/ redeployment can lead to catastrophic system failure as metocean conditions change

- *Instrument package recovery with wet mate connection*: mating connection complicates deployment operations; high cost of wet mate connector

2.4 Conclusion

Monitoring of early marine energy demonstration projects has the potential provide valuable information and inform sustainable development. While currently available instrumentation can address some of the regulatory concerns, new methods are needed to reduce "data mortgages" and associated costs. Integrating instrumentation may allow for the development of target tracking and data processing algorithms that would reduce the quantity of data produced. Cabling instrumentation packages to shore would enable higher power and data bandwidths to increase monitoring efficiency. Ultimately, these packages must be easily recoverable, however, to allow for regular maintenance and reconfiguration of instrumentation.

Chapter 3

BACKGROUND: THE ADAPTABLE MONITORING PACKAGE AND MILLENNIUM FALCON DEPLOYMENT SYSTEM

3.1 Introduction

In response to the instrumentation needs discussed in Chapter 2, NNMREC researchers are developing two systems to enhance capabilities and reduce the cost of environmental research: 1) the Adaptable Monitoring Package (AMP) to integrate a flexible suite of instrumentation into a single, streamlined body and 2) the infrastructure to allow an inspection class remotely operated vehicle (ROV) and custom tool skid to deploy the AMP at marine energy sites. Figure 3.1 shows the current design model of the AMP and the deployment system, a SeaEye Falcon ROV and custom tool skid referred to as the "Millennium." With a docking station incorporated into the MEC design or located near by, the AMP employs a "plug and socket" architecture, whereby the AMP ("plug") mates with the docking station ("socket") with a power and data connection to shore. Over the lifetime of a project, only the "socket" remains in the water while the "plug" (AMP) is readily maintained or reconfigured at a shore facility. The AMP conceptual design lends itself to rapid deployment in a precise manner, reliable connection to shore power and data, and recovery with similar facility all of which minimize the duration of a maintenance operation and surface vessel operational costs. This approach captures both the benefits of a cabled connection to shore and the adaptability of an autonomously operating package.

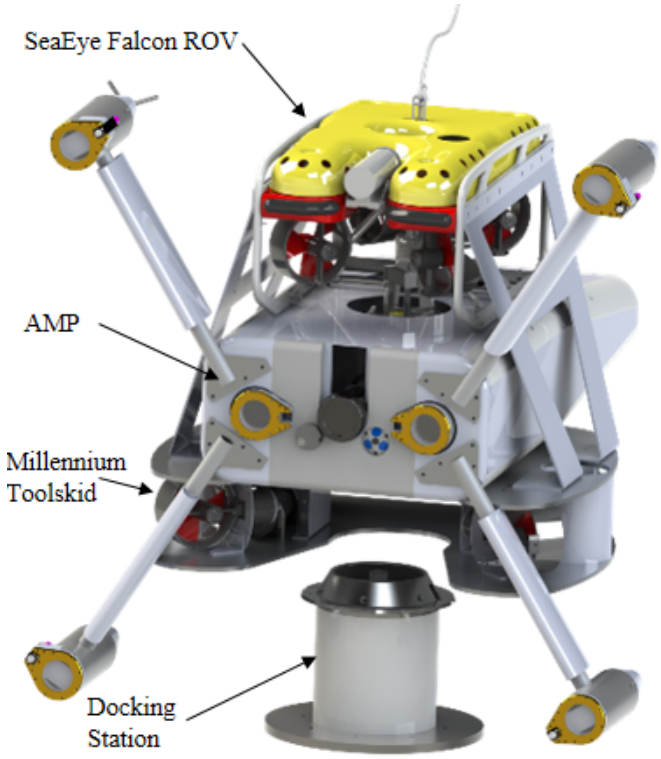

Figure 3.1: AMP and Millennium Falcon Deployment ROV

3.2 System Component Descriptions

Descriptions of the AMP, deployment ROV, docking station and launch platform, and operational concepts for deployment and recovery are provided in the following section.

3.2.1 The Adaptable Monitoring Package

Instrument integration has the potential to expand the capabilities of individual sensors while reducing the costs associated with environmental monitoring [*Polagye et al.*, 2014]. As a platform, the AMP allows for a flexible suite of instrumentation by providing up to 1 kW of power and 2 Gbps of data bandwidth (depending on the capacity of the MEC export cable). The instruments incorporated into the initial AMP design are listed in Table 3.1 with their internal layout in the AMP structure shown in Figure 3.2. Most of these instruments,

Instrument	Manufacturer and Model	Monitoring Capabilities	Layout Constraints
Stereo-Optical Camera System	Integrated System – UW Custom, Cameras – Allied Vision Tech., Strobes – Excelitas	Near-field marine animal interactions with turbine with potential for species-level identification	0.5 m camera separation, 1 m strobe/camera separation, must face region of interest[1]
Acoustical Camera	BlueView P900-2250	Near-field marine animal detection with capabilities for optical camera triggering	Must face region of interest
Hydrophone Array	Integrated System - UW Custom, Digital Hydrophones - OceanSonics iCListen	Marine mammal localization and converter sound monitoring	$\geq$1 m separation between hydrophone elements
Acoustic Doppler current profiler	Nortek Aquadopp 1 MHz	Near-field current profiling to study inflow and wake	Must face towards profile of interest
Acoustic Doppler velocimeter	Nortek Vector	Near-field current point measurement to study inflow and wake turbulence	Sensor head unobstructed
Water quality	SeaBird 16+ v2 CTDO	Water quality and property observations	Unobstructed intake
Cetacean click detector	Chelonia C-POD	Harbor porpoise click detection	Exposed hydrophone element
Fish tag receiver	Vemco VR2W	Tracking of tagged fish	Exposed hydrophone element

[1] Optimal separation and required camera/strobe separation were developed through the research described in Chapter 4

Table 3.1: Monitoring instrumentation incorporated in the initial AMP design

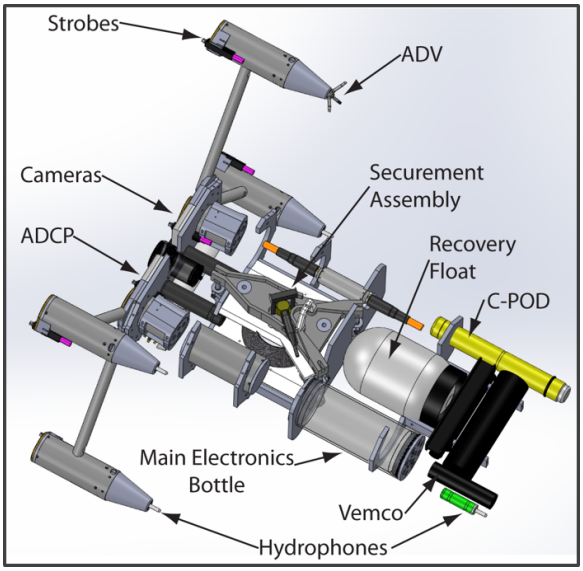

Figure 3.2: Representative AMP internal component layout with fairings and frame removed

with the exception of the stereo-optical camera system, are commercially available. The development and initial evaluation of the camera system are described in *Joslin et al.* [2014a]. The leading constraints on the AMP layout are due to the minimum separation distance between hydrophones in the localizing array and between the strobes and optical cameras. Practical experience suggests that time-delay-of-arrival (TDOA) localization methods for mid- and high-frequency cetacean vocalizations will be most effective with at least one meter separation between the hydrophone elements in either a tetrahedral or three-dimensional "L" configuration [*Wiggins et al.*, 2012]. Similarly, camera-strobe separation of one meter has been shown to reduce backscatter from biological flocculent [*Joslin et al.*, 2014a; *Jaffe*, 1988]. Both the optical and acoustical cameras, as well as other active acoustic instruments (e.g., echosounder, Doppler profiler), must also be oriented to face the regions of interest. The remaining instruments generally require a clear line of site for a receiving element (e.g., C-POD click detector, Vemco fish tag receiver) or pump intake (e.g., CTDO) and do not have strict separation or directional requirements. Each of these instruments has been integrated into the structure of the AMP in a way that respects their layout and orientation constraints

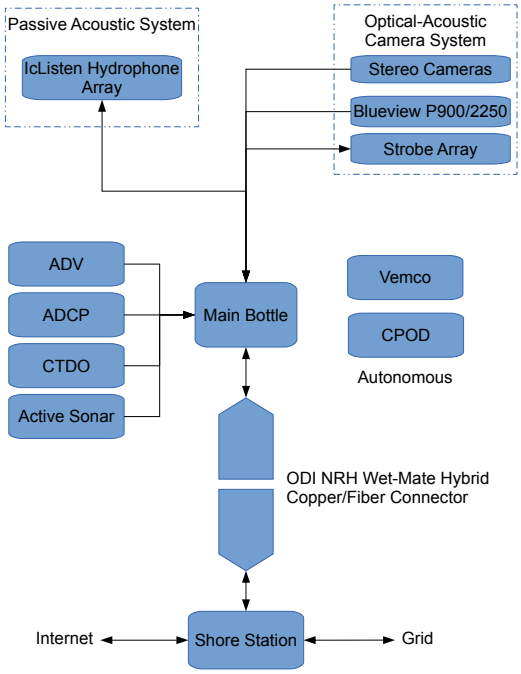

Figure 3.3: AMP system architecture while docked

while optimizing hydrodynamic performance and maintaining a favorable distribution of mass and buoyancy.

The power and communications architecture for the AMP, shown in Figure 3.3, is similar to that employed by cabled ocean observatories such as Neptune Canada [*Barnes et al.*, 2007, 2011] and the Regional Scale Nodes [*Cowles et al.*, 2010]. All of the instrumentation in the AMP is either autonomous (e.g., the C-POD and Vemco), or connected to the central node that converts power and data for the cabled connection to shore. Power is converted in the main bottle from the 48 VDC supply to switchable instrument connectors at 12, 24, and 48 VDC. All data from instruments is converted and aggregated to two Gigabit Ethernet channels from native Ethernet or network addressable serial converters. The wet-mate hybrid copper/fiber connector (ODI NRH) is housed at the center of the docking station and is the link between the AMP and shore power and data.

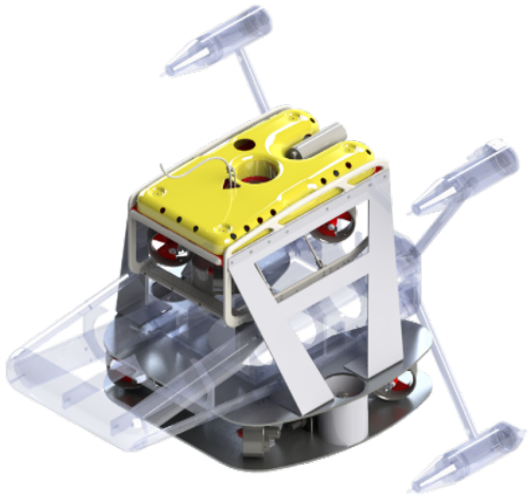

Figure 3.4: Millennium Falcon deployment ROV

Combining instrumentation into a single shrouded body simplifies maintenance and reduces the drag loads from currents. The mechanical structure of the AMP consists of a streamlined outer hull over modular internal bulkheads. These bulkheads support the loads on the external shrouds while providing mounting surfaces for the instruments. Instrumentation layout, and thereby control of the mass and buoyancy distribution is adaptable due to the modularity of this internal structure. At the center of the AMP body is the docking station securement system and wet-mate connector. The securement assembly consists of conical platform for alignment and three over-center clamps that are engaged by a centrally-located actuator on the ROV. By changing the orientation of the wet-mate connector and securement system alignment key, the AMP can be deployed in orientation angle of 0°, 50°, or 90° relative to the docking station to achieve different viewing angles of a MEC or surrounding ocean.

3.2.2 Millennium Falcon Deployment ROV

The commercially available SAAB SeaEye Falcon inspection class ROV forms the base of the AMP deployment system. Weighing approximately 60 kg in air with a payload capacity of 14 kg and having dimensions of 1 m long by 0.6 m wide by 0.5 m tall, the Falcon represents a balance of cost, performance, and ease of customization. The four vectored horizontal thrusters and single vertical thruster are capable of generating 50 kg of force in the surge direction and 13 kg of force in the heave direction. The initial hydrodynamic analysis, discussed in detail in Chapter 5, shows that the Falcon alone lacks sufficient thrust to deploy the AMP in the currents likely to be encountered at marine energy sites. In collaboration with SeaView Systems, a custom tool skid, shown in Figure 3.4, was developed that includes additional thrusters (four additional horizontal, one additional vertical), actuators, and cameras to meet the needs for deployment of the AMP.

The SeaView Systems power and communication distribution node operates in a Master/Slave configuration with the Falcon's surface control unit. Pilot commands for the Falcon are transmitted via a RS485 serial bus to all of the vehicle's thrusters, actuators, cameras, and lights. At the heart of the Millennium is SeaView's thruster control board, which receives the Falcon commands and emulates them to control the appropriate thrusters on the tool skid. These additional thrusters are mounted in a mirrored configuration to the Falcon but within the structure of the tool skid, which is connected to the Falcon but beneath the AMP during deployments. With thrusters positioned both above and below the AMP, the center of thrust is collocated with the center of pressure from drag. In this manner, the ten thrusters on the Millennium Falcon operate on the same commands as the Falcon alone while minimizing pitch and yaw moments from drag forces during maneuvers. Preliminary tank testing indicates that this configuration is able to produce 70 kg of forward/reverse thrust, 60 kg of lateral thrust, and 23 kg of vertical thrust.

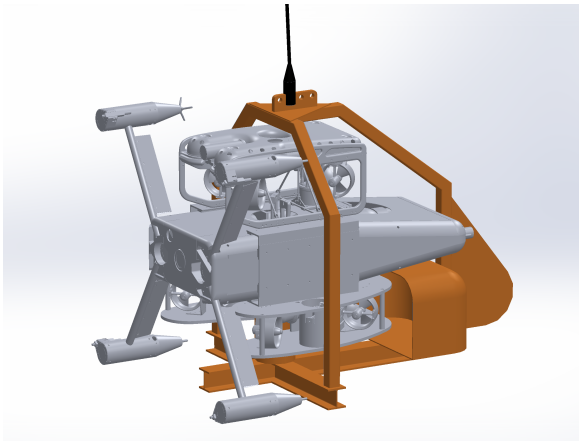

Figure 3.5: Launch platform for deployment to docking station depth

3.2.3 Launch Platform and Docking Station

A launch platform for the AMP and deployment ROV increases the acceptable current range during deployments by decreasing the umbilical drag that must be overcome by the ROV. Figure 3.5 shows the current design model of the launch platform that will deploy the system from a surface vessel to the approximate depth of the docking station. This platform is supported by a load-bearing umbilical. A junction bottle on the platform connects the power and data lines from the load bearing umbilical to a neutrally buoyant ROV umbilical. As the system drives off the launch platform, this second umbilical pays out from a passive tether management system on the platform so that the ROV is not exposed to drag on the load-bearing umbilical.

The docking station for the AMP, shown in Figure 3.1, is designed to facilitate docking and reduce operational time in adverse conditions. On approach, the ROV is guided into alignment with the docking station by cameras, lights, and an ultra-short baseline (USBL) positioning system on the Millennium tool skid. The horseshoe shape of the tool skid is used to achieve a coarse alignment with the vertical axis of the docking station. Fine alignment, required for the wet-mate connector, is achieved by the conical shape of the dock for the

vertical axis and a keyway for the system angle. Securement clamps on the AMP are engaged by a linear actuator on the Falcon ROV and designed to withstand the hydrodynamic forces generated by peak loads (Chapter 5). Mating of the AMP's power and data connection is performed by a second linear actuator on the ROV and monitored by a vertically oriented camera.

3.2.4 Deployment and Recovery Operations

Deployment of the AMP with the Millennium Falcon ROV is possible from small vessels with basic station keeping capabilities, an A-frame or crane with appropriate load capacity, and 220 VAC power availability. Figure 3.6 shows a basic diagram of the systems during a deployment operation. The operational steps for deployments are as follows:

- Prepare AMP instrumentation and docking clamps for desired deployment orientation. Load AMP and Millennium Falcon on to launch platform.

- Maneuver ship into position down current from docking platform and confirm that currents are within an acceptable range for ROV operations.

- Lower the system to the depth of the docking station on the launch platform and connect power and fiber on the winch for ROV operation through the load bearing umbilical (this order of operations obviates the need for a slip ring to support ROV operations).

- Confirm separation distance and orientation of the system with the docking station using a USBL, disengage from the launch platform and drive towards docking station.

- Maneuver into coarse alignment using Millennium docking features and forward facing cameras.

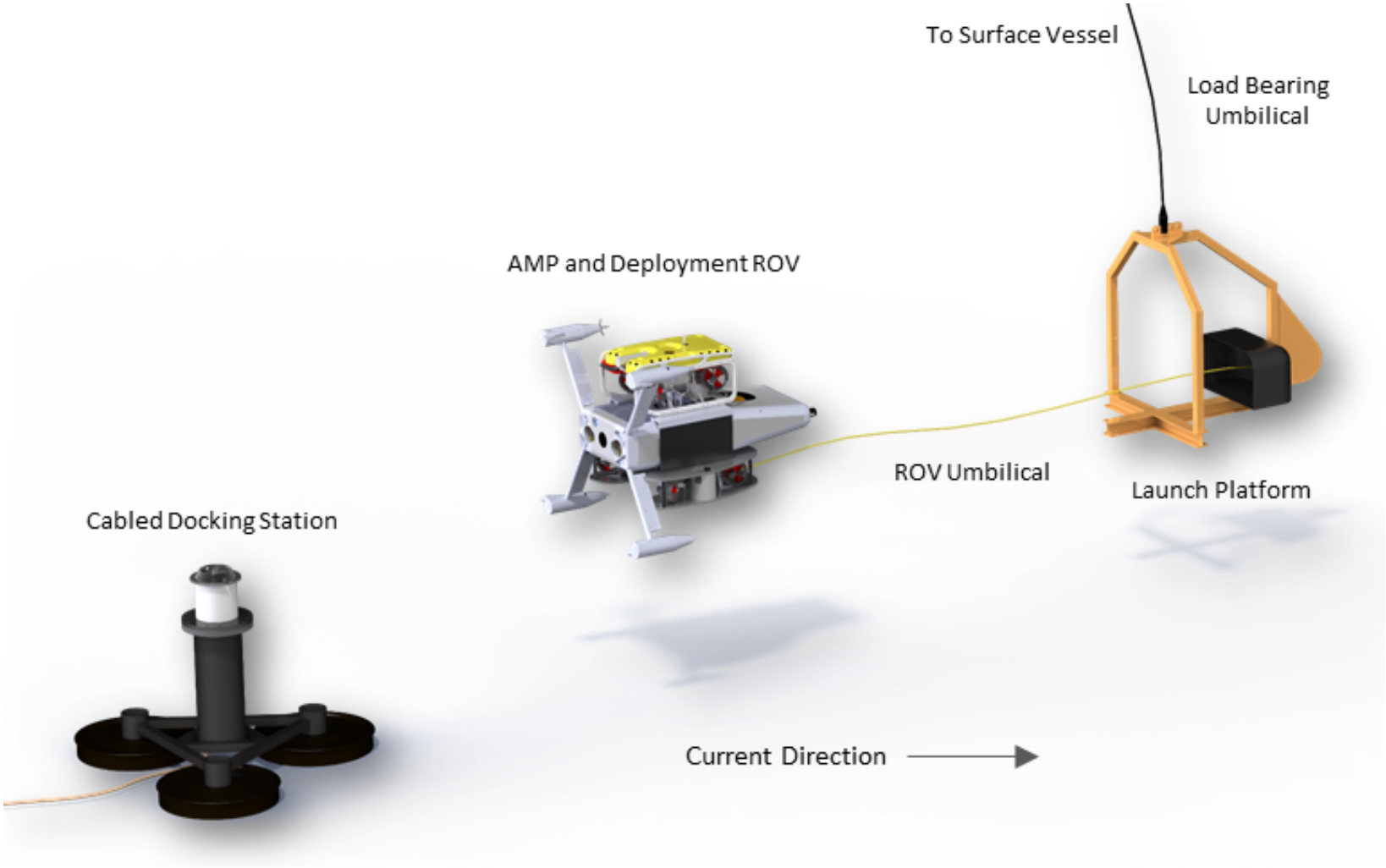

Figure 3.6: Diagram of the Millennium Falcon with the AMP during a deployment

- Thrust down onto the docking cone and partially engage the docking clamps in the initial “soft-lock” position.

- Rotate the ROV for angular alignment with the keyway on the docking station and engage docking clamps in the final “locked” position.

- Plug in wet-mate connector and bring the AMP online from a shore station to confirm instrument operations.

- Disengage the ROV from the AMP and return to surface for recovery.

- Disconnect ROV power and fiber on winch to recover the launch platform.

Recovery operations for the AMP are designed around an autonomous system, leaving ROV intervention as a backup. The operational steps for recovery are as follows:

- Maneuver recovery vessel into position and confirm the current range and direction.

- Power down AMP systems.

- Trigger the acoustic release of recovery float and messenger line from the AMP.

- Retrieve recovery float and place tension on the messenger line to sequentially disengage wet-mate connection and docking clamps.

- Raise the AMP to the surface for recovery.

These operating procedures are designed to minimize the time requirement for deployment and the risks associated with malfunctions.

3.3 Conclusion

The AMP and Millennium Falcon have the potential to enable a new level of environmental monitoring of marine energy converters. As a cabled system, the AMP provides real-time information from instruments with high power and data bandwidths. The AMP design allows for the integrated instrumentation to be customized for specific monitoring missions. By integrating a wet-mate connection into the AMP, the system maintains the ease of deployment and recovery associated with autonomous systems. These deployment and recovery operations take an innovative approach by using an "inspection-class" ROV and docking station to reduce the cost and time of maintenance. Development of these systems has required research into both the subsystems and of the overall package, as presented in the following chapters.

Chapter 4

DEVELOPMENT OF THE STEREO-OPTICAL CAMERA SYSTEM FOR NEAR-FIELD MONITORING OF HYDROKINETIC TURBINES

4.1 Design, Testing, and Optimization

The text of the following chapter was published in the *SPIE Journal of Applied Remote Sensing* in May, 2014. With the exception of reformatting the text, no changes were made to the content of the original article. The citation for the published document is as follows:

Joslin, J., B. Polagye, and S. Parker-Stetter, Development of a stereo-optical camera system for monitoring tidal turbines, *SPIE-J. Appl. Remote Sens., 8(1)*, 083633-1-25, 2014.

4.1.1 Introduction

The energy in fast moving tidal currents is a potential source of renewable, predictable electricity. Tidal turbines harness tidal currents in a manner analogous to wind turbines. Benefiting from the lessons learned in the development of wind energy, single-turbine demonstration projects with rated electrical capacities exceeding 1 MW have been successfully deployed in tidal races [*Polagye et al.*, 2011]. However, before large-scale utilization of tidal current resources may occur, operation of turbines must be proven to be not just technically feasible, but economically viable, environmentally benign, and socially acceptable.

Potential environmental impacts associated with tidal turbine operation have been evaluated by several groups [*Polagye et al.*, 2011; *Cada et al.*, 2007; *Boehlert and Gill*, 2010; *Inger et al.*, 2009; *Witt et al.*, 2012]. However, the frequency with which the most significant potential impacts will actually occur is uncertain. Resource agencies have expressed particular

interest in understanding the frequency and nature of close-range (defined as 1-2 diameters of the turbine rotor) interactions between marine animals (i.e., fish, large invertebrates, marine mammals, and diving seabirds) and tidal turbines. Possible interactions include collision/strike with the moving rotor, attraction due to the foundation as an artificial reef, and avoidance due to pressure fluctuations or sound. To date, there have been several attempts to collect this information with active acoustics (e.g., sonars or echosounders). These have provided valuable information about the behavior of fish in the vicinity of turbines [*Viehman and Zydlewski*, 2014; *Williamson and Blondel*, 2012] but have reported difficulties achieving a fine level of taxonomic classification or characterizing the nature of interactions with the turbine rotor itself.

At present, there are several dozen tidal turbine designs in various stages of development. *Khan et al.* [2009] provides an overview of proposed technologies and *Polagye et al.* [2011] includes case studies of several demonstration projects. While turbine technology has yet to converge on a single archetype comparable to the three-bladed axial flow wind turbine, a trend has emerged in recent years for utility-scale tidal turbines. The rotors are dominantly axial flow designs (i.e., the axis of rotation is parallel to the direction of water motion) and utilize two to three rotor blades. However, it has been noted [*Salter*, 2012] that large-scale utilization of tidal current resources may require devices with fundamentally different rotor topologies (e.g., vertically-oriented cross flow rotors). To achieve rated electrical capacities greater than 1 MW, turbine rotors for axial flow commercial demonstration systems are on the order of 20 m in diameter. Hub heights (i.e., height of axis of rotation about rotor hub) relative to the seabed depend on the foundation and mooring technology (monopiles, gravity foundations, or jacket structures). In general, current intensity increases away from the seabed, but foundation cost and complexity for bottom-anchored turbines also increases with hub height [*Kawase et al.*, 2011]. Consequently, depending on the turbine technology and deployment site, turbines can either operate entirely within the photic zone or at depths where there is negligible ambient light penetration.

4.1.1.1 Monitoring Near-Turbine Interactions

Because of the potential for injury caused by contact between turbine blades and marine animals, resource agencies in the United States and Europe have focused on observations within the near-field ($\leq$ 10 m from turbine). Concerns regarding blade strike primarily originate from the well-documented mortality of fish passing through conventional hydropower turbines [*Coutant and Whitney*, 2000] and tidal barrages [*Dadswell and Rulifson*, 1994], as well as injuries to birds and bats caused by wind turbines [*Barrios and Rodríguez*, 2004]. Field observations and laboratory experiments conducted to date for tidal and river turbines [*Viehman and Zydlewski*, 2014; *Normandeau Associates*, 2009; *Amaral et al.*, 2011] suggest that such interactions are likely to be rare. However, these results need to be confirmed for a broader set of locations and technology variants. Ideally, field observations should be able to discriminate between contact and a near-miss between marine animals and the turbine rotor, identify the marine animal involved to the species level, continuously observe the entire near-field, and cause minimal behavioral changes. Simultaneously satisfying these constraints is not technically feasible, as evidenced by the variety of approaches employed to date, three of which are briefly summarized here to provide context for the development of the stereo-optical camera system.

Verdant Power operated an array of turbines near Roosevelt Island in the East River of New York from 2005 through 2008. The project used a combination of split-beam acoustic echosounders (BioSonics, DTX) deployed from shore and a vessel-deployed imaging sonar (acoustical camera) (Sound Metrics, DIDSON) to monitor fish passage. The array of split-beam transducers (24 in total) was able to monitor targets passing through the project area, but could not be used to detect animal strikes with the device or to identify fish to the species level [*Polagye et al.*, 2011].

Ocean Renewable Power Company tested a cross flow turbine from a barge near Eastport, Maine from 2010-2011. An acoustical camera (Sound Metrics, DIDSON) and single-beam echosounder were deployed from the generator barge to monitor fish behavior around the

operating rotor [*Viehman and Zydlewski*, 2014]. These observations were the first in-field documentation of fish passage through a tidal turbine, but the positioning of the sonars did not allow individual fish to be tracked through the turbine.

OpenHydro used unlighted video to monitor fish interactions with its turbine at the European Marine Energy Center in the Orkney Islands of the United Kingdom [*Barr*, 2010]. This approach was able to detect fish aggregations in the turbine wake during low current flows (e.g., < 1.5 m/s). This turbine was deployed within the photic zone and monitoring was restricted to daylight hours. Observations were conducted with a single camera deployed from a spar on one side of the turbine. Fish were not observed to pass through the turbine once it began rotating.

4.1.1.2 Technology Options for Near-Turbine Monitoring

Technologies potentially suitable for the study of near-turbine interactions include optical imaging, acoustical imaging, and animal-borne tags (i.e., tags actively transmitting an acoustic signal). Traditional fisheries trawls are unlikely to be feasible in close proximity to turbine rotors because of both the risk of net entanglement with the rotor and the difficulty of fishing effectively during periods of strong currents when interactions between turbines and fish are of greatest interest. In addition, as fish may experience injury or scale loss during capture in a trawl [*Ryer*, 2004], it may be infeasible to determine if body trauma resulted from interaction with the turbine rotor or from trawl capture. The potential trade-offs between available technologies are summarized in Table 4.1, following workshop discussions summarized in *Polagye et al.* [2014]. Of the available technologies, optical imaging may be best suited for discriminating between contacts and near-misses, as well as identifying targets to the species level, but subsampling in space and time are presently required due to data bandwidth. For example, a stereo imaging arrangement involving a pair of 2 megapixel black and white cameras with 16-bit resolution would produce more than 6 terabytes of uncompressed imagery per day when acquiring images at 10 fps. In contrast, a two-dimensional (2-D) imaging sonar acquiring information at a similar rate produces only about 0.09 terabytes/day.

Table 4.1: Capabilities of potential near-turbine monitoring technologies.

	Optical imaging	**Acoustical imaging**	**Animal-borne tags**
Discrimination between contact and near-miss	Possible with stereo imaging	Not generally possible due to acoustic reflection from hard surfaces	Not possible
Identification to the species level	Possible at close range with stereo imaging	Possible for species with distinct shapes or swimming patterns. Requires additional information for similarly sized species about presence/absence	Inherent
Continuous observations of entire near-field	Difficult due to positioning of cameras, data bandwidth, and functional range of cameras when artificial lighting is required	Difficult due to positioning of transducers and data bandwidth	Possible with an array of localizing receivers [*Furey et al.*, 2013; *McMichael et al.*, 2010]
Behavioral changes	Artificial illumination will affect behavior [*O'Driscoll et al.*, 2012; *Harvey et al.*, 2007; *Johnson et al.*, 2003; *Simmons*, 2006; *Marchesan et al.*, 2005; *Ryer et al.*, 2009; *Stoner et al.*, 2008]	Minimal effect	Short-term effects after handling for tag insertion [*Bridger and Booth*, 2003]

4.1.1.3 Site Description

There are no "typical" tidal energy sites. Each has unique attributes that can either impair or facilitate the use of optical imaging techniques. The intended use of the system described in this paper is at a tidal energy site in northern Admiralty Inlet, Puget Sound, Washington. Public Utility District No. 1 of Snohomish County has proposed to deploy two turbines manufactured by OpenHydro (www.openhydro.com) at this location [*PUD*, 2012]. The turbines are axial flow devices 6 m in diameter and would operate for up to five years as a demonstration project to evaluate environmental interactions and turbine reliability. If the demonstration project is successful, Admiralty Inlet has significant potential for large-scale tidal energy utilization [*Polagye et al.*, 2009]. The water depth in the project area is approximately 55 m and the turbine hub height is 10 m above the seabed. During strong tidal exchanges, currents exceed 3 m/s [*Polagye and Thomson*, 2013].

As discussed in Section 4.1.3.4.1, there is likely to be minimal ambient light at the depth of the turbine rotors at this location such that artificial illumination will be required. Measurements indicate turbidity to be less than 1 NTU *Polagye and Thomson* [2013] but benthic habitat surveys utilizing remotely operated vehicles [*Greene*, 2011] have encountered significant biological flocculent close to the seabed that limited the visible range of their camera systems. This flocculent can interfere with optical imaging by both obscuring the target and scattering artificial illumination back towards the cameras.

4.1.2 Imaging System Description

This section provides a description of the imaging system that is developed and evaluated, starting with a background of prior developments.

4.1.2.1 Prior Developments

Mono- and stereo-optical imaging systems with artificial illumination have been deployed by several research groups to study the marine environment. *Howland et al.* [2006] developed

a towed single camera system to capture high-resolution still imagery for scallop population density. Similarly, *Rosenkranz et al.* [2008] developed an imaging system to provide high-resolution images of benthic habitats. *Williams et al.* [2010] employed stereo imaging to study rockfish abundance in untrawlable areas. These systems share a number of requirements with imaging of tidal turbines, such as operating depth and towing or current velocity, but were not developed for long term deployments or for use in areas with high levels of biological flocculent as would be the case for tidal turbine monitoring. Further, in reviewing the literature on stereographic imaging, there have been no standardized test cases for objective optimization of system performance. Most lateral stereo arrangements have been studied using parallel camera axes [*Barnard and Fischler*, 1982; *Alvertos et al.*, 1989] or, more recently, to mimic human vision for 3-D cinema [*Westheimer*, 2011; *Aylsworth et al.*, 2013]. Optimization methods for stereo vision have generally focused on the correspondence problem (i.e., selection of points in stereo images that correspond to the same spatial location) and image matching (i.e., transforming data from stereo images into a single coordinate system) for computer vision [*Jones*, 1997].

4.1.2.2 Design Parameters

The operational objectives for the imaging system that is the subject of this paper are to classify targets (e.g., taxonomic classification to the species level, if possible) within the near-field environment (e.g., within 1-2 turbine diameters distance from the turbine and subsea base) of an operating hydrokinetic turbine, without significantly affecting animal behavior. During periods of strong currents, the relative velocity between the camera and these targets may be on the order of several m/s. Due to the difficulty and cost of maintaining the imaging system, which will require remotely operated vehicle (ROV) operations for recovery to the surface [*Joslin et al.*, 2013], the system will need to operate for multiple months at a time. For deployments of this duration, biofouling of the optical ports could rapidly degrade system effectiveness and will require mitigation [*Lehaitre and Compere*, 2005]. Shore power up to 1 kW and fiber optic data connectivity with 1 Gb/s bandwidth will be available.

The imaging system developed in response to these objectives and constraints is a stereo-optical system, incorporating two machine vision optical cameras. As described in Section 4.1.3.1, calibrated stereo cameras can provide information about the absolute position, size, and speed of targets. Target size is particularly relevant for classification.

The primary trade-offs in camera selection are resolution, bandwidth, and cost. High-resolution increases the potential for target classification, but at high frame rates (e.g., 10 Hz) data bandwidths can easily exceed the capacity of the communications system. To capture crisp images with relative motion on the order of 3 m/s, an exposure time between 2 and 50 μs is recommended [*Gallager et al.*, 2005]. This can be achieved by strobe illumination. Increased camera-light separation improves the effective range by reducing backscattered light from turbidity and flocculent [*Jaffe*, 1988]. However, the camera-light separation is constrained by the maximum practical package size for maintenance operations at tidal sites that require deployment by ROV (in this case, < 0.5 m^2 of frontal area).

4.1.2.3 Principle System Components

The principle components of the imaging system were, therefore, a pair of cameras, four strobe illuminators for redundancy and even illumination of targets, and the power/communications architecture to integrate them and communicate with shore via the fiber optic link. In addition to the stereo-optical camera an acoustical camera was included in the package for future use (further discussion in Section 4.1.5). The selected cameras were Allied Vision Technologies Manta G-201 B/Cs (2 Mpixel, www.alliedvisiontec.com). These were compact, industrial-grade machine vision cameras operating on Gigabit Ethernet (GigE) vision protocols. Each camera was equipped with a 5 mm focal length lens (Navitar NMV-5M23). A wider field of view (discussion in Section 4.1.3.3.1) could have been achieved with a shorter focal length lens, but at the cost of decreased image resolution. For strobe illumination, four Excelitas Technologies MVS-5002 units were selected on the basis of their performance in underwater camera systems with similar specifications [*Howland et al.*, 2006]. The acoustical camera was a BlueView P900-2250 (www.blueview.com).

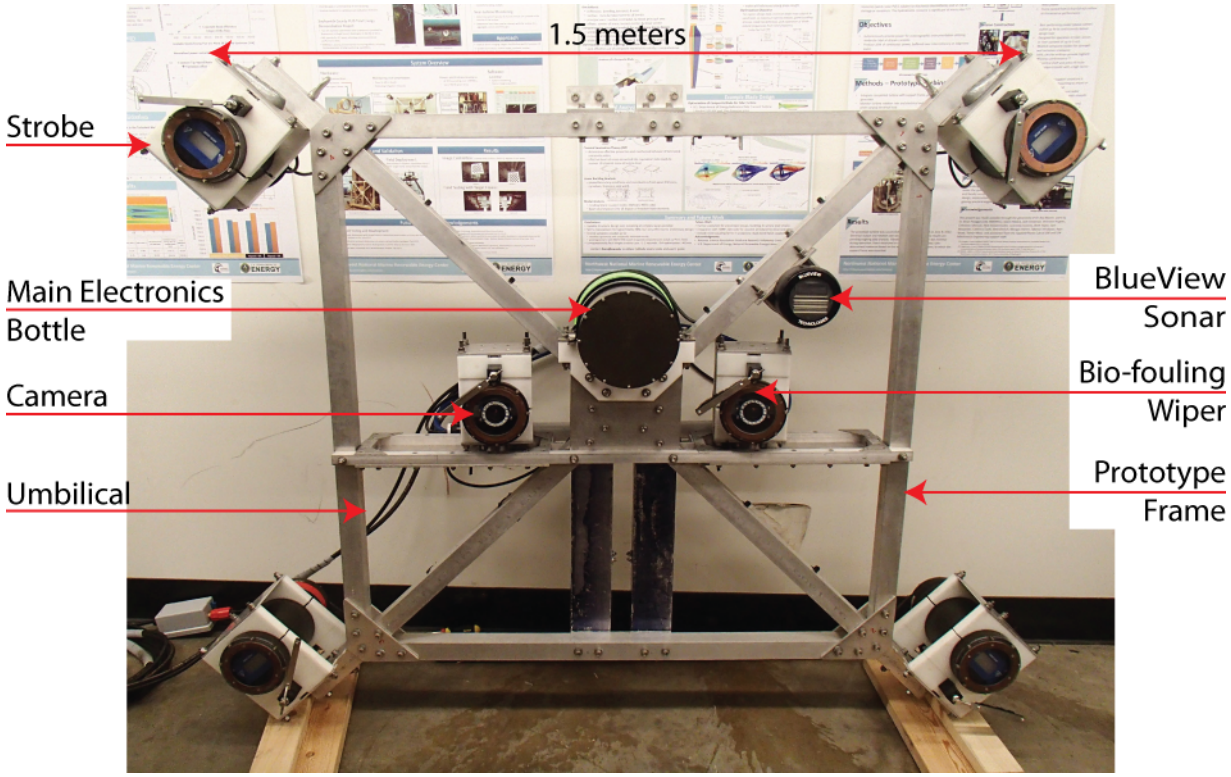

Figure 4.1: Prototype imaging system showing principal components and scale.

With the exception of the acoustical camera, the system components were not designed for underwater use and were enclosed within pressure housings. The pressure housings for the optical cameras and strobes were anodized aluminum with acrylic optical view ports (planar). For testing, these modular components were mounted to an aluminum frame, as shown in Figure 4.1, which resulted in a camera-strobe separation distance of ∼1 m. The frame allowed for the optical camera separation to be adjusted between 0.5 and 1.1 m with camera toe-in angles up to 10°. A method for determining optimized separation and toe-in angle is presented in Section 4.1.3.2.

To address biofouling concern, a mechanical wiper (Zebra-Tech Hydro-wiper, www.zebra-tech.co.nz) was integrated into each housing and copper rings are placed around the perimeter of the optical ports. A commercially available antifouling coating that would complement the mechanical wiper could also be employed [*Joslin and Polagye*, 2015].

Off-the-shelf component specifications and costs are detailed in Table 4.2.

Table 4.2: Component descriptions and costs for the stereo-optical camera system.

Component	**Manufacturer**	**Description**	**Quantity required**	**Unit cost**
Optical cameras	Allied Vision Technologies, Manta G-201B/C	2Mpixel, GigE Vision Camera with Sony ICX274 Sensor, 1624 x 1234 pixels, 4.4 μm pixel cell size, 1/1.8 in. sensor size, 14 fps	2	$1600
Lenses	Navitar NMV-5M23	2/3 in. Mpixel format with manual focus from 0.05 m to infinity and 2.8 to 16 F-stop	2	$500
Strobes	Excelitas Technologies MVS-5002	20 μs flash duration, 30 Hz maximum flash rate	4	$1300
Acoustic camera	BlueView P900-2250	Dual frequency sonar with 45 deg x 20 deg field of view, 60 m (900 kHz) and 8 m (2.25 MHz) maximum range	1	$30,000
Mechanical wipers	Zebra-Tech LTD	Brush style hydro fouling optical port wiper	6	$1300

Table 4.3: Component power requirements at maximum data acquisition rates.

Component	**Mode**	**Power requirement (W)**
Optical cameras (2)	Acquiring at 10 fps	10
Strobes (4)	Strobing at 10 hz	72
Mechanical wipers (6)	3 wiper motors locked (high failure rate)	18
Media conversion and auxiliary loads	Operating	30
DC conversion losses	80% efficiency	37
Total system draw		167

4.1.2.4 System Operations

To minimize system cost and complexity, the primary communications bus operated on Ethernet protocol, with media conversion from copper to fiber to extend its range. A secondary communications bus operated on serial protocol (converted to Ethernet) and was used to monitor the health of various components (current draw, temperature, and humidity) and control power distribution. Low-cost media conversion limited the total bandwidth to 1 Gb/s (125 MB/s).

Power requirements for system components are described in Table 4.3. Custom power electronics stepped down the main supply power (375 VDC) to a 12 V component supply. These were built around Vicor (www.vicorpower.com) DC-DC converters. Medium voltage DC power supply was required to minimize resistive losses over the long cable run between the turbine and shore station. Temperature, humidity, and current monitoring in each pressure housing also utilized custom electronics.

System operation, monitoring, camera control, and optical image acquisition were per-

formed with the National Instruments LabView serial communications (VISA) and image acquisition (IMAQ) modules (www.ni.com/labview). The image acquisition module was configured to allow a user to directly control a limited subset of camera settings accessible through GigE Vision protocol, such as frame rate, exposure time, digital gain, and strobe triggering. Simultaneous image acquisition from both cameras was achieved by a hardware trigger (i.e., electrical trigger connection between the master camera and slave camera) and the virtual shutter effect due to the short strobe duration (20 μs) in the absence of ambient light. Qualitative acoustical camera imagery was acquired using a proprietary software package (ProViewer, BlueView).

4.1.3 Testing and Optimization Methodology

The methods used to evaluate the imaging system are presentes in this section starting with a review of the fundamentals of stereo imaging.

4.1.3.1 Stereo Imaging Fundamentals

Stereographic imagery uses cameras in multiple positions to map three-dimensional space from two-dimensional images. Many arrangements for stereographic systems have been proposed [*Alvertos et al.*, 1989] each of which has various benefits and drawbacks to system performance. The system described here is a general two camera lateral arrangement (i.e., side-by-side cameras on a common lateral axis), as described in *Alvertos et al.* [1989]. The three parameters that describe this arrangement are (1) the rotation angle of the cameras, ω, (2) the baseline separation of the two cameras, b, and (3) the toe-in angle of the cameras, ϕ. Determination of appropriate values for each of these variables depends on the operating field of view of each camera, θ, and the expected target range. To fully describe the stereo system, the intrinsic parameters for each camera (e.g., focal length, principal point, skew, distortion coefficients) and the extrinsic parameter (e.g., relative camera spacing, orientation) for the system must be measured experimentally. For simplicity in this section, the two cameras are assumed to be identical and modeled as ideal pinhole cameras. The pinhole camera model

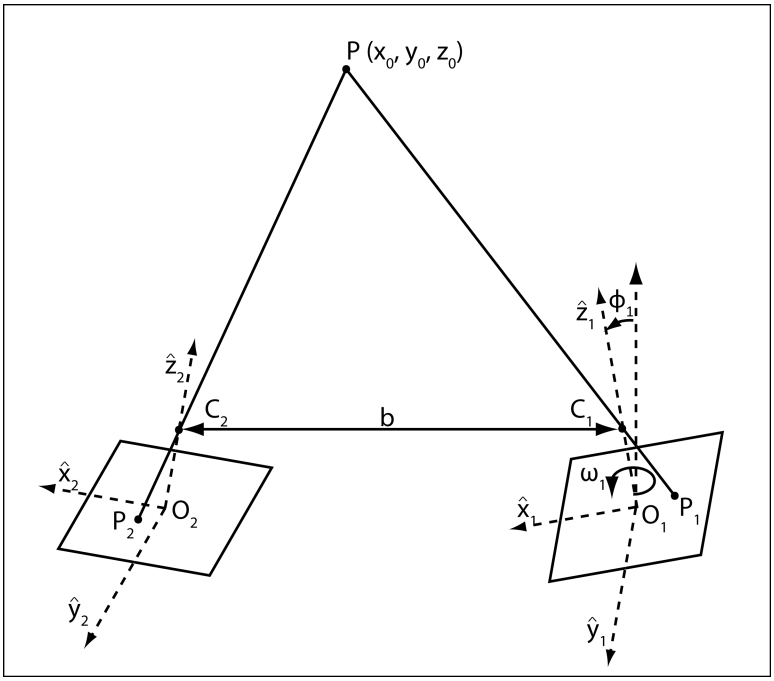

Figure 4.2: General three-dimensional stereo camera arrangement.

represents the camera as a single point in three-dimensional space through which light is projected onto an associated image plane where the optical sensors are located, neglecting lens distortion effects [*Wohler*, 2013]. Figure 4.2 shows a generalized lateral arrangement with the right and left cameras located at C_1 and C_2 respectively and the associated image planes centered at O_1 and O_2. For the chosen machine vision cameras, the image plane is rectangular with the $x-$ and $y-$ axes containing 1624 and 1234 pixels respectively.

Triangulation uses pixel coordinates in each image plane corresponding to the same point in three-dimensional space to determine that points coordinates. Target size may be calculated from a pair of stereo images by computing the Euclidean norm between two triangulated points in the same image pair. Similarly, target velocity may be calculated from the distance a single point moves over sequential frames. As shown in Figure 4.2, two coordinate systems are defined at the center of the right and left image planes as $(\hat{x}_1, \hat{y}_1, \hat{z}_1)$ and $(\hat{x}_2, \hat{y}_2, \hat{z}_2)$

respectively. These coordinate systems are related to each other by

$$\begin{pmatrix} \hat{x}_1 \\ \hat{y}_1 \\ \hat{z}_1 \end{pmatrix} = \begin{pmatrix} \hat{x}_2 \\ \hat{y}_2 \\ \hat{z}_2 \end{pmatrix} R + T, \tag{4.1}$$

where R is a 3 x 3 orthonormal rotation matrix and T is a translation vector, which define the extrinsic parameters of the stereo system. For a fixed camera arrangement, these values are constant and are readily obtained by the calibration procedure discussed in Section 4.1.3.3.1. A target point (P) that is within the field of view of both cameras will have the coordinate (x_1, y_1, z_1) and (x_2, y_2, z_2) in the right and left coordinate systems, respectively. Projections of this point on each two-dimensional image plane through the respective camera lens are identified as P_1, with coordinates $(x_1^i, y_1^i, 0)$ and P_2, with coordinates $(x_2^i, y_2^i, 0)$. These image coordinates are related to the three-dimensional target point coordinates in each system by

$$\frac{x_1}{x_1^i} = \frac{y_1}{y_1^i} = \frac{\lambda - z_1}{z_1^i} \tag{4.2}$$

and

$$\frac{x_2}{x_2^i} = \frac{y_2}{y_2^i} = \frac{\lambda - z_2}{z_2^i}, \tag{4.3}$$

where $\lambda = C_1O_1 = C_2O_2$ (i.e., the camera focal lengths are equal). With a known set of extrinsic parameters, Eqations 4.1, 4.2, and 4.3 may be combined to determine the spatial coordinates of a target point, P, from the pixel coordinates of the target projection in each camera image. Choosing image coordinates that represent the same target point may be challenging due to the different perspectives of each camera and is referred to as the correspondence problem in machine vision [*Alvertos et al.*, 1989]. Although the automation of target identification and tracking may necessitate further investigation of this problem in the intended application, more information about image quality and target frequency and size is first needed to constrain the problem.

4.1.3.2 Optimizing Camera Arrangement

Optimization of this camera arrangement for the purpose of measuring target location, size, and speed involves the maximization of the percentage of overlapping fields of view of the two cameras and the minimization of triangulation error due to depth perspective. The overlapping field of view of the two cameras is defined as the volume of space where a target appears in both camera images. Since the area captured in either image increases with distance from the camera, but target triangulation at any position in the near-field of a turbine is equally important, volumetric overlap, as a percentage of an individual cameras volumetric field of view, is chosen as the optimization criteria. This percentage depends on all three of the arrangement variables (ω, b, and ϕ). The range over which the volumetric fields of view are calculated depends on the functional range (or distance at which a target is expected to be detectable, discriminated, or classified) of the system which is evaluated through field testing in Section 4.1.4.2.

The camera rotation angle that maximizes the overlapping field of view occurs when the image planes are aligned on the horizontal x-axis or side-by-side (where the x-axis is defined as the dimension of the image plane with the greatest number of pixels). In this arrangement, the vertical y-axis field of view is equal and the system orientation can be described entirely in the $\hat{x} - \hat{z}$ plane, as in Figure 4.3.

Given a symmetric lateral stereo arrangement, the overlapping field of view may be calculated on the basis of a coordinate system centered between the two cameras at O. The percentage of the overlapping volumetric field of view of the two images on any plane parallel to O may be written as a function of distance from O to a target, d; the horizontal field of view angle, θ; the toe-in angle, ϕ; and the baseline separation, b. First, let x_a, x_b, x_c, and x_d be the horizontal limits of the right and left camera images, respectively, at distance, d, as shown in Figure 4.3b, which may be calculated as

$$x_a = \frac{b}{2} + d\tan(\theta - \phi), \tag{4.4}$$

$$x_b = \frac{b}{2} + d\tan(\theta + \phi), \tag{4.5}$$

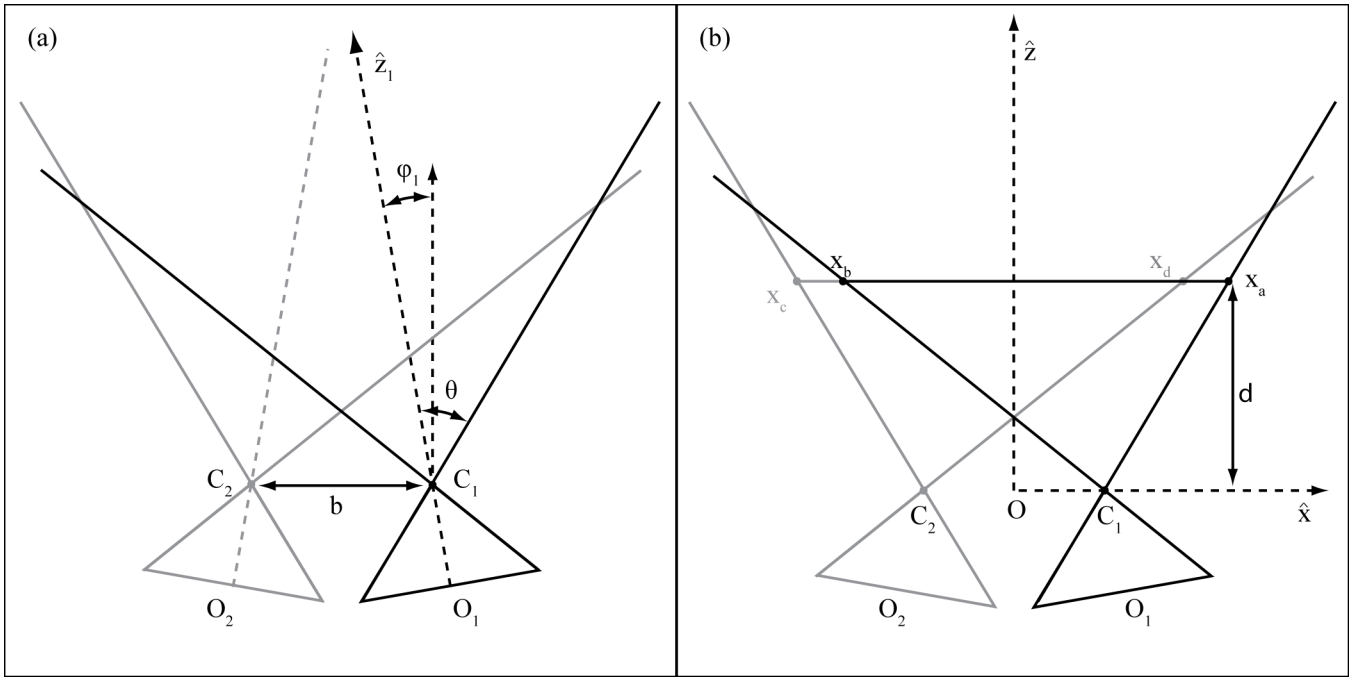

Figure 4.3: Stereo camera arrangement diagrams with (a) camera arrangement variables in the $x - z$ plane and (b) variables describing the over-lapping volumetric field of view at a given distance (d) from the camera.

$$x_c = -x_a, \tag{4.6}$$

$$x_d = -x_b. \tag{4.7}$$

Consequently, recalling that there is complete overlap in the y-direction, the percentage of the volumetric field of view that overlaps between the left and right cameras, FOV, is

$$FOV(d) = \begin{array}{ccc} 0 & & d \leq (b/2)\tan(\theta+\phi) \\ 2x_b/(x_a - x_b) & for & (b/2)\tan(\theta+\phi) < d \leq b/[\tan(\theta+\phi) - \tan(\theta-\phi)]. \\ -2x_a/(x_a - x_b) & & b/[\tan(\theta+\phi) - \tan(\theta-\phi)] < d < d_max \end{array} \tag{4.8}$$

Once the field of view and functional range have been established for a given application, Equation 4.8 can be integrated over the functional range for various baseline separations and toe-in angles to evaluate the percentage overlap for a given configuration.

Intuitively, the greatest overlap occurs when the baseline separation is minimized. Target triangulation however, uses the disparity of the two images to measure the distance on the z-axis. This depth perspective increases with increasing baseline separation and, consequently, spatial triangulation errors may increase as the stereographic field of view is maximized. To understand the sensitivity of triangulation to the baseline separation, experiments were conducted with the cameras at the extreme limits of baseline separation (0.5 and 1.0 m) and with toe-in angles that maximize the percentage of overlap in a range of 1 to 5 m.

4.1.3.3 System Tank Testing

Initial system testing was performed in a controlled laboratory environment using a large saltwater tank. This testing allowed for the estimation of camera parameters and evaluation of triangulation accuracy and target tracking capabilities.

4.1.3.3.1 Intrinsic and Extrinsic Camera Parameters The field of view of the individual cameras was measured empirically by acquiring images of a graduated rule at a known distance from the camera that spanned the horizontal axis of the image. To account

for lens barrel distortion and refraction at the air/water interface across the optical port on the pressure housing, images were acquired underwater.

The calibration procedure for the stereo camera pair, which was used to estimate the intrinsic and extrinsic parameters, closely followed the methods described in *Williams et al.* [2010]. Images of a one-meter square calibration target with a 7 x 8 checkerboard pattern of 10 cm squares were acquired in an indoor, saltwater pool with a camera-target separation distance ranging from 3 to 6 m. With the camera system suspended approximately one meter below the surface of the water, the target was moved through the water while images were collected, yielding a set of images with the target at various three-dimensional orientations relative to the static camera position. For each combination of baseline camera separation and toe-in angle, fifty image pairs were collected.

The images were analyzed using an open-source camera calibration toolbox for Matlab [*Bouguet*, 2010]. This software uses the Harris corner finding algorithm, which locates the square corners on the calibration target in each image based on color gradients[*Harris and Stephens*, 1988]. From these coordinates, estimates of the intrinsic parameters of the individual cameras were produced, based on the known target size. These parameters accounted for all barrel distortion of the images and were used to rectify images acquired by either camera. With the estimated intrinsic parameters for the individual cameras, a stereo calibration was used to estimate the extrinsic parameters of the camera system by analyzing the target position in the image pairs and iteratively computing the epipolar geometry [*Xu and Zhang*, 1996]. Together these intrinsic and extrinsic parameters represent the system model necessary for target triangulation.

4.1.3.3.2 Triangulation Accuracy Along with the estimates for the intrinsic and extrinsic parameters of the camera system, the calibration procedure provided an estimate of pixel errors. These errors were the differences between the pixel coordinates of the corners found using the Harris method during calibration and the expected corner location based on a reprojection of the target on each image. These errors were used to evaluate the calibra-

tion procedure and the accuracy of the corresponding system model for the camera pair. For example, a T-test statistical comparison of the magnitude and standard deviation of these errors enabled assessment of the accuracy of different baseline separations and toe-in angles.

4.1.3.3.3 Target Tracking Capability The system's ability to measure and track a target in three-dimensional space was demonstrated by moving a model killer whale (20 cm length) through the cameras' field of view. Images were collected at 2 frames per second for 30 s. For each image pair, the tip of the head and tail were manually identified. From this, an estimate was produced of the target length and spatial position. As discussed in Section 4.1.5, in operation around a tidal turbine, target detection and tracking would likely make use of automated processing routines.

4.1.3.4 System Field Testing

This section describes the field testing of the system performed in Admiralty Inlet and Sunset Bay, Puget Sound, WA.

4.1.3.4.1 Admiralty Inlet, Puget Sound, WA One of the key uncertainties regarding the integration of the optical imaging system with a tidal turbine was the functional range for detection, discrimination, and classification of marine animals by the optical cameras. The "functional range" refers to the range over which these capabilities are possible, with the functional range for detection being greater than for classification. This distance established where the imaging system should be deployed to observe interactions with a turbine rotor. A secondary question was the comparative effectiveness of the optical and acoustical camera systems to meet the objectives of near-turbine monitoring. The main variables that could affect imaging system effectiveness to classify a target were (1) the target range and orientation, (2) relative velocity between the target and camera, (3) attenuation of artificial lighting by turbidity and flocculent, (4) the optical camera digital gain setting, and (5) behavioral effects of the strobe illumination. In this study, the first four of these were qualitatively

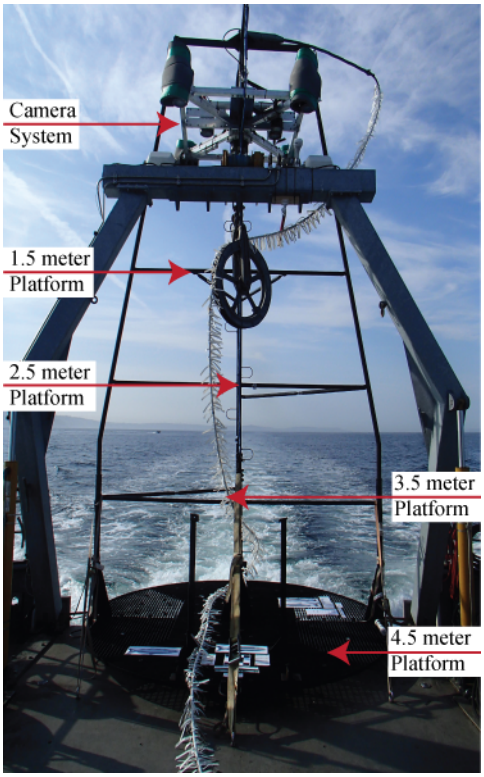

Figure 4.4: Imaging frame for camera testing.

evaluated by capturing images in varying environmental conditions and camera settings.

Given the difficulty of accurately simulating flocculent and high relative velocities between targets and the camera in a laboratory setting, a field evaluation was undertaken with the imaging frame shown in Figure 4.4. The frame consisted of a mounting point for the imaging system located 4.5 m above the base of the frame. The frame had an in-air weight of approximately 1360 kg (3000 lbs). Relative water velocities of up to 2 m/s were achieved by towing the imaging frame from a high-tensile strength umbilical cable (Rochester A302351) with power conductors and optical fibers. Various targets were attached to platforms at camera-target separation distances of 1.5 m, 2.5 m, 3.5 m, and 4.5 m. These targets included static objects, such as a single 10 cm square from the calibration image described in Section 4.1.3.3.1, standard eye charts, and line drawings of fish. The latter include large adult salmon (42 cm fork length), as well as small juvenile salmon and Pacific herring (5-11 cm fork length). Fish drawings were printed on a white or green background to provide either low or high

contrast between the fish and background, respectively. As many fish expected at this site have a silver coloration, the white background provided a lower contrast around the edge of the printed image. In addition, tape streamers were attached to the frame and used to evaluate the ability of the camera system to capture rapid, complex motions without image blur. Other targets, including three-dimensional metallic objects and flash-frozen fish were considered and tested during methodology development. Preliminary testing demonstrated that these targets were more difficult to handle and did not provide more useful information than printed targets and streamers about system performance.

In addition to image acquisition by the optical and acoustical cameras, several types of ancillary data were collected during field experiments. Cosine irradiance light meters (HOBO Pendant Temp-Light, www.onsetcomp.com) were attached to the camera frame and imaging frame platforms. These were intended to characterize the intensity of strobe illumination, but their response time was insufficient to achieve this, even at 10 Hz strobe rate and 1 Hz light meter sampling rate. However, information from the light meters was used to characterize the light attenuation coefficient tests and quantify ambient light levels. Co-temporal profiles of depth and illumination obtained during deployment and recovery of the imaging frame were used to evaluate the attenuation coefficient by fitting them to a profile of the form

$$I(z) = I_0 e^{-cz}, \tag{4.9}$$

where I is illumination (Lux), z is depth relative to the surface (m), and c is the empirical attenuation coefficient [*Beer*, 1852]. Pressure loggers (HOBO U20 Water Level, www.onsetcomp.com) were attached to the camera frame and the base of the imaging frame to monitor depth at a sampling rate of 1 Hz. During tows, the umbilical wire angle could be significant, up to 40° at maximum tow velocities. Vibration was monitored by accelerometers on each platform and on the camera frame (HOBO Pendant G, www.onsetcomp.com) logging at 1 Hz. Relative water velocity between the tow frame and flocculent was monitored by a through-hull mounted Doppler profiler (RDI Workhorse 300 kHz, www.rdinstruments.com). Single-ping Doppler profiler data were recorded and ensemble averaged over the duration of

image acquisition for a set of camera test parameters. Water depth was monitored by the tow vessels echosounder and location was monitored by differential GPS, both logging at 1 Hz in Nobeltec software (www.nobeltec.com).

Assessments of imaging system performance included qualitative observations of flocculent density/motion and clarity of both the eye charts and fish line drawings. A quantitative assessment of performance was obtained by calculating the length of one horizontal side of the 10 cm central black square on the calibration target from image pairs under different test conditions using the triangulation technique described in Section 4.1.3.1. Absolute measurement error for each image pair was defined as

$$e = L_{measured} - L_{actual}, \tag{4.10}$$

where $L_{measured}$ and L_{actual} are the stereographically measured and actual length of the calibration square, respectively. For simplicity of presentation, e was quantified in units of mm.

Tow tests were undertaken August 13-16, 2012 in northern Admiralty Inlet, Puget Sound, Washington. All tows were conducted by the University of Washington Applied Physics Laboratory's research vessel, the R/V Jack Robertson. Testing occurred during periods of falling tidal currents on greater ebb and flood to characterize performance during periods when biological flocculent would likely be suspended in the water column by intense tidal currents. There is also likely to be substantial seasonal variation in water clarity, with conditions in August likely to be on the lower end of seasonal clarity. Testing during this seasonal period was intended to demonstrate the system capabilities in a potentially "worst case" of water clarity. During each tow, static targets were positioned on the imaging frame at a camera-target separation distance of either 2.5 m, 3.5 m, or 4.5 m. Preliminary testing undertaken at an earlier date indicated shading of lower platforms by upper platforms could significantly degrade the quality of more distant images when multiple platforms were simultaneously employed. These earlier tests also indicated that targets were easily classified at 1.5 m range. Consequently, each test involved targets at a single camera-target separation

distance and no tests were undertaken at separation distances 2.5 m. During each test, the imaging frame was lowered through the water column until the bottom of the frame (4.5 m distance from the cameras) was at a depth of 50 m. Images were acquired in blocks of fifty pairs at sampling rates of 5-10 frames per second under the following combinations of conditions:

- Camera-target separation: 2.5 m, 3.5 m, or 4.5 m
- Relative water velocity: near-zero (free-drift) or 2 m/s (tow)
- Optical camera digital gain: $0x$, $10x$, or $20x$

Each set of tests also included optical image capture with the strobes off and a camera gain of $20x$, to confirm the expectation that observations at this depth and location required artificial illumination. Absolute measurement error was evaluated for the first thirty image pairs under each of the test conditions using Equation 5.19 to measure the length of one horizontal side of the 10 cm calibration square. This quantitative evaluation of the system performance was used to assess the variance of measurements of a target of known size conducted in each of the conditions described above. In other words, these tests represent the best case system performance in the given environmental conditions.

4.1.3.4.2 Sunset, Puget Sound, WA From March 3 to July 2, 2013 the camera system was deployed on the target frame near a dock in Sunset Bay, Puget Sound, WA to evaluate the systems endurance in a salt water environment. The system and target frame were placed on the bottom in approximately 20 m of water and cabled to shore for power and data connectivity. Throughout the deployment, 10 images (1 s of imagery at 10 fps) were captured at 15 minutes intervals to monitor for marine life around the frame and assess the biofouling on the cameras optical ports and support frame [*Joslin and Polagye*, 2015]. Images captured of fish in variable water quality conditions provided an additional point of comparison for qualitatively evaluating the systems ability to detect, discriminate, or classify fish at various camera-target separation distances. For comparison to open-water field trials,

Table 4.4: Calibration reprojection error values for each camera.

	Camera 1	**Camera 2**
Horizontal and vertical pixel error (x, y)	(0.065, 0.059)	(0.14, 0.13)
Localization uncertainty at 3.5 m (x, y) [mm]	(0.081, 0.091)	(0.17, 0.20)

static targets were mounted to the bottom of the frame at a distance of 4.5 m, but no static targets were included at intermediate distances.

4.1.4 Results

The results from system testing and evaluation are presented here in an order matching the methods.

4.1.4.1 System Tank Testing

Tank testing results demonstrate the system performance in a laboratory environment and provide the camera parameters needed for field testing.

4.1.4.1.1 Intrinsic and Extrinsic Camera Parameters The measured field of view of the individual cameras was approximately 54° in the horizontal direction (x-axis) and 42° in the vertical direction (y-axis). For reference, at a camera-target separation distance of 3.5 m, each pixel corresponded to a physical dimension of 2.10 mm by 2.17 mm and the field of view (including barrel distortion) is 3.4 m by 2.7 m.

As described in Section 4.1.3.3, uncertainty in the intrinsic parameters estimated through the calibration process was quantified by pixel error for each camera. Table 4.4 shows the standard deviation of the error values associated with the calibration procedure conducted prior to the field deployments which are representative of a typical calibration. This error

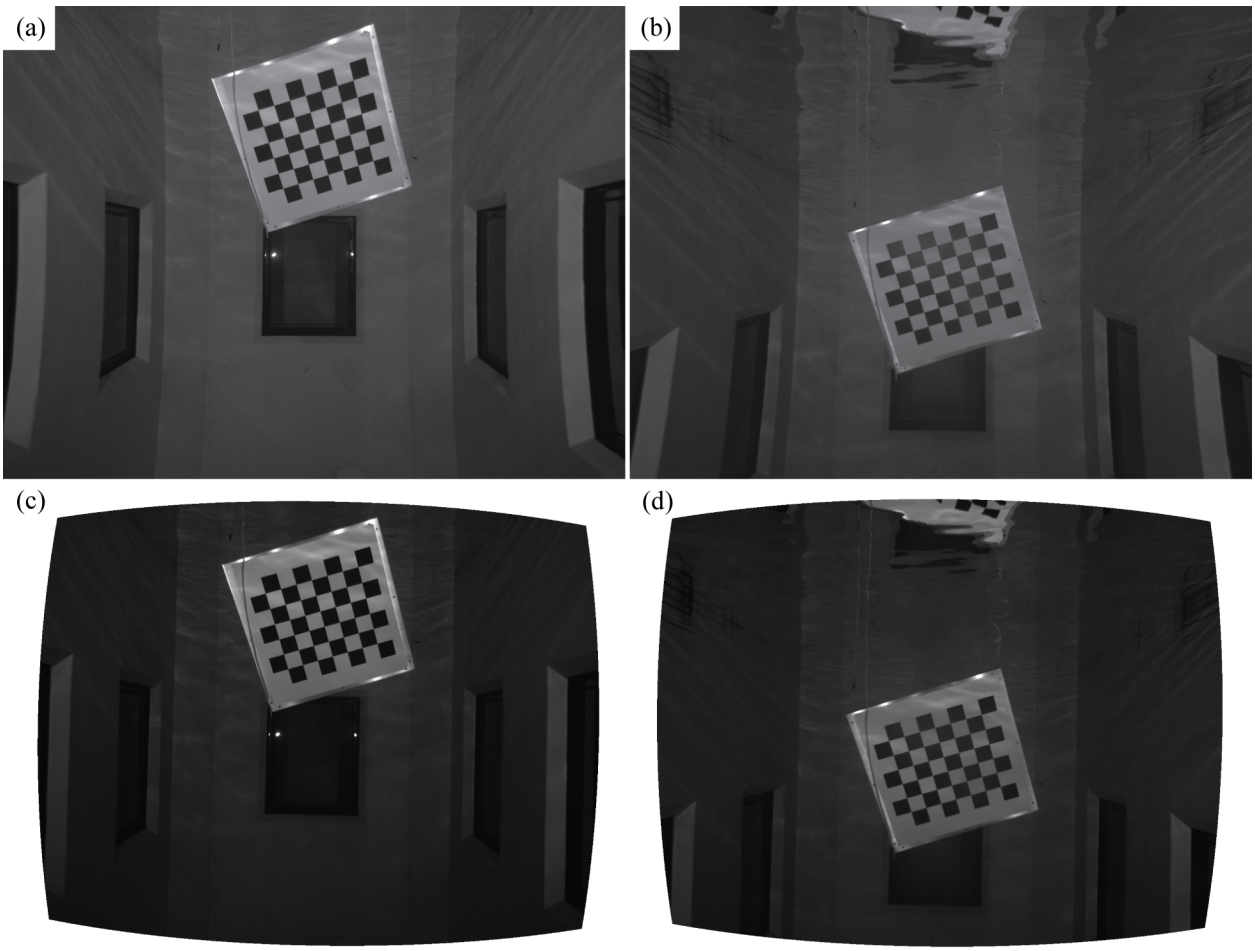

Figure 4.5: Camera 1 (left) and camera 2 (right) calibration images before (a and b) and after (c and d) rectification.

varied throughout the stereographic field of view and caused a position bias for fixed points in space. At a distance of 3.5 m from the center of the camera pair, these values resulted in a spatial positioning error of approximately 0.2 mm.

Raw and rectified images from each camera are shown in Figure 4.5 with the barrel distortion effects clearly visible in the curvature of the windows along the edges of the original images.

4.1.4.1.2 Optimized Camera Arrangement The objective of camera arrangement optimization was to maximize the stereographic field of view without significantly reducing

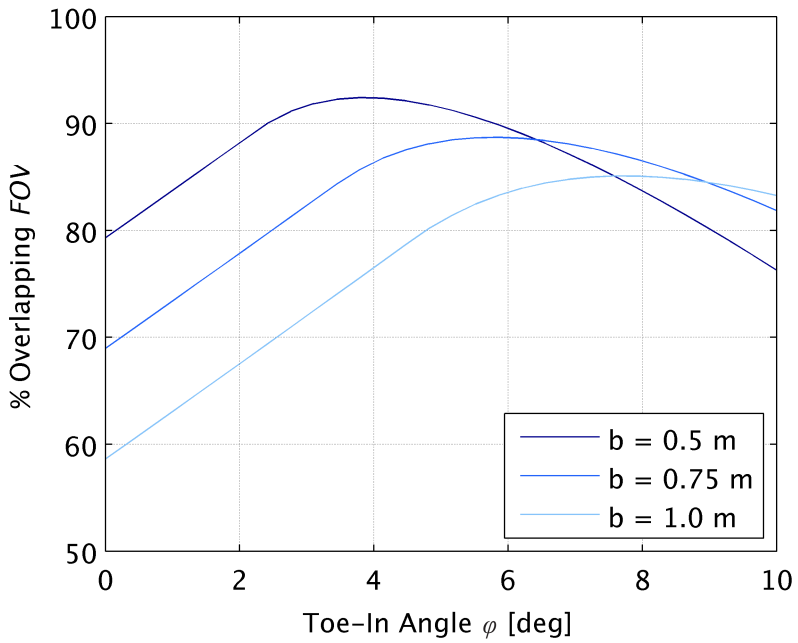

Figure 4.6: Variation in volumetric field of view overlap as a function of toe-in angle and camera spacing (b).

triangulation accuracy. Figure 4.6 shows the percentage of the overlapping field of view with baseline separations (b) of 0.5, 0.75, and 1.0 m over a range of toe-in angles and a field of view defined by a camera-target separation distance (measured from the center of the camera pair) of 1 to 5 m.

With a baseline separation (b) of 0.5 and 1 m the maximum overlapping field of view occurred when the cameras were towed-in to an angle of 3.8° and 7.6°, respectively. Figure 4.7 shows a boxplot distribution of the calibration pixel errors (N = 8400) for these two arrangements. A statistical T-test showed no difference between the two arrangements with a P-value of 1.0, suggesting that triangulation accuracy was not sensitive to the baseline separation over the range of values tested. The optimized system arrangement, therefore, was based purely on maximization of the overlapping field of view, given by $b = 0.5$, $\phi = 3.8°$, and $w = 0°$.

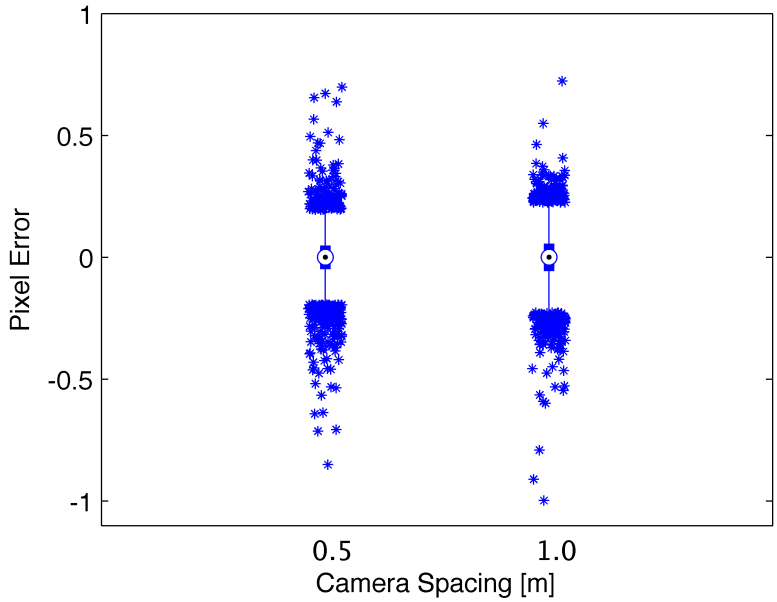

Figure 4.7: Calibration pixel errors ($N = 8400$) at baseline separations (b) of 0.5 and 1 m. Circles denote median values; solid lines denote the 25th and 75th percentile; thin bars denote the extent of measurements beyond the interquartile range; and asterisks denote outliers that are beyond 1.5 times the interquartile range.

4.1.4.1.3 Target Tracking Capability The system's ability to measure and track a complex target in three-dimensional space was demonstrated in the 30 s of imagery shown in Video 1 (available online URL: http://dx.doi.org/10.1117/1.JRS.8.083633.1). For each image pair with the killer whale model visible, the projected points at the head and tail were plotted along with the corresponding coordinates relative to the left camera in the 3-D plot below the image pairs. The target length measurements conducted in this video had a mean of 212 mm ($N = 47$), which was equal to the actual length of the model killer whale, and a standard deviation of 15 mm. Tracking included cases in which the target was nearly head-on to the cameras.

4.1.4.2 System Field Testing

Results from the system field testing are presented for the two field sites in Puget Sound, WA.

4.1.4.2.1 Site-Specific Attenuation Coefficient, Admiralty Inlet, Puget Sound, WA Four co-temporal depth/light profiles were evaluated to characterize ambient light at testing depth using the procedure described in Section 4.1.3.4. As previously discussed, these were collected on August 13-16, 2012 at the location proposed for tidal turbine deployment. Values for the attenuation coefficient (c) obtained during four profiling casts with the target frame ranged from 0.15 to 0.24 m^{-1} based on fits to data between the surface and depth at which light meter sensitivity was exceeded. These values are within the range of values expected for coastal waters [*Jaffe*, 1988] and confirmed qualitative expectations for turbidity. Attenuation in embayments can be an order of magnitude higher [*Jaffe*, 2007], which would significantly degrade the performance of the optical cameras. Observations of optical camera imagery during the tests indicated that artificial lighting was required below a depth of approximately 30 m to detect targets, corresponding to an ambient illumination of approximately 5 Lux.

4.1.4.2.2 Functional Range and Performance, Admiralty Inlet, Puget Sound, WA Table 4.5 details the conditions tested, in terms of the experimental variables and site conditions. Specifically, z is the depth of the camera frame, H is the total water depth, and u is the actual relative velocity between the imaging frame and the water. Two gain settings were not evaluated for quiescent conditions (i.e., 0 m/s nominal) with a 3.5 m camera-target separation because, even with the surface vessel drifting, the relative velocity between the test frame and currents exceeded 1 m/s. Quiescent conditions for other tests corresponded to a relative velocity of less than 0.5 m/s.

Example images used for qualitative evaluation of the optical system are shown in Figure 4.8. As expected, image clarity degraded with distance (Figure 4.9) due to a combination

Table 4.5: Camera evaluation cases from tow testing.

Camera-target separation	**Nominal relative velocity**	**Digital Gain**		
		$G = 0x$ (no gain)	$G = 10x$	$G = 20x$
2.5 m	0 m/s	$z = 46$ m	$z = 46$ m	$z = 46$ m
		$H = 61$ m	$H = 61$ m	$H = 60$m
		$u = 0.2$ m/s	$u = 2.0$ m/s	$z = 1.8$ m/s
	2 m/s	$z = 30$ m	$z = 33$ m	$z = 31$ m
		$H = 70$ m	$H = 70$ m	$H = 69$ m
		$u = 1.9$ m/s	$u = 2.0$ m/s	$u = 1.8$ m/s
3.5 m	0 m/s	Not tested	Not tested	$z = 51$ m
				$H = 60$ m
				$u = 0.3$ m/s
	2 m/s	$z = 36$ m	$z = 37$ m	$z = 36$ m
		$H = 56$ m	$H = 56$ m	$H = 57$ m
		$u = 0.3$ m/s	$u = 1.7$ m/s	$u = 1.8$ m/s
4.5 m	0 m/s[a]	$z \sim 30$ m	$z \sim 46$ m	$z \sim 46$ m
		$H = 60$ m	$H = 60$ m	$H = 61$ m
		$u = 0.3$ m/s	$u = 0.2$ m/s	$u = 0.2$ m/s
	2 m/s[b]	$z \sim 30$ m	$z \sim 30$ m	$z \sim 30$ m
		$H = 66$ m	$H = 66$ m	$H = 66$m
		$u = 2.1$ m/s	$u = 1.9$ m/s	$u = 1.9$ m/s

[a]Pressure logger data unavailable. Camera depth estimated from umbilical length.

[b]Pressure logger data unavailable. Camera depth estimated from umbilical length and wire angle for other comparable platform tests and level of ambient light (zero reading on light meters).

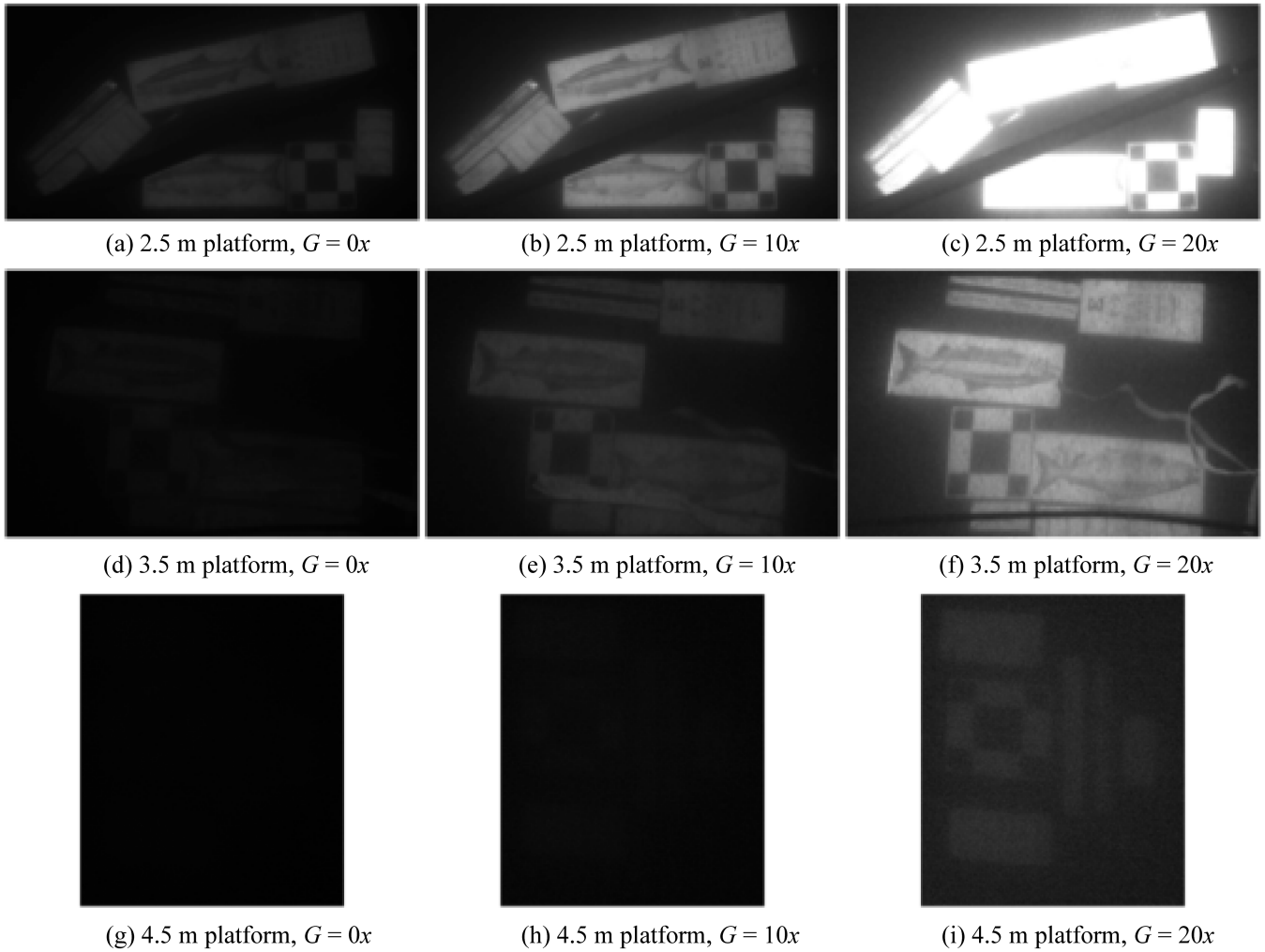

(a) 2.5 m platform, $G = 0x$ (b) 2.5 m platform, $G = 10x$ (c) 2.5 m platform, $G = 20x$

(d) 3.5 m platform, $G = 0x$ (e) 3.5 m platform, $G = 10x$ (f) 3.5 m platform, $G = 20x$

(g) 4.5 m platform, $G = 0x$ (h) 4.5 m platform, $G = 10x$ (i) 4.5 m platform, $G = 20x$

Figure 4.8: Images acquired during testing under tow (u ~2m/s) (image h detectable at full resolution on a large screen). (a) 2.5 m platform, $G = 0x$, (b) 2.5 m platform, $G = 10x$, (c) 2.5 m platform, $G = 20x$, (d) 3.5 m platform, $G = 0x$, (e) 3.5 m platform, $G = 10x$, (f) 3.5 m platform, $G = 20x$, (g) 4.5 m platform, $G = 0x$, (h) 4.5 m platform, $G = 10x$, (i) 4.5 m platform, $G = 20x$.

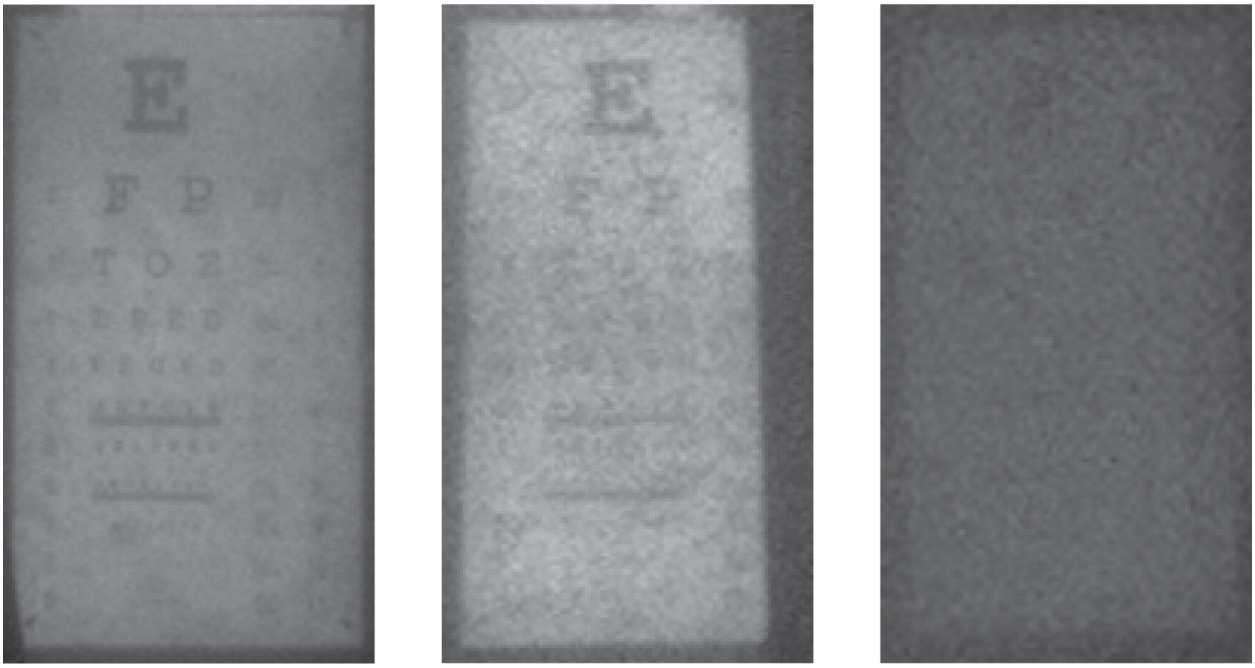

(a) 2.5 m platform, $G = 10x$ (b) 3.5 m platform, $G = 20x$ (c) 4.5 m platform, $G = 20x$

Figure 4.9: Details of eye charts (detail from same images as Figure 4.8). (a) 2.5 m platform, $G = 10x$, (b) 3.5 m platform, $G = 20x$, and (c) 4.5 m platform, $G = 20x$.

of light attenuation, backscatter, and increasing pixel size. Strobe illumination was effective at freezing motion, with the streamers captured crisply in the frame (e.g., Figure 4.8f, 3.5 m, $20x$ gain). At most camera-target separations, some degree of digital gain was required to detect the targets, though the high gain setting resulted in an over exposure of images at shorter separation distance (e.g., Figure 4.8c, 2.5 m, $20x$ gain). Flocculent was apparent in video sequences as black flecks, but the 1 m camera-strobe separation suppressed the majority of backscatter from strobe illumination. There were no distinguishing qualitative differences between images captured under tow, with a high flocculent flux through the field of view, and those captured free drifting, with a low flocculent flux.

As a point of comparison, the acoustical camera was capable of imaging the test frame and detecting streamer motion, but the two-dimensional images could, obviously, not be used to detect the static targets on the frame, as shown in Video 2 (available online, URL: http://dx.doi.org/10.1117/1.JRS.8.083633.2) for co-temporal video obtained by the

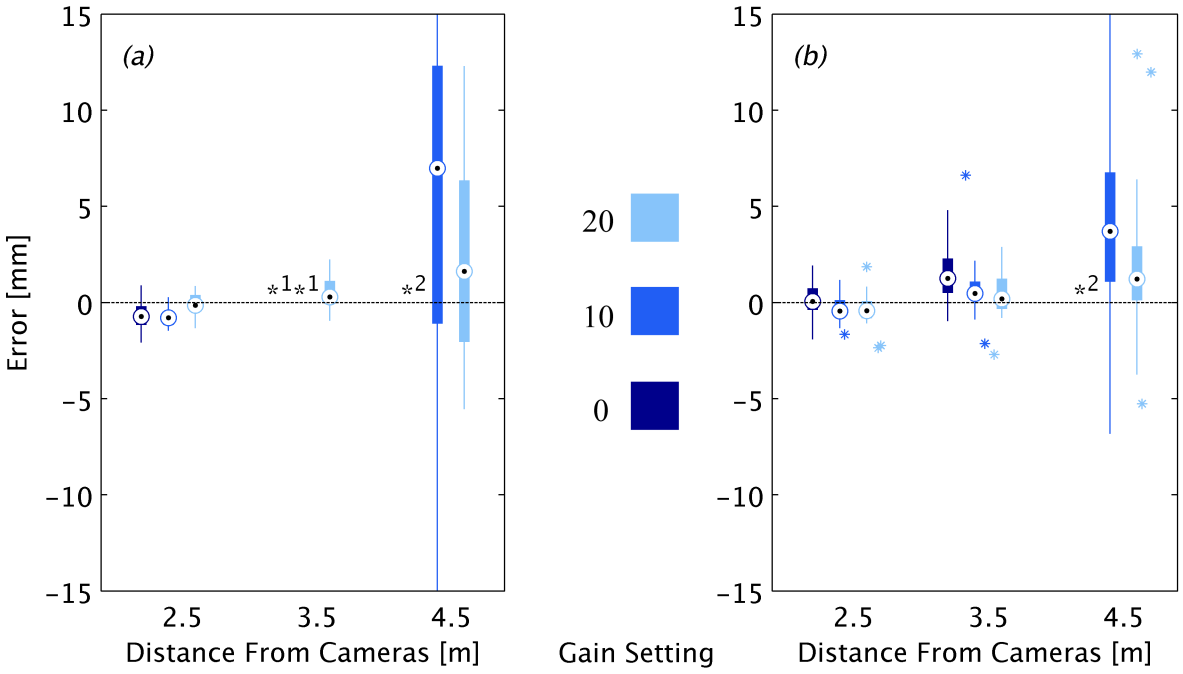

Figure 4.10: Absolute measurement error for each gain setting and camera-target separation for $N = 30$ image measurements. (a) No relative water velocity. (b) Relative water velocity of ∼2 m/s. Circles denote median values; lines denote the 25th to 75th percentile; thin bars denote the extent of measurements beyond the interquartile range; and asterisks denote outliers that are beyond 1.5 times the interquartile range. (1) Case not tested and (2) targets not visible at this gain setting.

two types of cameras.

Figure 4.10 shows absolute measurement errors in the length of one horizontal side of the 10 cm central calibration target square for 30 image pairs for each combination of gain setting and camera-target separation for the optical camera. At 2.5 m and 3.5 m camera-target separation there was a slight negative bias (length contraction) on the order of 2 mm and uncertainties were of similar magnitude. Bias may have been due to"trimming" of the black target area by over-exposure of the surrounding white space or errors in the estimates for camera system extrinsic parameters related to the calibration procedure. Although the

individual camera pixel error was an order of magnitude smaller than the observed bias, compounding biases from both cameras and the identification of corresponding positions in the image pairs may have approached 2 mm. At a separation of 4.5 m, uncertainties were higher due to the degradation in image quality and length errors could exceed 1 cm (10% of target length). As shown in Figure 4.8, images at this distance had little contrast and the precision of corner detection was reduced. Difficulty associated with identifying the same target position in image pairs with low resolution and contrast contributed to greater uncertainty in the length measurement. Measurement errors under test conditions with high relative water velocity were not markedly different from the low water velocity for the 2.5 m and 3.5 m separations. Error decreased for the 4.5 m separation for the high relative water velocity case, likely due to decreased frame depth (30 m submersion due to high wire angle for fixed length umbilical) which increased ambient light levels to $\sim$5 Lux. Consequently, ambient light was sufficient to illuminate the targets and provide additional contrast, which decreased the error beyond the anticipated conditions at turbine depth.

4.1.4.2.3 Functional Range, Sunset Bay, Puget Sound, WA During the four month endurance deployment at Sunset Bay, the camera system captured images of marine animals (e.g. small fish, harbor seals, crabs, and starfish) in varying turbidity. After heavy rainfall, turbidity would increase at the deployment site due to runoff from a nearby stream. As expected, the functional range of the camera system decreased with increasing turbidity levels. Qualitatively, elevated turbidity reduced the range of strobe illumination. Figure 4.11 shows representative imagery containing small fish (Pacific herring) in three different turbidities. These images were post-processed to increase contrast but the effect of turbidity is visible in the resolution of the printed targets that are fixed to the bottom of the frame (4.5 m camera-target separation). While the small fish were visible in all three images, their resolution decreases with increasing turbidity and they were only detectable at maximum range when they were silhouetted by the white printed targets. This imagery also demonstrated that fish are least detectable when viewed on edge due to the limited

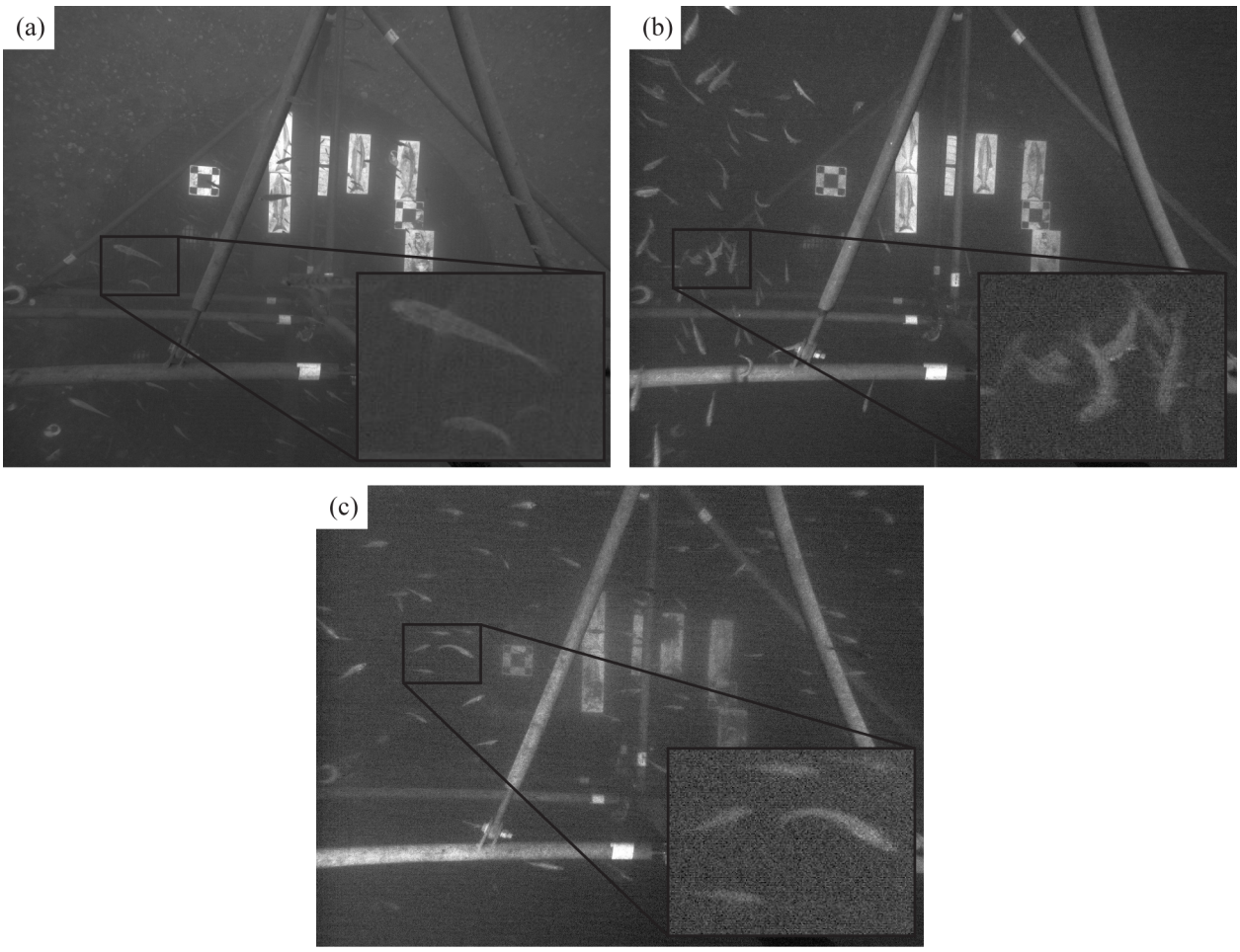

Figure 4.11: Sample imagery of small fish from endurance testing at Sunset Bay with relatively (a) low water turbidity, (b) moderate water turbidity, and (c) high water turbidity (insets show enlarged region of interest).

contrast associated with their coloration. This suggests that the most effective deployment orientation for the camera system will be one that images fish laterally.

Video 3 (available online, URL: http://dx.doi.org/10.1117/1.JRS.8.083633.3) is a slow motion sequence created from one second of imagery that captured a harbor seal foraging beneath a school of fish during the Sunset Bay deployment. The complex motion of the school of fish and seal are illustrative of the challenges associated with automatic target identification and tracking.

4.1.5 Discussion

The results of laboratory and field evaluations indicate that the stereo imaging system shows promise for performing its desired function of monitoring near-turbine inactions between the rotor and marine animals. Measurement errors of calibration squares, even at 4.5 m camera-target separation, were relatively small, $< 10\%$ of the length of expected small targets (e.g., 10 cm Pacific herring). Although the high contrast calibration targets used for measurements represented a "well behaved" target in comparison to marine animals, this quantitative evaluation demonstrated the system capabilities for ideal targets in representative environmental conditions. Measurements of live fish that vary in orientation and contrast are likely to be less accurate but should be informative for identification purposes (i.e., length errors would not increase by an order of magnitude for real targets in comparison to ideal targets). A digital gain setting between $10x$ and $20x$ appears necessary for target detection, discrimination, and classification over a range of camera-target separation distances. In our opinion, the system performed well in currents up to 2 m/s, with no obvious qualitative degradation in image quality associated with higher levels of flocculent flux. Since the testing in Admiralty Inlet was performed in August during an intended period of low water clarity it is expected that these results present a conservative picture of system performance. During periods of clear water at Sunset Bay, the 4.5 m targets were more easily visible than in Admiralty Inlet, consistent with this hypothesis.

Based on the results of field testing in Admiralty Inlet and in Sunset Bay, the anticipated capability of the optical imaging system to detect, discriminate, and classify fish targets are summarized in Table 6. Further studies are required to quantitatively evaluate system performance, but we feel that this general framework is helpful to describe functionality. "Detection" denotes the ability to locate a target in the camera field of view. "Discrimination" denotes the ability to distinguish between fish and other targets, such as woody debris or kelp. "Classification" denotes the ability to achieve a degree of taxonomic grouping. Test data indicated that visual imagery from an individual camera would be unlikely to provide

sufficient information for species-level classification at this specific location, but species-level classification may be possible if supplemented by stereographic information (e.g., length) and known patterns species presence/absence.

As part of an integrated instrumentation package, the acoustical camera is likely to be an effective complement to the optical cameras. It is likely that classification and discrimination of targets from the acoustical imagery alone would only be possible for large fish with distinctive shapes. However, as part of an integrated package, the acoustical camera could be used to characterize the behavioral response of fish to strobe illumination [*O'Driscoll et al.*, 2012] and/or as a trigger for the stereo-optical cameras when fish are within its functional range. Similarly, the acoustical camera could be used to determine the target range and select an appropriate gain setting for the optical cameras, reducing the risk of over-exposure at close range or under-exposure at distant ranges. Integration of the acoustical and optical cameras for target detection and optical camera triggering will be the subject of future studies. In particular, triggering could reduce data bandwidth and the amount of optical imagery requiring review. The volume of data produced by optical imaging systems of this type is daunting, and, disregarding the potential for behavior modification, the use of such a system in a continuous manner poses a challenge for data management. Targeted use to evaluate specific hypotheses is recommended.

Automation of target detection, measurement, and tracking will be similarly helpful to manage the potentially large datasets [*Polagye et al.*, 2014]. Future system enhancements will involve algorithm development once the system is deployed on a tidal turbine. Developing automated processing capabilities prior to deployment is not recommended due to uncertainties in site conditions throughout the year and the frequency of marine animal presence. A number of research groups are developing promising approaches for automatic classification [*Matai et al.*, 2010; *Huang et al.*, 2012], but this remains an active problem, particularly when multiple species are present in the same sequence of imagery.

Qualitative assessment of the imagery from field testing suggests that to evaluate interactions between marine animals and the turbine rotor, the imaging system should be deployed

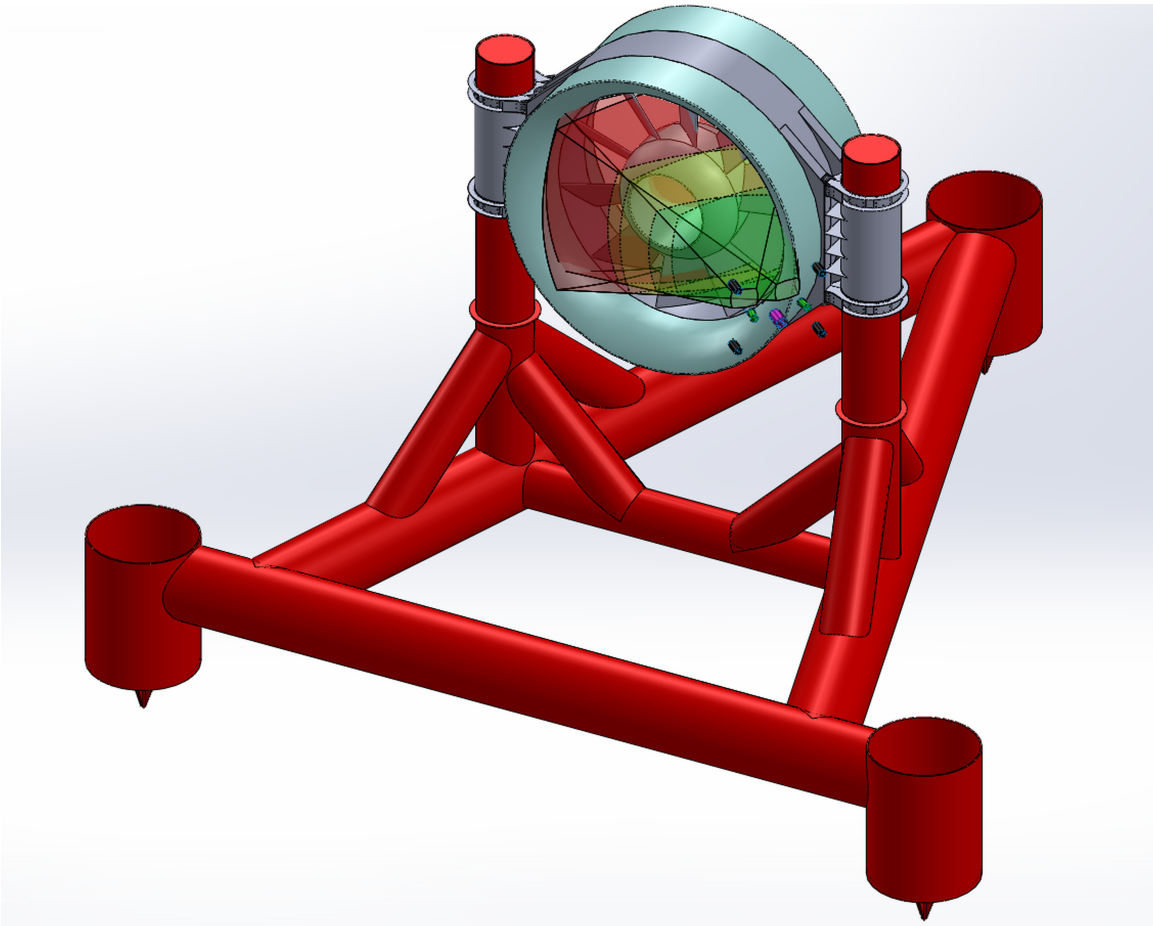

Figure 4.12: OpenHydro turbine with camera system and anticipated functional ranges. Green prism denotes range at which classification may be possible, yellow for discrimination, and red for target detection.

at turbine hub height at a slant distance of no more than 3-4 m from the turbine rotor and oriented to primarily observe fish in the lateral direction. The anticipated capabilities of an imaging system deployed in this manner are shown, conceptually, in Figure 4.12 for an OpenHydro turbine with the camera system deployed on one side at an optimum angle and distance to view the rotor. Detection may be possible over the entire rotor swept area, but discrimination and classification are only likely to be possible over a smaller portion of this region. The recovery strategy for this turbine precludes placing monitoring packages on both sides of the turbine rotor.

4.1.6 Conclusion

Environmental monitoring in the near-field of tidal turbines would ideally be able to provide continuous coverage, differentiate between target collisions with turbine blades and near-misses, allow taxonomic classification of marine animals, and not cause behavioral disturbances. The stereo-optical camera system described in this paper has the potential to meet two of these monitoring needs (differentiation between collisions and near-misses; taxonomic classification) in the conditions expected in Admiralty Inlet. In a location with persistently higher turbidity, such as the East River of New York where Verdant Power tested its turbines, the system would not likely be effective, whereas in a location with persistently lower turbidity, such as in the Orkney Islands where OpenHydro has tested its turbines, the system would be more effective. As part of an integrated instrumentation package, an acoustical camera may allow evaluation of behavioral disturbance associated with the strobe lighting and could potentially serve as a trigger for the optical cameras to enable continuous monitoring, satisfying the other two criteria. Field evaluations conducted in Admiralty Inlet and Sunset Bay demonstrated the systems ability to measure idealized targets at a range of up to 4.5 m with an accuracy of approximately 1 cm. Images of live fish at Sunset Bay demonstrate the range of image quality for live targets at various orientations as a consequence of varying turbidity. These tests suggest that the system should be able to characterize marine animal interactions with turbine blades while providing some level of taxonomic categorization over the majority of the rotor swept area. Future development and testing will include integration with an acoustical camera, the development of automated target tracking routines, and the evaluation of the systems ability to differentiate between strike/collision and a near-miss.

4.2 Biofouling on Optical Camera Ports

The text of the following chapter was published in the *Marine Technology Society Journal* in the January, 2015. With the exception of reformatting the text, no changes were made to the content of the original article. The citation for the document, pending publication, is as follows:

Joslin, J. and B. Polagye, Demonstration of biofouling methods for long term deployments of optical cameras, *MTS Journal*, 49(1), 88-96, 2015.

4.2.1 Introduction

Biofouling is often a limiting factor for long-term deployments of oceanographic optical instrumentation. While this study focuses on the fouling of camera optical ports, the methods and outcomes may be relevant to other instruments that rely on light transmission, such as absorption-attenuation meters (ac meters), photosynthetically active radiation (PAR) sensors, or fluorometers [*Manov et al.*, 2004]. The sensitivity of each optical sensor to biofouling can vary greatly and results from one instrument should not be extrapolated to another. As biological growth colonizes a camera's optical port, image quality degrades and the monitoring mission may be compromised. With the proliferation of cabled ocean observatories [*Howe and Mcginnis*, 2004; *Woodroffe et al.*, 2008; *Chave et al.*, 2009], long-term deployments of optical instrumentation are becoming more common and biofouling mitigation methods are receiving more attention. Research in this field is generally focused on improving understanding of fundamental biofouling mechanisms (such as adhesion and growth) [*Phang et al.*, 2007; *Salta et al.*, 2013] or development of biofouling mitigation measures. For example, *Manov et al.* [2004] discusses the use of copper to prolong deployments of open, enclosed or semi-enclosed, and shuttered optical instrumentation and *Debiemme-Chouvy et al.* [2011] describe applications of electrochemisty to produce a biocide on the optical port surface. *Whelan and Regan* [2006] and *Delauney et al.* [2010] provide reviews of existing biofouling

mitigation techniques and their implementation on different sensors.

Marine renewable energy, including wave, tidal and ocean current, and off-shore wind energy, is a growing sector of the electricity generation industry that requires robust approaches to biofouling. Energy converters and their support structures are deployed in the marine environment for multi-year periods and cannot expect to receive significant maintenance if their cost of energy is to be competitive with conventional forms of electricity generation. While biofouling is possible on any of the converter surfaces, general-purpose biofouling mitigation methods may be different from the approach taken for more sensitive components, such as sensor transducers. Optical camera observations have been proposed to inform a number of critical environmental questions [*Polagye et al.*, 2014] and the shore cables for the energy converters provide sufficient power and data bandwidth to support high-resolution optical measurements over extended periods. This paper discusses the implementation of biofouling mitigation measures on the optical ports of a camera system developed for long term monitoring of marine energy converters [*Joslin et al.*, 2014a]. This system will be recovered periodically for maintenance [*Joslin et al.*, 2013] and it is expected that optical port fouling will be the limiting factor for the interval between maintenance. Methods to quantitatively evaluate the effectiveness of these biofouling mitigation measures are developed and applied to a multi-month endurance test of the camera system.

4.2.2 Methodology

This section describes the deployment and layout of biofouling mitigation measures on the camera system as well as the evaluation of biofouling mitigation measure performance.

4.2.2.1 Field Deployment Configuration

Figure 4.1 illustrates the stereo-optical camera system developed for monitoring marine renewable energy converters [*Joslin et al.*, 2014a]. The integrated system combines two Allied Vision Technologies Manta G-201 machine vision optical cameras, 4 Excelitas Technologies MVS-5000 strobes and the supporting power and communications infrastructure to cable the

system to a shore station. The system is controlled in real time by a computer on shore that can adjust camera settings (e.g. frame rate, exposure time, digital gain, and strobe triggering) and archive acquired stereo imagery. The optical cameras and strobes are marinized by enclosing them in aluminum pressure housings with planar acrylic optical ports. Material selection has been shown to influence the rate of biofouling on optical ports [*Manov et al.*, 2004] and although not optimal for biofouling, abrasion resistant acrylic is used here due to its transparency for optical imagery and ease of manufacturing for integration in the pressure housings.

A multi-month field trial was conducted during early 2013 to evaluate overall system endurance (hardware performance, software stability, corrosion, and biofouling). After an initial calibration in a tank, the system was deployed from 24 January to 8 February in freshwater off of a dock on Lake Union, WA. Subsequently, the system was deployed in a saltwater environment from 3 March to 2 July off Edmonds, WA.

For the salt-water endurance trial, the camera system was mounted to the test frame shown in Figure 4.4. The Applied Physics Laboratory vessel R/V Jack Robertson lowered the test frame to the seabed in approximately 20 meters of water at a point 100 meters from shore. Mounted to this frame, the camera system was suspended 5 meters above the seabed in a downward looking orientation. The power and fiber umbilical was terminated on shore and connected to a data logging computer. Divers from the Applied Physics Laboratory at the University of Washington visually inspected the system for biofouling and corrosion on 3 March, 11 April, 3 May, and 26 June.

4.2.2.2 Biofouling Mitigation Measures

A combination of active and passive biofouling mitigation measures are implemented on the optical ports of the two camera and four strobe housings. As shown in Figure 4.13, each four-inch optical port has a ring of copper (Cu) around its perimeter, which is intended to suppress biofouling at the edge of the optical port. Each housing is also equipped with a mechanical brush wiper (Wi) manufactured by Zebra-Tech Ltd (http://www.zebra-

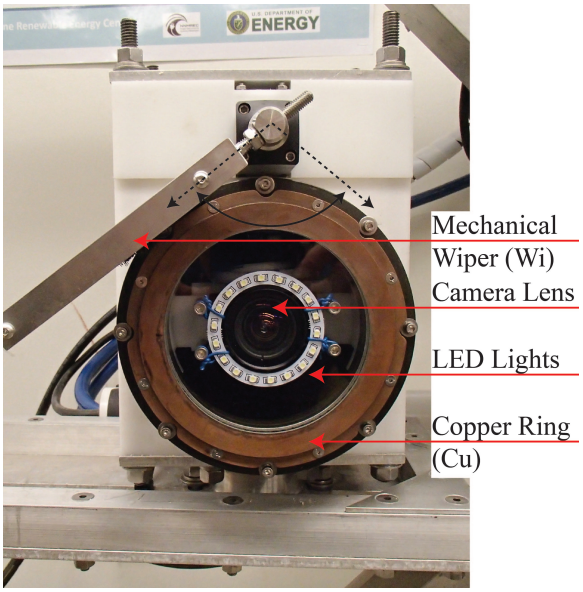

Figure 4.13: Biofouling mitigation measures on the optical camera port (pre-endurance test).

tech.co.nz/Hydro-Wiper). In addition, one of each of the camera and strobe ports is coated with the ClearSignal fouling release coating (CS) produced by Severn Marine Technologies (http://www.severnmarinetech.com/). This combination of biofouling mitigation measures is selected based on the demonstrated effectiveness of copper shutters [*Manov et al.*, 2004] and the potential additional benefit of the ClearSignal coating. Interactions between the copper, wiper, and release coating are theorized to increase the antifouling effectiveness over each measure individually. A fully shuttered system was considered but deemed undesirable for optical cameras since failure in the closed position would obviate any data collection and large shutters would be subject to significant structural loads while open in an energetic environment (wave or current). Ultraviolet lights were similarly considered but not implemented due to the uncertainty in the appropriate wavelengths for preventing fouling and limited documentation of this field in the literature [*Manov et al.*, 2004].

The wiper, when triggered by the control computer in the shore station, sweeps a 90° arc across the copper ring and optical port before reversing direction and returning to its "home" position. This action may transfer trace amounts of copper from the ring across the optical port over the course of many wipe cycles, thus increasing the effectiveness of

the wiper in isolation. This is, however, a hypothesis that was not part of the test matrix during this field trial (e.g., removing the copper ring from one of the pressure housings with a wiper). Throughout the endurance test, the wipers actuated once per hour during normal system operation. Electrical interference in the serial communications bus between the shore computer and camera system required the system to be shut down on six occasions, during which the wipers were not actuated. For the final month of the deployment, the system did not run continuously because of continued degradation of the communication bus. To continue collecting biofouling data during this period, the cameras were brought on-line manually each night to capture images. For this month, the mechanical wipers on the cameras actuated once every 24 hours and the wipers on the strobes were inactive. During this same period, the mechanical wiper on Camera 2 (CU and Wi) malfunctioned and would periodically stop in front of the optical port after a wipe cycle, thereby blocking part of the image. This did not affect the wiper's ability to remove fouling, but did complicate quantification of biofouling rates (Section 4.2.2.3). This malfunction was caused by a gradual increase in friction between the wiper and the optical port caused by fouling on the wiper brush and may be avoided by decreasing the interference spacing between the wiper brush and port.

Figure 4.14 illustrates the arrangement of the biofouling mitigation measures on the six optical ports in the system. Strobe 3 (Cu) was intended to serve as a control with minimal anti-fouling protection by disabling the wiper. However, an interruption to the bottle's power supply would cause the wiper to automatically actuate and since the system was power cycled on six occasions, the results for this optical port cannot be considered a control case.

4.2.2.3 Qualitative and Quantitative Evaluation of Biofouling Mitigation Measures

Performance of biofouling mitigation measures were monitored qualitatively during the endurance trial by diver inspections and quantitatively through the images captured by the cameras. During the inspections, the divers visually checked for the presence or absence of macro-fouling on the six optical ports and adjacent surfaces but did not disturb the surfaces

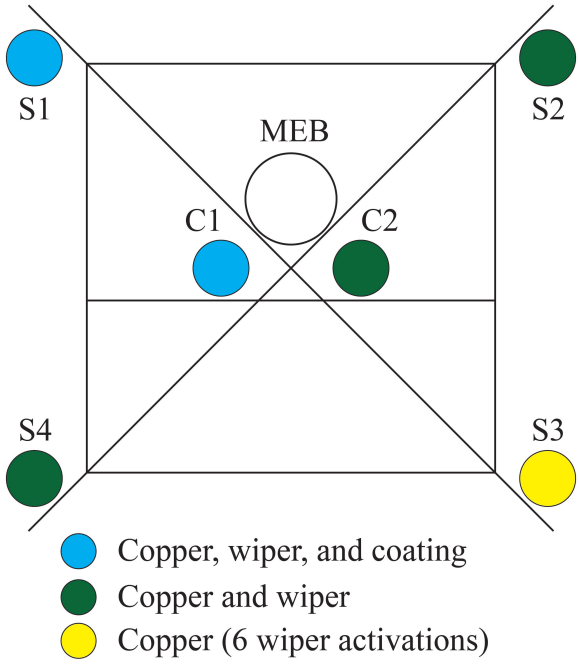

Figure 4.14: Arrangement of anti-fouling measures on camera system optical ports (S denotes strobe, C denotes camera, and MEB denotes the main electronics bottle).

or attempt to quantify the degree or type of fouling. More precise methods [AST, 2011; *Dobretsov et al.*, 2014] to quantify fouling during inspections were not attempted due to diver limitations. A final qualitative assessment of the biofouling on the system and all of the optical ports was conducted post-recovery on 2 July.

During testing, the optical cameras collected sequences of 10 images at 10 frames per second once every 15 minutes to monitor interactions between marine life and the frame (such as fish, crabs, and starfish) and provide some indication of test platform integrity between inspection dives. To monitor the biofouling levels on the camera optical ports, a ring of LED lights is installed within the camera housing, at the perimeter of the camera lens. On an hourly basis, sequences of 10 images were captured with these LEDs backlighting the optical port, as shown in Figure 4.15. Biofouling on the optical port is illuminated by the LEDs and shows increased brightness relative to clean conditions. This allows the extent and severity of biofouling to be contrasted for the two combinations of mitigation treatments

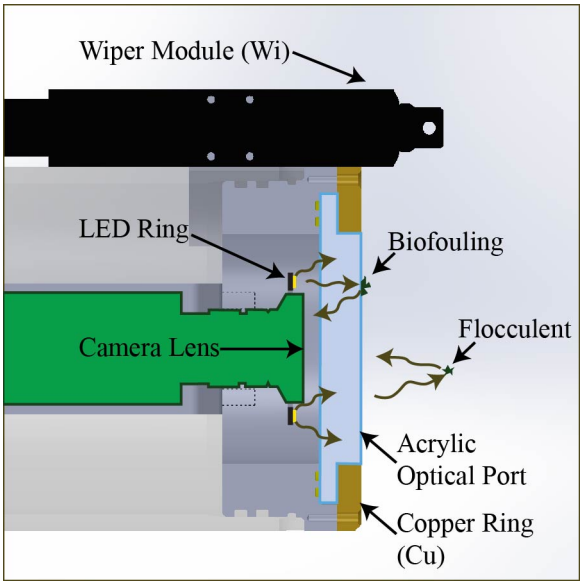

Figure 4.15: Cross-sectional schematic of camera bottle demonstrating the photon path from LED lights to camera lens as a reflection off biofouling or flocculent.

applied to the camera optical ports (Cu, Wi, and CS on camera 1 versus Cu and Wi on camera 2).

The brightness, B, of an image collected at time t, with the LED illumination activated is calculated as a summation the pixel grayscale values, $p(x,y)$ as

$$B(t) = \sum_{x=1}^{n} \sum_{y=1}^{m} p(x, y) \tag{4.11}$$

For this camera configuration, the image resolution is $n = 1624$ and $m = 1234$ with a pixel grayscale range of 0 to 255.

A time-varying biofouling metric, $F(i)$, for each acquired image is calculated as

$$F(t) = \frac{B(i) - B(0)}{B_{max} - B(0)} \tag{4.12}$$

where $B(0)$is the baseline value corresponding to the brightness levels on the first night of the deployment and B_{max} is the maximum possible brightness value ($255xnxm$). This metric takes on values between zero (for the baseline images) and unity (for a fully obscured optical port).

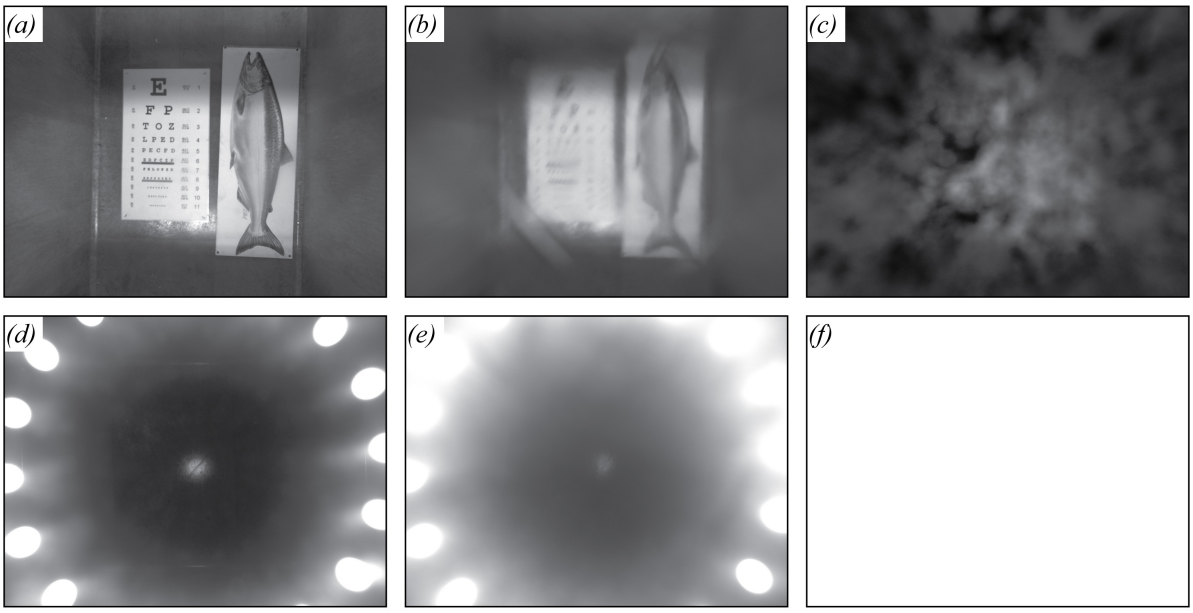

Figure 4.16: Demonstration images for biofouling metric calculations with LED backlighting. *(a) – (c)* show representative image quality for a clear optical port with the LEDs inactive *(a)*, a partially obscured ($F = 0.37$) optical port *(b)*, and fully obscured ($F = 1.0$) optical port *(c)*. *(d) – (f)* show the corresponding image brightness with the LEDs active.

Figure 4.16 demonstrates the effectiveness of this method for quantifying fouling on a camera's optical port by showing the quality of images captured with external illumination alongside images captured with the internal LED backlight for a clear ($F = 0$), blurry ($F = 0.37$), and fully obscured ($F = 1.0$) optical port. The artificial fouling in these images is simulated in the lab using a light coating of silicone grease as adhesive and fine sand to obscure the image. The maximum acceptable biofouling metric for optical images depends on the monitoring mission intended for the system. Missions requiring high image resolution (e.g., precise measurements of target size and speed using stereo processing) will have a lower threshold than simpler missions (e.g., fish detection within a few meters of the camera).

The hourly biofouling images were collected in three sets of 10 images with camera exposure times of 10 ms, 25 ms, and 50 ms. This range of exposure times is used to evaluate the method's sensitivity to camera configuration. For all three exposures, images were acquired

Figure 4.17: Camera 1 (Cu, Wi, and CS) images of biofouling on the field testing frame from *(a)* 19 March, *(b)* 15 May, and *(c)* 2 July prior to recovery.

at a rate of 1 frame per second, no digital gain was used, and the strobes were not triggered. By averaging the sets of 10 images collected each hour, the variations in backscattered light caused by moving flocculent in the water is reduced. A daily mean biofouling metric is calculated as

$$\bar{F}(t) = \sum_{t=1}^{N} \frac{F_i(t)}{N} \tag{4.13}$$

where $F_i(t)$ is the fouling metric for each image and N is the number of images used from each day. Only images collected during nighttime hours ($N \sim 80$) are used for each camera configuration to avoid the confounding effect of variable external illumination.

4.2.3 Results

The results of this evaluation are presented in this section with an overview of the field deployment and an analysis of the biofouling mitigation measure effectiveness.

4.2.3.1 Field Deployment

Diving inspections confirmed increasing macro-fouling on the test frame throughout the deployment (also observed in camera imagery), while the optical ports were observed to remain clear of fouling until the final (26 June) inspection. During this final inspection, the strobe optical ports (which were no longer being actively wiped) were observed to have varying degrees of macro-fouling while the camera ports remained clear. Figure 4.17 shows

the increasing level of biofouling on the test frame from camera images acquired over the course of the deployment.

4.2.3.2 Biofouling Mitigation Measures

Figure 4.18 shows the calculated daily mean biofouling metric for each camera from the images collected with 50 ms exposure times throughout the endurance trial. Qualitatively similar trends were observed with 10 and 25 ms exposure settings, suggesting an insensitivity to exposure time. Highlighted periods represent interruptions in system operation due to software errors, electrical interference with serial communications, and wiper malfunctions. As previously discussed, during the last month of the deployment the system operation was reduced to a short period every night such that the number of images used for the nightly average was reduced to 10 from ∼80. On three occasions during this same period, the wiper on Camera 2 (Cu and Wi) malfunctioned and partially obscured the images that were collected, preventing the calculation of a metric for that night.

The biofouling metric values shown in Figure 4.18 are consistently below 0.04, indicating that both camera optical ports remained clear throughout the deployment, consistent with diver observation and post-recovery inspection. Variation in the camera metrics is primarily attributed to changes in the water quality during the deployment because flocculent or turbidity in the water close to the optical ports is illuminated by the LED backlight and increases the value of F, without actually fouling the port. Days with F value variations during the first three months of the deployment also have increased standard deviations, indicating that the variation is within the uncertainty of the measurement. During the last month of the deployment, the F values for Camera 1 (Cu, Wi, and CS) increase without an increase in the standard deviation, indicating a true change in the signal. Camera 1 (Cu, Wi, and CS) images are consistently brighter than those from Camera 2 (Cu and Wi) and have a larger range of variation. It is hypothesized that the light diffraction through the ClearSignal coating causes a "halo effect", increasing the number of bright pixels and magnifying any variation in brightness. Images obtained with external strobe illumination

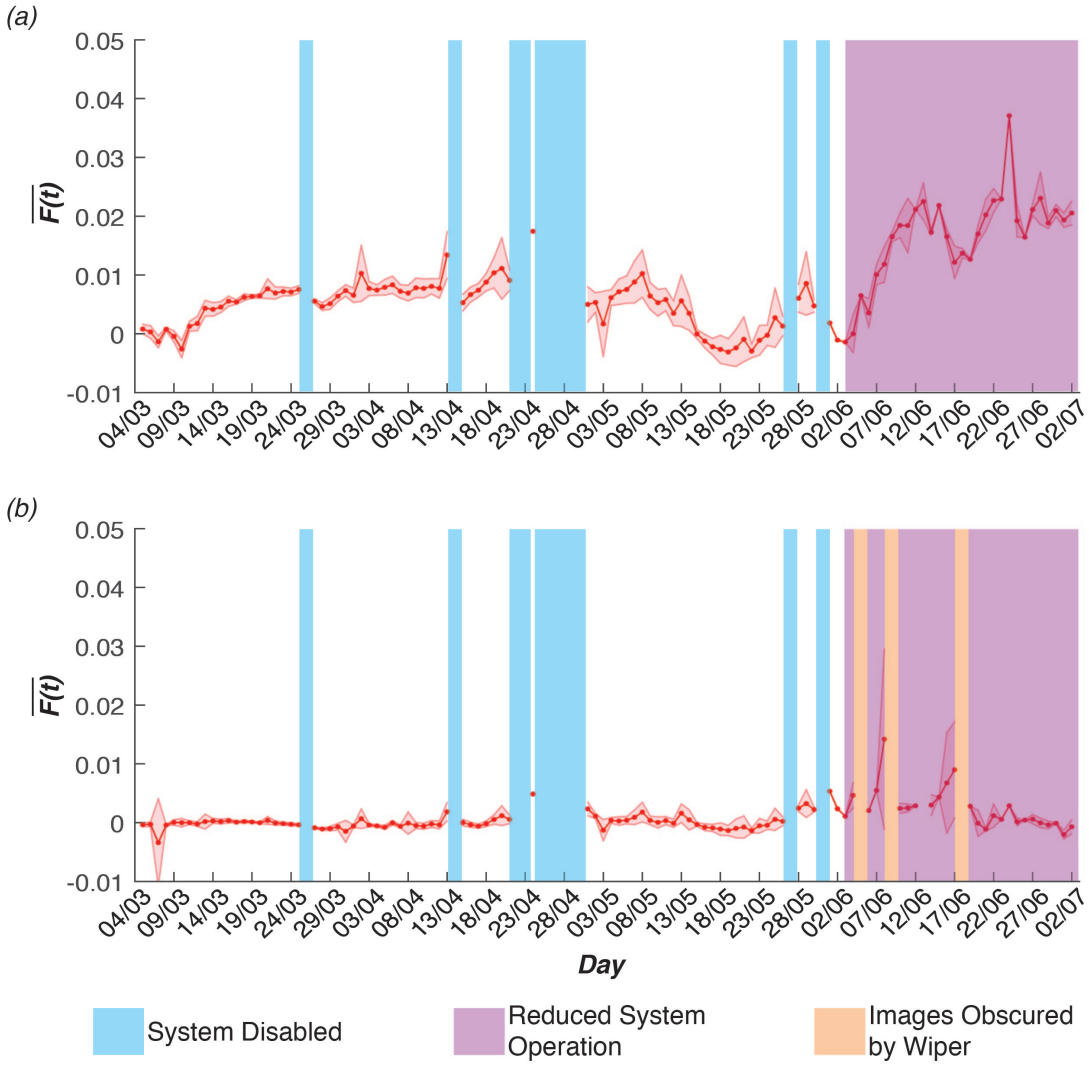

Figure 4.18: Averaged nightly biofouling metric values with shaded standard deviations on (*a*) Camera 1 (Cu, Wi, and CS) and (*b*) Camera 2 (Cu and Wi) optical ports throughout endurance test.

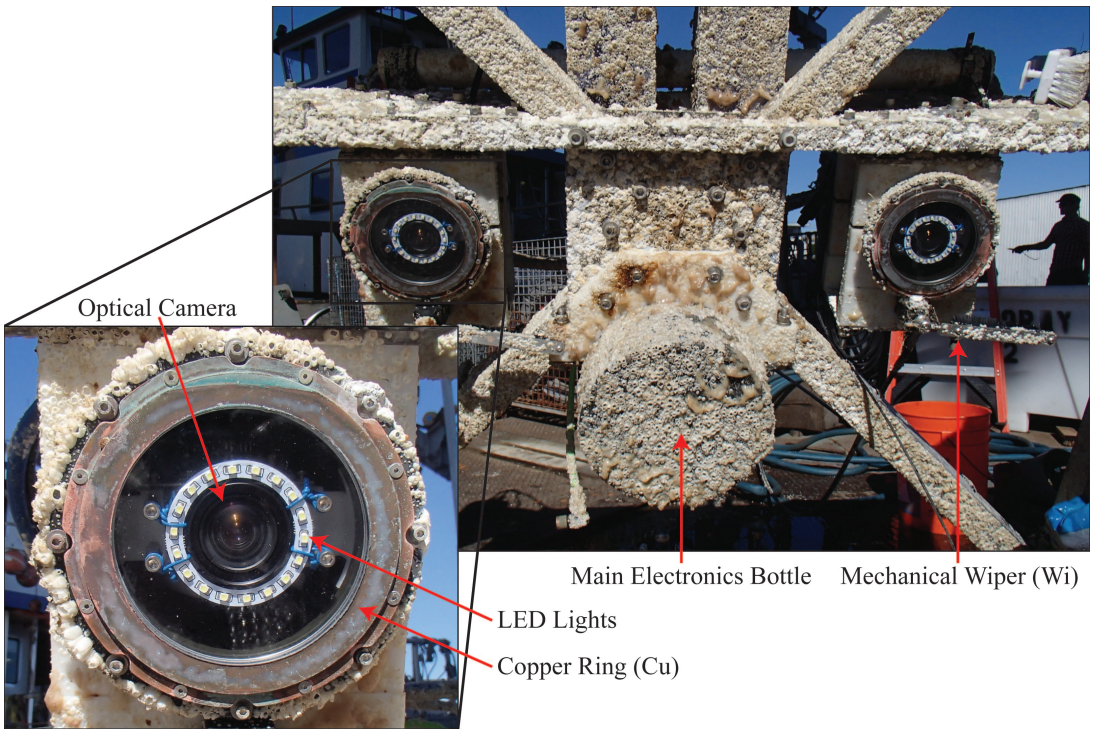

Figure 4.19: Post recovery biofouling on aluminum frame and camera optical ports.

from the coated camera port are not of markedly lesser quality than the uncoated port, so this does not suggest that the coating degrades operational effectiveness. Counterintuitively, with the wipers activated only once per day at the end of the deployment, the fouling metric increases for Camera 1 (Cu, Wi, and CS), even though one would expect that the ClearSignal coating would mitigate fouling more effectively than the bare acrylic.

Post-recovery inspection of the system revealed severe macro-fouling of every surface (including the back of the wiper blades) except for the camera optical ports. Figure 4.19 shows the center of the camera frame with a close-up view of the Camera 1 (Cu, Wi, and CS) optical port. Fouling on the system generally consisted of barnacles and algae and was independent of the surface orientation. The fouling release coating on Camera 1 (Cu, Wi, and CS) and Strobe 1 (Cu, Wi, and CS) optical ports was found to be slightly abraded (abrasion grooves in the arc of the wipers). The degradation of the coating, while not apparent in review of images acquired with strobe illumination, may have contributed to the fouling metric increase on Camera 1 (Cu, Wi, and CS) when illuminated by LED back lighting.

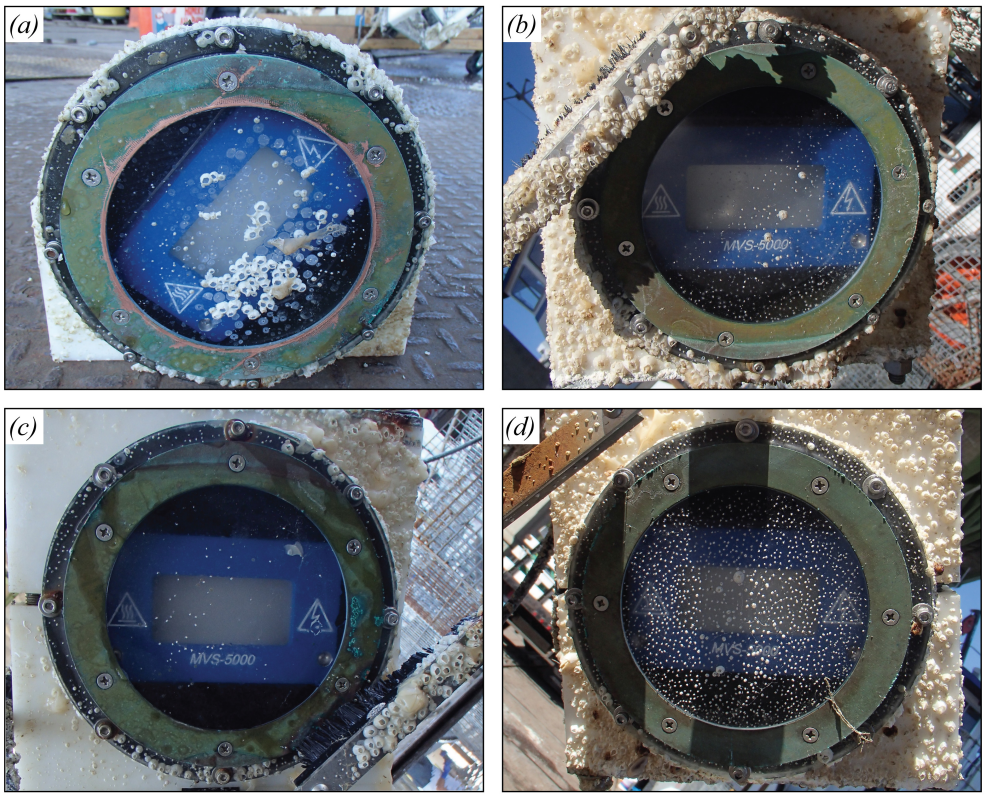

Figure 4.20: Biofouling on strobe optical ports with (*a*) Strobe 1 (Cu, Wi, and CS, though wiper rotated out of plan during test and was not effective for unknown period), (*b*) Strobe 2 (Cu and Wi), (*c*) Strobe 4 (Cu and Wi), and (*d*) Strobe 3 (Cu w/ 6 wiper actuations). Ordering identical to treatment schematic in Figure 4.14.

As the wiper abraded the coating, the diffraction of light through the coating may have changed or the surface may have become more susceptible to micro-fouling, both of which could contribute to an increase in the fouling metric for Camera 1 (Cu, Wi, and CS) over time.

The strobe optical ports, which were not monitored during the deployment, other than qualitatively for the presence of fouling by the diver inspections, are shown post recovery in Figure 4.20. Due to the wipers being disabled over the last month of the deployment for the strobes (whereas the camera wipers were still actuated once each night), all four optical ports exhibit some barnacle growth. Strobe 1 (Cu, Wi, and CS) exhibits the most growth,

though upon recovery, the wiper blade for this bottle was noted to have rotated out of the plane of the optical port, thus making it ineffective for a longer portion of the test than the wipers on the other strobe ports. Coincidentally, the Strobe 1 (Cu, Wi, and CS) optical port is also coated with ClearSignal, suggesting that the passive fouling mitigation measures (Cu and CS) would not be sufficient for multi-month deployments in adverse fouling conditions. Qualitative comparison of the camera and strobe optical ports demonstrates the effectiveness of the mechanical wiper to mitigate fouling (Figure 4.19 and Figure 4.20).

4.2.4 Discussion and Conclusions

There are expected to be strong seasonal and spatial variations in biofouling within a region the size of Puget Sound [*Dickey and Chang*, 2001]. The dates of this field deployment were chosen to span the spring and summer seasons, during which fouling is most severe. Since the endurance trial took place in calm waters with the camera system entirely within the photic zone, the biofouling observed during the trial was likely to be more severe than would occur at the anticipated deployment depth of 50 meters.

Monitoring biofouling levels on camera optical ports in a quantitative manner is complicated by the variable nature of the imagery. This method of backlighting the optical ports with LEDs in the absence of external illumination provides a means to quantify temporal changes in the optical port clarity. While there was no apparent degradation in image quality during the deployment, the biofouling metric was able to detect more subtle changes than the human eye. An upward trend in this metric could, therefore, be used to predict the need for system maintenance before the optical port is visibly degraded, thus affording more time to plan system recovery (essential in marine renewable energy environments) and reducing system downtime.

The combination of mechanical and passive biofouling mitigation methods effectively prevented macro-fouling growth that would have otherwise degraded system performance. The clarity of the camera optical ports in comparison to adjacent surfaces, as shown in Figure 4.19, is intuitively representative of this effectiveness. With no discernible difference

between the clarity of the two camera optical ports, the benefit of the ClearSignal coating was minimal under the test conditions. The abrasion of the coating by the wiper brush suggests that the combination of these two antifouling measures is potentially detrimental with a wiper actuation frequency shorter than an hour. If a system deployment were to be power constrained, and the wipers could not be run as frequently (as would be the case for an autonomous deployment), then a transparent coating may be helpful to maintain optical port clarity.

Separating the antifouling contributions of the copper rings from the wipers is difficult due to the lack of a true control. However, evaluation of the surfaces on the outside of the copper rings, which were not in contact with the wipers, suggests that the copper rings directly reduce fouling within a proximity of several millimeters. Similarly, for the optical port on Strobe 3 (Cu), which had fewer wiper activations, the most severe biofouling was at the center of the optical port, furthest from the copper ring. One hypothesis is that the presence of the ring contributed to this pattern, but without further testing it is not possible to distinguish causality from correlation.

While the mechanical wipers play an important role in biofouling mitigation, they are only effective if they do not fail themselves. Integrating the wiper mount into the camera pressure vessel to control the interference spacing between the wiper and optical port would reduce the chance of wiper failures. For the prototype system described here, the spacing was set by hand prior to deployment, which may have resulted in inconsistent interference and caused the wiper malfunctions. The modular design of the Zebra-Tech Hydrowiper allows for easy integration but caution should be taken to ensure proper and secure alignment. These modifications have been incorporated into the camera system design for the next iteration in system development [*Rush et al.*, 2014; *Joslin et al.*, 2014c].

For future deployments, measuring turbidity independently from the cameras and overlaying the measurement with the biofouling metric may allow correlations to be identified. This should be possible during subsequent system deployments, since the overall monitoring package can support additional instrumentation for an optical turbidity measurement. Bio-

fouling of this turbidity measurement must be considered similarly to the cameras to avoid confounding the results.

The clarity of images obtained during this endurance trial suggest optical camera deployments of at least four months are possible even under adverse fouling conditions with these biofouling mitigation measures. The results for these biofouling mitigation measures are consistent with the results for copper shuttered systems described in *Manov et al.* [2004], which have been shown to be effective for multi-month deployments. While the mechanical wiper does not protect the optical port by covering it between cycles like the shutter, it does not have to be activated every time data is acquired. The cleaning effect of the brush may also be greater than non-contact shuttered systems. While this result is most applicable to optical monitoring in Puget Sound, projects elsewhere involving long-term deployments of optical cameras may benefit from similar biofouling mitigation measures. Future deployments of this camera system for environmental monitoring of tidal energy projects will provide additional information about seasonal effectiveness of the measures employed.

Chapter 5

AMP AND MILLENNIUM FALCON HYDRODYNAMIC ANALYSIS

5.1 Hydrodynamic Coefficient Analysis

The text of the following chapter was submitted for publication in the *Journal of Ocean Engineering* in March, 2015. With the exception of reformatting the text, no changes were made to the content of the article. The citation for the document, pending publication is as follows:

Joslin, J., B. Polagye, and A. Stewart, Hydrodynamic coefficient analysis for an underwater vehicle, *J. Ocean Engineering*, in review.

5.1.1 Introduction

Remotely Operated Vehicles (ROVs) are able to conduct underwater operations in conditions that would be impractical or unsafe for direct human intervention. The recent growth of new marine industries, such as ocean observatories [*Howe and Mcginnis*, 2004; *Baptista et al.*, 2008; *Barnes et al.*, 2007, 2011] and marine renewable energy [*Boehlert and Gill*, 2010; *López et al.*, 2013; *Ng et al.*, 2013; *Perveen et al.*, 2014], has created new challenges and opportunities for ROV intervention [*Joslin et al.*, 2014c]. Operations at tidal current or wave energy sites, in particular, may require vehicles to maneuver in currents with non-negligible mean and turbulent components [*Thomson et al.*, 2012; *Ashton et al.*, 2014]. Ensuring that a vehicle design is able to maintain maneuverability during operations is critical. As operational challenges call for new design approaches, successful intervention strategies must rely on a model of the vehicle's hydrodynamics.

A complete hydrodynamic model of an underwater vehicle requires the centers of mass

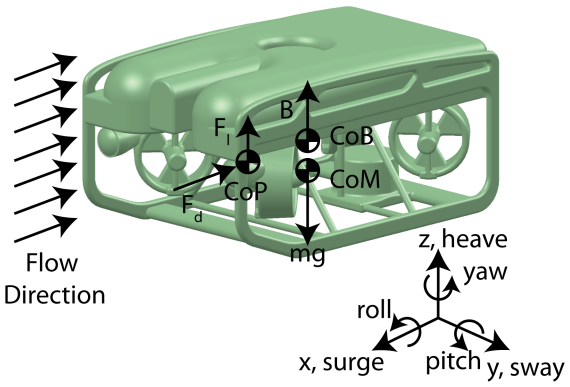

Figure 5.1: Falcon ROV free body diagram

(CoM), buoyancy (CoB), pressure (CoP) and thrust (CoT) along with the lift, drag, and added mass coefficients. Figure B.3 illustrates the approximate location of the first three centers and the axes of translation and rotation for an underwater vehicle. The centers of mass, buoyancy, and thrust can be measured from a solid model of the vehicle and are independent of the operating conditions. The center of pressure and hydrodynamic coefficients (lift, drag, and added mass) depend on the fluid flow over the vehicle and momentum imparted by the thrusters. Depending on the vehicle's symmetry and degrees of freedom, independent coefficients may exist for the three axes of translation (surge, sway, and heave; x, y, and z axes respectively) and about the three axes of rotation (roll, pitch, and yaw), as well as for coupled terms in the case of added mass, as discussed in Sec. 5.1.2. Combined with information about vehicle thrust, these parameters can be used to calculate the vehicle's response to currents and, ultimately, to design controllers that stabilize and facilitate operations [*Schjolberg and Fossen*, 1994; *Conrado de Souza and Maruyama*, 2007; *Soylu et al.*, 2010].

While all unmanned underwater vehicles (UUVs) have different geometries, the open-framed rectangular box structure is common for ROVs [*Bowen et al.*, 2004; *Elvander and Hawkes*, 2012; *Fletcher et al.*, 2009]. Syntactic foam provides buoyancy and a closed structure on the topside of the vehicle, while a lightweight open-frame is used to protect the thrusters

and create a mounting platform for the vehicle payload. Placing the vehicle's center of buoyancy above the center of mass creates passive rotational stability due to a buoyant righting moment on the pitch (y-axis) and roll (x-axis) axes (Fig. B.3). For a vehicle with this design, these two degrees of freedom may be considered approximately fixed, while the vehicle maintains the other four degrees of freedom for maneuverability. In addition, a generally symmetric shape makes translation on the surge (x-axis) and sway (y-axis) axes equivalent in the positive and negative directions.

Computational fluid dynamics (CFD) software packages can simulate fluid interactions with a solid body to estimate the lift and drag coefficients and center of pressure of underwater vehicle designs [*Long et al.*, 2008; *Jagadeesh et al.*, 2009; *Dropkin et al.*, 2011; *Eng et al.*, 2008, 2013]. Wave force interaction software, such as WAMIT (WAMIT, Inc., Chestnut Hill, MA, USA) and ShipMo (Fleet Technology Limited, Kanata, ON, Canada) can estimate the vehicle's added mass [*Eng et al.*, 2013]. In comparison to physical experiments, numerical simulations are relatively fast and inexpensive, providing complete information about the fluid interaction with the vehicle. However, the accuracy of the simulation depends on the quality of the meshed fluid domain and solution method. This can be particularly intractable for open-frame vehicles with complex geometries that are challenging to approximate.

Due to the potential for inaccuracy in CFD solutions, physical experiments are often used to verify results. Testing of vehicle designs to measure hydrodynamic coefficients may be performed in large tow tanks or flumes [*Egeskov et al.*, 1994; *Jagadeesh et al.*, 2009; *Dropkin et al.*, 2011]. In these experiments, the fluid flow is maintained at either a constant velocity or accelerated along a single axis to measure the drag coefficient or added mass, respectively. The use of specialized facilities is costly and suggests a benefit for more economical verification methods. Smaller test tank experiments have been shown to effectively estimate hydrodynamic coefficients using small amplitude oscillations on the heave axis and measuring the vehicle's depth with a pressure sensor [*Long et al.*, 2008]. With known thruster force inputs generating the oscillations, an energy balance can be used to identify the hydrodynamic coefficients on the heave axis. *Eng et al.* [2008, 2013] demonstrated the use of

free-decay pendulum motion in a small test tank to measure the coefficients on all three primary axes of translation. The pendulum position was measured from digital imagery and a least squares regression was performed on a single body pendulum dynamic equation of motion.

This paper describes numerical and experimental methods for determining the hydrodynamic coefficients of an open-framed ROV (SAAB SeaEye Falcon, Hampshire, United Kingdom). CFD simulations are performed on a simplified vehicle geometry. These simulations are inexpensive and may be performed at an early stage of design to allow for comparison and evaluation of design options prior to constructing a full-scale prototype. Free-decay pendulum experiments after *Eng et al.* [2008] are conducted in a saltwater test tank and used to measure the vehicle's added mass and verify the CFD-derived hydrodynamic coefficients. The suitability of the method is investigated through benchmarks involving simple geometric shapes (sphere and cube) and synthetic data generated by solving the pendulum equation of motion. Similarly, a geometrically simplified, one-quarter scale ROV model is constructed using rapid prototyping and 3D printing for comparison to the full-scale system.

The sections of this paper are laid out as follows. Section 5.1.2 describes the methodology, starting with a description of the general dynamic equations used for modeling an ROV. The simulation methodology for the ROV is presented in Sec. 5.1.2.2 and the experimental setup for the free-decay pendulum presented in Sec. 5.1.2.3. An analysis of two benchmark geometries is provided in Sec. 5.1.2.4 to evaluate the methods for bodies with canonical values of drag and added mass. Section 5.1.2.5 describes the application of these methods to a scale model of the ROV to evaluate scaling effects. Section 5.1.3 compares the results from the simulations and experiments. The discussion provided in Section 5.1.4 evaluates the effectiveness of these methods.

5.1.2 Methodology

The following section presents the methods used to measure the hydrodynamic coefficients, starting with a review of underwater vehicle dynamics.

5.1.2.1 Dynamic Equations of Motion for an ROV

The motion of an underwater vehicle is described by a six degree of freedom dynamic equation [*Alessandri et al.*, 1998; *Long et al.*, 2008; *Eng et al.*, 2013]. The generalized matrix form of these equations may be expressed as

$$M\dot{v} + F_C + F_D + F_G = F_T \tag{5.1}$$

where v is the linear and angular velocity vector ($\in R^{6x1}$), M is the matrix of mass and inertial terms ($\in R^{6x6}$), F_C is the Coriolis and centripetal force vector ($\in R^{6x1}$), F_D is the damping and drag force vector ($\in R^{6x1}$), F_G is the gravity and buoyancy restoring force vector ($\in R^{6x1}$) and F_T is the thruster force vector ($\in R^{6x1}$). These equations can be simplified by assuming that the system is neutrally buoyant (i.e., $F_G = 0$), and that the contribution of F_C is negligible at low speeds. For known thruster inputs, these simplifications leave only the inertial and drag forces as unknowns.

The mass and inertial matrix includes the static mass and moments of inertia of the vehicle as well as the virtual or "added" mass terms due to acceleration of fluid around the vehicle [*Lamb*, 1932; *Myers et al.*, 1969; *Streeter*, 1961; *Blevins*, 1979]. The static mass of the vehicle in air is readily measured, but the static mass must also account for fluid that is entrained within the vehicle once submerged. This entrained water contributes to the vehicles inertia, but does not scale with the vehicle's geometry in the same manner as added mass. Additional complications arise when the water entrapped within the vehicle is only partially enclosed, as is the case for an ROV design with a perforated shroud. The added mass matrix can contain up to 36 independent terms but the off diagonal terms may be negligible in some cases. For example, for an ROV with port-starboard symmetry, the added mass matrix reduces to twelve independent coefficients [*Blevins*, 1979]. The experimental methods described here are adapted from *Eng et al.* [2008] and used to measure the terms associated with the three primary axes of translation: surge, sway, and heave.

Drag forces acting on the vehicle are modeled with quadratic velocity dependence as

$$F_d = \frac{1}{2}\rho A C_d |v| v \tag{5.2}$$

where ρ is the fluid density, A is the cross sectional area normal to the axis of motion, and C_d is the drag coefficient on this axis. The drag coefficients are Reynolds number dependent, which is defined as

$$Re = \frac{\rho v L}{\mu} \tag{5.3}$$

where L is the characteristic length of the body and μ is the dynamic viscosity of the fluid. However, within the operational velocity range of interest for vehicle design, the drag coefficients are taken to be constant. For the case of an ROV with a characteristic length of 0.5 m operating in moderate currents (0.1 to 2.5 m/s), the Reynolds number ranges from 10^4 to 10^6, placing the vehicle in the transitional and turbulent regimes.

For simple translational motion along a single axis, such as surge on the x-axis, and with the assumptions given above, Eq. 5.1 reduces to a form of Morison's Equation [*Morison et al.*, 1950; *Morrison and Yoerger*, 1993]

$$(m_0 + m_{ax})\dot{v}_x - \frac{1}{2}\rho A_x C_{dx}|v_x|v_x = F_{Tx} \tag{5.4}$$

where m_0 is the static mass of the ROV and m_{ax} is the added mass due to acceleration in the x direction. With the added mass proportional to acceleration and the drag proportional to velocity, the two coefficients must be measured simultaneously for each axis or at a constant velocity to eliminate the added mass term.

5.1.2.2 CFD simulations

CFD simulations of a constant velocity fluid flow over the vehicle estimate the drag forces acting on the body without the need to conduct physical experiments. The ROV geometry for these simulations was created in ANSYS DesignModeler (ANSYS, Inc., Workbench version 14.5) from simplified SolidWorks (Dessault Systemes SolidWorks Corp., 2012 x64 Edition) models. Simplifications were made to the full-scale system geometry to prevent meshing errors (e.g., sharp corners, narrow gaps) and to achieve acceptable computational cost. The mesh was generated in ANSYS Workbench using unstructured tetrahedrons with five inflation layers on all body surfaces to form the boundary layer. Simulations solved the

Reynolds Averaged Navier Stokes (RANS) equations with steady inflow conditions. The effect of turbulence on boundary layer formation was modeled using the k-ω SST formulation, which has been shown to predict flow separation with greater accuracy than one-equation closures (e.g., Spalart-Allmaras) or other two-equation closures (e.g., k-ϵ) [Flu, 2011; *Shives and Crawford*, 2012]. Drag and lift coefficients were monitored for convergence, along with the scaled residuals of continuity, velocity, and k-ω turbulence coefficients.

Grid refinement studies determined whether a simulation result is independent of grid resolution. Three separate mesh resolutions were generated for the fluid domain around the vehicle body and evaluated for flow in the surge direction: a coarse mesh with 1.9 million elements, a medium mesh with 3.6 million elements, and a fine mesh with 5.5 million elements. Simulations for each of the three mesh resolutions converged in 1.1, 2.2, and 4.4 hours, respectively, using 6 parallel processors on a standard workstation. Wall y^+ values for each element in the mesh are defined as

$$y^+ = \frac{\rho u_* y}{\mu} \tag{5.5}$$

where u_* is the friction velocity at the nearest wall and y is the distance to the nearest wall. The ranges of these values indicated the degree to which the boundary layer was resolved and are provided in Sec. 5.1.3.1 for the three mesh resolutions. The SST k-ω turbulence closure is relatively insensitive for y+ values less than 300 [Flu, 2011]. To evaluate the Reynolds number dependency of the results, simulations were also conducted using the coarse mesh for mean flow velocities between 0.1 to 3.0 m/s (Reynolds numbers based on the ROV height from $5.8x10^4$ to $3.5x10^5$). Following these sensitivity studies, a series of simulations covering the Reynolds number range of interest were performed for the ROV in the surge, sway, and heave directions with the same meshing parameters, and approximately the same number of elements, as for the coarse mesh. For the surge and heave simulations, the fluid domain was modeled for only half of the vehicle to take advantage of symmetry and reduce solution time. The computational domain extended one meter (or two characteristic lengths) in all directions from the body except downstream where it extended to five meters to resolve

the wake. The boundary conditions on the fluid domain included a velocity inlet with 5% turbulence intensity and 0.5 meter length scale, a pressure outlet, symmetry on the four sides, and a no-slip wall condition at the vehicle surfaces.

Lift and drag forces obtained from simulations are used to calculate the center of pressure. The lift and drag coefficients, C_l and C_d, for the various components are calculated as

$$C_l = \frac{2F_l}{\rho A|v|v} \tag{5.6}$$

$$C_d = \frac{2F_d}{\rho A|v|v} \tag{5.7}$$

where F_l and F_d are the combined viscous and pressure lift and drag forces respectively (e.g., skin friction and form drag). The center of pressure is calculated by Fluent as the location where these forces act without generating a moment on the body. Figure B.3 illustrates the approximate centers and direction of the lift, drag, buoyancy and mass forces in the positive surge direction.

5.1.2.3 Free-decay pendulum experiments

The experimental process is presented in this section including setup, data collection, and data processing.

5.1.2.3.1 Experimental setup The dynamic equation of pendulum motion is relatively simple and has a rich history of use in physical experiments [*Nelson and Olsson*, 1986]. By placing the body of interest at the end of a rigid pendulum arm and measuring the free decay pendulum motion in a salt water tank, *Eng et al.* [2008] demonstrated the ability to obtain estimates for the drag force and added mass. Figure 5.2 shows the free body diagram of the pendulum experiment to characterize the ROV, broken into a two-body problem (the pendulum arm and ROV).

The pendulum arm (body 1) is a rigid metal rod approximately 2 m in length that has a mass m_1, buoyancy force B_1, and drag force F_{d1}. These forces are approximated to act about

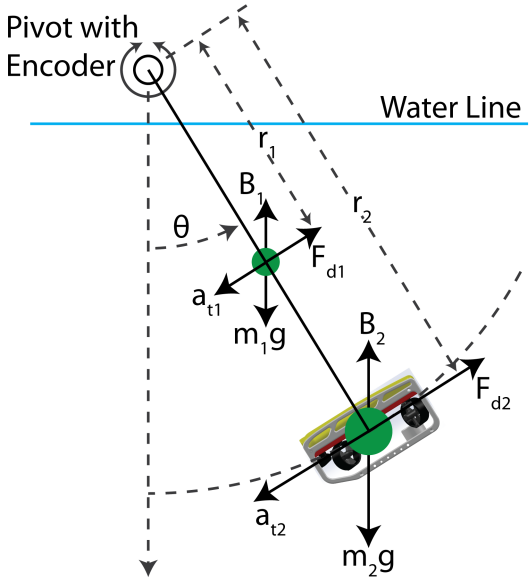

Figure 5.2: Free body diagram of the two-body pendulum experimental setup

the center of gravity that is located at distance r_1, half the length of the arm from the pivot point. The ROV (body 2) is affixed to the end of the arm and has the same corresponding forces acting at the center of mass, located at a distance r_2 from the pivot. Forces acting on the pendulum arm are measured separately from the body of interest by swinging the arm without anything attached to the end and assuming that mutual interaction between the bodies is negligible. The rotational axis of the pendulum is a shaft supported by two ball bearings that constrain the motion about a single axis. By summing the moments about this axis we find the pendulum equation of motion to be

$$\sum M_p = [(B_1 - m_1 g)r_1 + (B_2 - m_2 g)r_2]sin(\theta) + F_{d1}r_1 + F_{d2}r_2 = I\ddot{\theta} \tag{5.8}$$

where θ, $\dot{\theta}$, and $\ddot{\theta}$ are the angular position, velocity, and acceleration respectively. The moment of inertia, I, for the system is found using the parallel axis theorem for the two bodies [*Beer and Johnston*, 2004] as

$$I = \frac{4}{3}(m_1 + m_{a1}){r_1}^2 + (m_2 + {m'}_{a2}){r_2}^2 + I_{body}. \tag{5.9}$$

The quadratic drag forces are modified from Eq. 5.2 to be stated in terms of rotational velocity as

$$F_d = \frac{1}{2}\rho A C_d r^2 \theta^2 \tag{5.10}$$

where r is the distance from the pivot to the associated body's center of mass.

To achieve pendulum velocities in the operational range of interest (on the order of 1 m/s), the test body was ballasted with additional lead. For the full-scale ROV, approximately 20 kg of lead was added to the otherwise neutrally buoyant body. The required ballast was determined by numerically solving Eq. 5.8 (Matlab ODE15 solver) with approximate estimates for the hydrodynamic coefficients.

5.1.2.3.2 Data Collection The external volumes, cross-sectional areas, and body moment of inertia were calculated from a solid model of the ROV provided by the manufacturer. Weights were measured in air and in water using a hanging scale to determine the static mass and buoyancy. The water density was 1020 kg/m^3, as determined by casts with a conductivity, temperature, and depth sensor in the test tank. The mass of water enclosed within the vehicle was calculated as the difference of the expected buoyancy from the body's external volume (solid model calculation) and the measured buoyancy (scale).

The radii for each center of mass were calculated by swinging the pendulum in air, where the added mass was negligible, and measuring the period of oscillation, T. For a simple pendulum, the period is approximated as

$$T = 2\pi\sqrt{\frac{L}{g}}(1 + \frac{1}{16}{\theta_0}^2 + \frac{11}{3072}{\theta_0}^4 + ...) \tag{5.11}$$

where L is the radius of gyration and θ_0 is the initial angular position [*Nelson and Olsson*, 1986]. In the case of the pendulum arm, which is a single body pendulum, the radius of gyration is

$$L = \frac{I_{arm}}{m_1 r_1} \tag{5.12}$$

where I_{arm} is the moment of inertia for a rod pivoting about its end, or $\frac{4}{3}m_1{r_1}^2$. For the two

body system, the radius of gyration becomes

$$L = \frac{I_{arm} + m_2 {r_2}^2 + I_{body}}{m_1 r_1 + m_2 r_2} = \frac{(4/3) m_1 {r_1}^2 + m_2 {r_2}^2 + I_{body}}{m_1 r_1 + m_2 r_2} \tag{5.13}$$

which is solved for the radius of the second body, r_2.

For each test, the pendulum was raised to a position close to the water surface, the disturbance in the tank was allowed to dissipate, and then the pendulum was released. A minimum of ten pendulum releases were recorded for each of the cases tested. These cases included the two benchmark geometries, the quarter-scale model ROV in surge, sway, and heave, and the full-scale ROV in surge and sway, as well as the pendulum arms alone. Angular position was measured using an optical encoder at the pivot point. A data acquisition system (NI-DAQ 6210, National Instruments) and LabView software (National Instruments) recorded the encoder output for each pendulum release. The sensitivity of results to encoder resolution was tested using two encoders (Encoder Products Co. Accu-Coder Model 260) with resolutions of 1000 and 2540 counts per revolution.

5.1.2.3.3 Data Processing The pendulum equation of motion (Eq. 5.8) can be rearranged to the form

$$\ddot{\theta} = \alpha sin(\theta) + \beta |\dot{\theta}| \dot{\theta} \tag{5.14}$$

where

$$\alpha = \frac{(B_1 - m_1 g) r_1 + (B_2 - m_2 g) r_2}{\frac{4}{3}(m_1 + m_{a1}) {r_1}^2 + (m_2 + m'_{a2}) {r_2}^2 + I_{body}} \tag{5.15}$$

and

$$\beta = \frac{-\rho (A_1 C_{d1} {r_1}^3 + A_2 C_{d2} {r_2}^3}{2[\frac{4}{3}(m_1 + m_{a1}) {r_1}^2 + (m_2 + m'_{a2}) {r_2}^2 + I_{body}]} \tag{5.16}$$

Encoder data collected from each pendulum swing was used to calculate θ, $\dot{\theta}$, and $\ddot{\theta}$, (angular position, velocity, and acceleration). Data points for each swing were limited to the first descent of the pendulum from the initial starting point to the high point of the backswing where the velocity returns to zero. Due to the noise inherent to the digital encoder time series of position [*Belanger et al.*, 1998; *Brown et al.*, 1992], a smoothed spline was fit to the position

data points using the Matlab curve fitting toolbox and then differentiated analytically to obtain the velocity and acceleration.

The series of N data points for each swing were converted to the matrix form

$$\begin{bmatrix} \ddot{\theta}_1 \\ \ddot{\theta}_2 \\ \vdots \\ \ddot{\theta}_N \end{bmatrix} = \begin{bmatrix} sin(\theta_1) & |\dot{\theta}_1|\dot{\theta}_1 \\ sin(\theta_2) & |\dot{\theta}_2|\dot{\theta}_2 \\ \vdots & \vdots \\ sin(\theta_N) & |\dot{\theta}_N|\dot{\theta}_N \end{bmatrix} \begin{bmatrix} \alpha \\ \beta \end{bmatrix} + \begin{bmatrix} error_1 \\ error_2 \\ \vdots \\ error_N \end{bmatrix}. \tag{5.17}$$

$$\downarrow \qquad \downarrow \qquad \downarrow \qquad \downarrow$$

$$Y \qquad S \qquad Z \qquad \epsilon$$

In this form, Z was found for each swing of the pendulum through a least squares regression of the form

$$Z_{LS} = (S^T S)^{-1} S^T Y \tag{5.18}$$

where the residual errors, ϵ, [*Juang*, 1994] were

$$\epsilon = Y - \hat{Y} = Y - S^T Y \tag{5.19}$$

and the quality of the fit was determined by the standard deviation of these errors. Encoder quantization and off-axis pendulum oscillations were potential error sources in the measurement. Added mass and hydrodynamic coefficients may also be Reynolds number dependent [*Blevins*, 1979]. These effects are at odds with the assumptions used to linearize the equation of motion and the degree to which they affect the results is quantified by the residual errors.

Values for the added mass and drag coefficients are then calculated from the α and β terms of Z_{LS}. For the pendulum arms, these terms were

$$m_{a1} = \frac{3(m_1 g - B_1)}{4\alpha r_1} - m_1 \tag{5.20}$$

and

$$C_{d1} = \frac{-8\beta(m_1 - m_{a1})}{3\rho A_1 r_1} \tag{5.21}$$

and for the test body they were

$$m'_{a2} = \frac{(m_1 g - B_1) r_1 + (m_2 g - B_2) r_2}{\alpha {r_2}^2} - \frac{\frac{4}{3}(m_1 + m_2){r_1}^2 + I_{body}}{{r_2}^2} - m_2 \tag{5.22}$$

and

$$C_{d1} = \frac{2\beta[\frac{4}{3}(m_1 - m_{a1}){r_1}^2 + (m_2 - m'_{a2}){r_2}^2 + I_{body}] + \rho A_1 C_{d1} {r_1}^3}{\rho A_2 {r_2}^3} \tag{5.23}$$

The calculated value for the "added mass" of the test body, m'_{a2}, includes the mass of water enclosed within the body after submersion. The true added mass of the body (m_{a2}) was obtained by correcting for the measured mass of enclosed water, m_e, as

$$m_{a2} = m'_{a2} - m_e. \tag{5.24}$$

Statistical means and standard deviations for the coefficients were calculated from the set of pendulum swings for each orientation.

To evaluate the data processing methods and sources of error, the equation of motion (Eq. 5.8) was solved numerically (Matlab ODE15 solver) using the experimentally-derived variables and approximate starting conditions. This synthetic data was processed with the same methods as the experimental data to verify that the method recovers the correct coefficients. The errors produced by off-axis motion and Gaussian noise are similarly evaluated by adding these sources to create "noisy" synthetic data sets.

5.1.2.4 Benchmark Geometries: Cube and Sphere

In addition to the ROV, two benchmark geometries, a cube and sphere, were tested to evaluate the methods against canonical solutions. The cube was 0.151 m on edge (∼6 inches) with a fillet radius of approximately 5 mm on all edges. The sphere was 0.216 m in diameter (8.5 inches). The analytical solutions for added mass on the primary axes are

$${m_a}^{cube} = 0.7 \rho a^3 \tag{5.25}$$

for a cube with side length a [*Blevins*, 1979] and

$${m_a}^{sphere} = \frac{2}{3} \rho \pi r^3 \tag{5.26}$$

for a sphere with radius r [*Streeter*, 1961], which yield 2.46 kg and 2.69 kg for the geometries used here, respectively. These canonical solutions are for bodies in an ideal, high Reynolds number flow and may show Reynolds number dependence in other regimes [*Blevins*, 1979]. For a perfect cube, the drag coefficient on the primary axis is 1.05 for Reynolds numbers greater than 10^4, but this value decreases with the size of the edge fillet [*Schlichting*, 1955]. The drag coefficient of a sphere is a function of Reynolds number and surface roughness but is approximately 0.2 for turbulent conditions [*Schlichting*, 1955]. In the transition region between laminar and turbulent flow, experimental results in the literature show considerable scatter relative to the canonical values presented in introductory fluid mechanics texts.

CFD simulations for the cube and sphere were performed using the same configurations as for the ROV described in Sec. 5.1.2.2. The velocity input for the simulations ranged from 0.1 to 3.0 m/s. Due to the smaller size of the benchmark geometries relative to the ROV, a pendulum arm with smaller diameter (0.0125 m) but similar length (approximately 2 m) was used for their free decay experiments. Both bodies were ballasted to achieve maximum linear velocities of approximately 1.5 m/s. To avoid the complications from enclosed water, the bodies were sealed, allowed to come to equilibrium in the test tank, and weighed in air after testing to include the mass of any water that may have leaked into the body during the experiment. All other methods used for the pendulum experiments were the same as for the ROV.

5.1.2.5 Scaling Effects

Scale model experiments to verify simulation results are commonly performed at an early stage of vehicle design prior to constructing a full-scale prototype [*Eng et al.*, 2008]. Such experiments are useful because they can inform the design process and may allow for testing that would be prohibitive at full-scale. The quarter scale model of the ROV shown in Fig. 5.3 was rapid prototyped with a 3D printer from a simplified solid model and ballasted with lead. This model was similar to the one used in CFD simulations. Experimentally-derived drag coefficients were compared to the full-scale ROV at equivalent Reynolds numbers, achieved

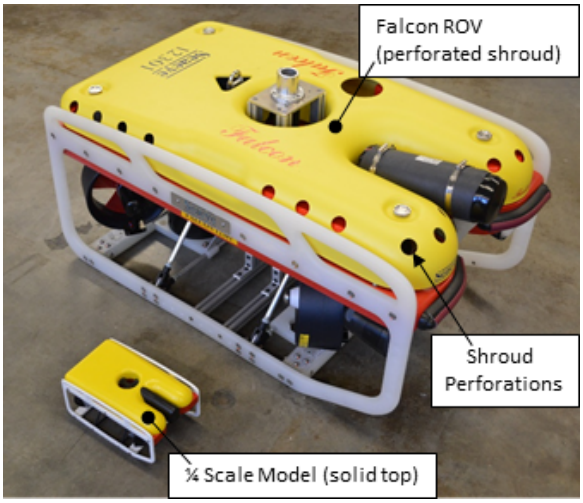

Figure 5.3: Saab Seaeye Falcon ROV with quarter scale model

by increasing the velocity of the scale model to offset the geometric reduction. Added mass is a function of the body shape, Reynolds number, and volume of displaced water. For equivalent Reynolds numbers, added mass is multiplied by the cube of the geometric scaling factor (64, for a quarter-scale model) to account for the difference in volume of displaced water [*Blevins*, 1979; *Eng et al.*, 2008].

Simulation suggested velocity independent results above 0.2 m/s (Reynolds numbers greater than $9.3\text{x}10^4$). The scale model achieved linear velocities greater than 0.8 m/s, allowing for a comparison of results in a Reynolds number range where simulation predicts velocity-independent drag coefficients. Characterization of the pendulum with the quarter scale ROV used the same smaller diameter pendulum arm as the benchmark geometries, but were otherwise identical to the full-size ROV experiments.

5.1.3 Results

The results for the determination of hydrodynamic coefficients from the CFD simulations and the free-decay pendulum experiments are presented in this section.

5.1.3.1 CFD Simulations

Table 5.1: CFD grid sensitivity study results for full-scale ROV simulations

Grid Sensitivity Study

Mesh Resolution	**Coarse Mesh**	**Medium Mesh**	**Fine Mesh**
# of Elements	1.89x10^6	3.55x10^6	5.45x10^6
Computational Cost (standard workstation)	1.1 hrs	2.2 hrs	4.4 hrs
Wall y^+ Range	0.01 to 30	0.01 to 25	0.01 to 20
Drag Coefficient	0.767	0.761	0.751
% Change from Coarse Mesh	-	0.78%	2.7%

Table 5.2: Reynolds number dependence sensitivity study results for the full-scale ROV simulations

Reynolds Number Dependence (Coarse Mesh)

Reynolds Number	**0.6x10^5**	**1.2x10^5**	**1.6x10^5**	**2.2x10^5**	**2.9x10^5**	**3.5x10^5**
Drag Coefficient	0.795	0.767	0.756	0.751	0.750	0.741
% Change from Baseline Re (1.2x10^5)	3.7%	-	1.4%	2.1%	2.2%	3.4%

The grid and Reynolds number dependence sensitivity studies showed less than 2.7 % and 3.7% variation, respectively, in the calculated drag coefficients for the ROV in the surge

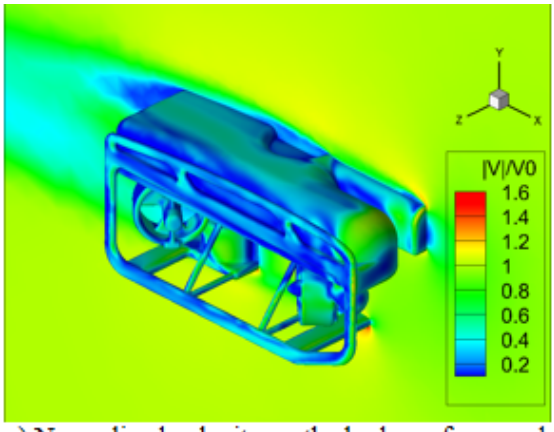

a) Normalized velocity on the body surfaces and plane of symmetry

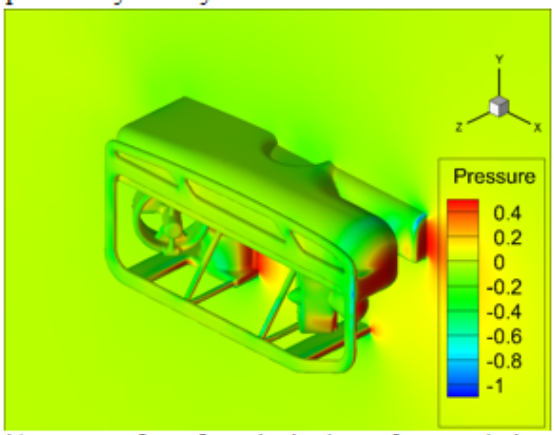

b) Pressure [MPa] on the body surfaces and plane of symmetry

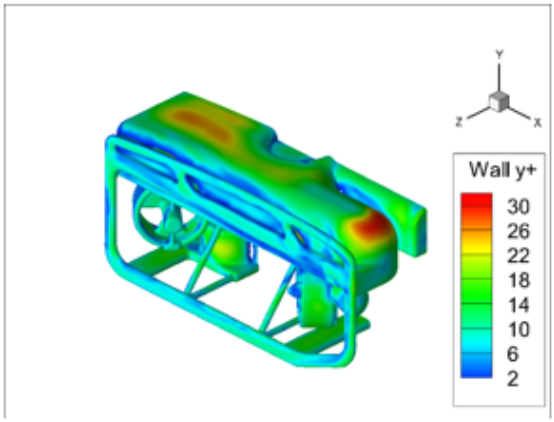

c) Wall y^+ values on the body surfaces

Figure 5.4: CFD simulation results visualizations for the full-size ROV in a 1 m/s flow in the surge direction with (a) normalized velocity on the body surfaces and along plane of symmetry, (b) pressure [MPa] on body surfaces and along plane of symmetry and (c) wall y^+ values on body surfaces

Table 5.3: CFD simulation results summary

		Drag Coefficient, C_d	**Lift Coefficient, C_l**	**CoP (in front of and above CoT) [mm]**
ROV in	Surge	0.767	0.18	(21, 9.9)
	Sway	0.880	0.17	(-56, 26)
	Heave	0.824	0.018	(6.7, 40)
Cube		0.681	0	NA
Sphere		0.188	0	NA

direction (Tables 5.1 and 5.2). For a 1 m/s flow, the coarse mesh has y^+ values of less than 30 (Fig. B.4c) which is below the recommended threshold for k-ω invariance. Consequently, the coarse meshing settings are used for all proceeding simulations to minimize computational time. While computational cost might be further reduced with an even coarser mesh, this is impractical without further simplifying the ROV geometry.

Visualizations of the CFD results for the ROV in a 1 m/s flow in the surge direction are shown for the normalized velocity, pressure, and wall y^+ values in Fig. B.4. Table 5.3 summarizes the CFD results for lift and drag coefficients, along with the center of pressure relative to the center of thrust, for each of the experimental cases in a 1 m/s flow (Reynolds number $\sim 10^5$).

5.1.3.2 Free-decay pendulum experimental results

Variables measured for each experimental case are presented in Table 5.4. The mass of water enclosed within the ROV shroud is estimated to be 47 kg. Experimental results from the two encoder resolutions tested (1000 and 2450 counts per revolution) are within 2% for the mean coefficient values, indicating minimal difference between the two encoders.

Table 5.4: Static variables for pendulum experiments

		Cross-Sectional Area, A [m^2]	**Mass, m_0 [kg]**	**Buoyancy, B [N]**	**Radius to CoM, r [m]**	**Moment of Inertia, I [kg*m2]**
Cube		0.0228	7.88	34.4	1.89	0.03
Sphere		0.0366	7.27	53.6	1.72	0.03
Scale Model in	Surge	1.0165	5.43	19.03	1.86	0.0315
	Sway	0.0240				0.0142
	Heave	0.0390			1.96	0.037
ROV in	Surge	0.310	83.06	625.9	2.28	7.72
	Sway	0.440				3.46
Large Pendulum Arm		0.0677	5.84	21.0	0.94	N/A
Small Pendulum Arm		0.0226	1.85	1.18	0.91	N/A

]

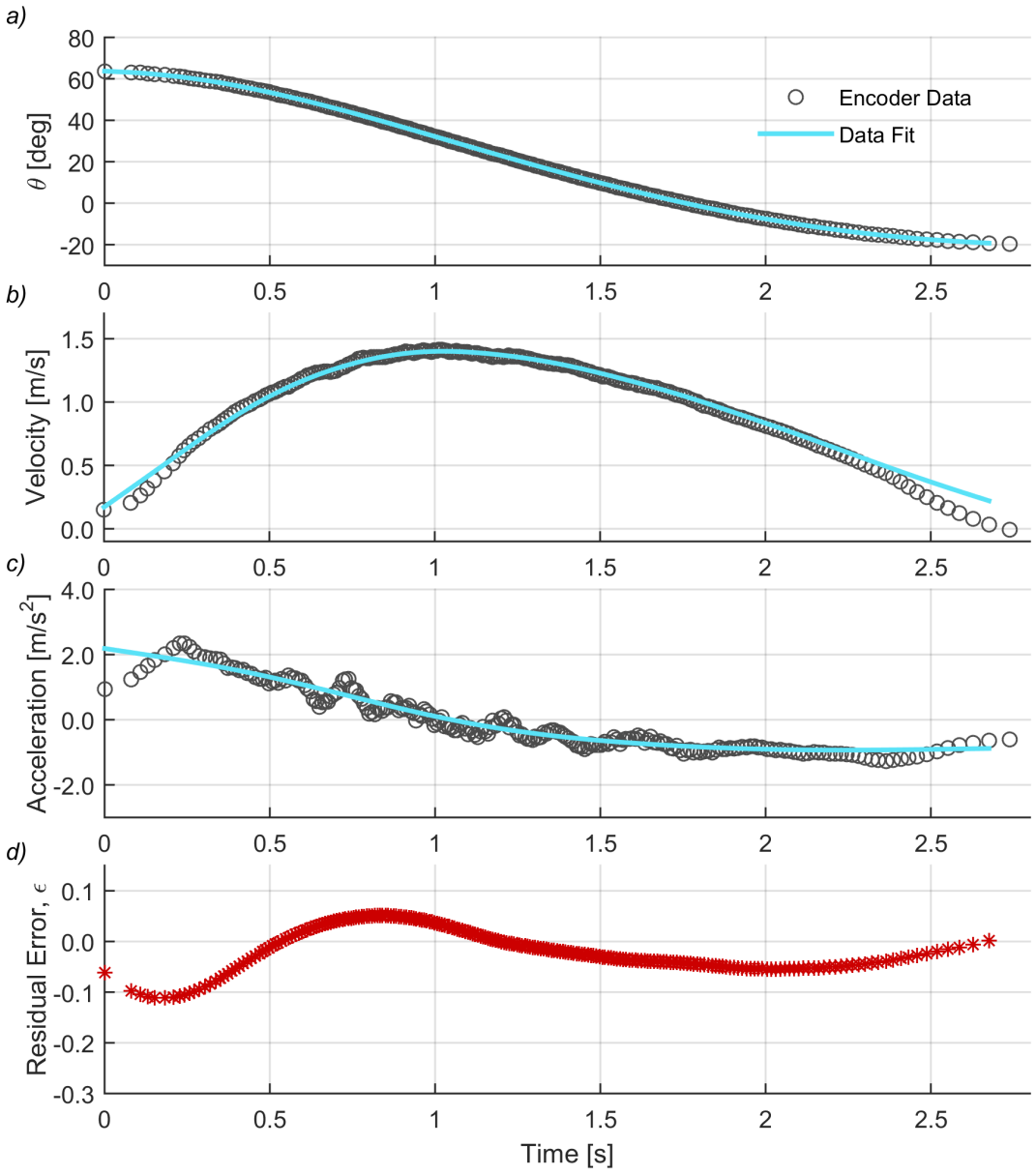

Figure 5.5: Sample data from the free-decay pendulum experiment with the sphere showing (a) angular position, (b) velocity, (c) acceleration, and (d) the residual error for each data point from the least squares regression

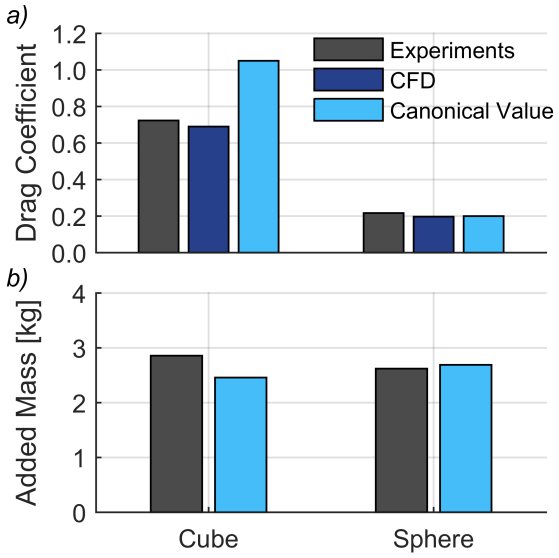

Figure 5.6: - Hydrodynamic coefficients for the benchmark geometries

5.1.3.2.1 Benchmark Geometries Pendulum swings of the cube and sphere covered a Reynolds number range based on the cube edge length and sphere diameter of up to approximately 2.5x10^5. Figure 5.5 shows a representative pendulum swing with angular position, velocity, and acceleration from the encoder along with the smoothed spline fit used for data processing, as well as the residual errors from the least squares regression (Eq. 5.19).

Figure 5.6 shows a comparison between the average experimentally derived results, the CFD simulation results, and the canonical solutions for drag coefficients (5.6a) and for the added mass (5.6b). The mean and standard deviation of these results from the 10 pendulum swings are summarized in Table 5.5 at the end of Sec. 5.1.3. The drag coefficients for the cube with filleted edges from experiments (0.723±0.035) and from CFD simulations (0.69) are less than the canonical solution (1.05) by 31 to 35%.

Numerically simulated data for pendulum swings of the sphere use a drag coefficient of 0.20 and an added mass of 2.69 kg. Processing this synthetic data with the curve fitting methods developed for the experiments produces a drag coefficient to be 0.203 and the added mass to be 2.73 kg. Both of these estimates are within 1.5% of the true values to the

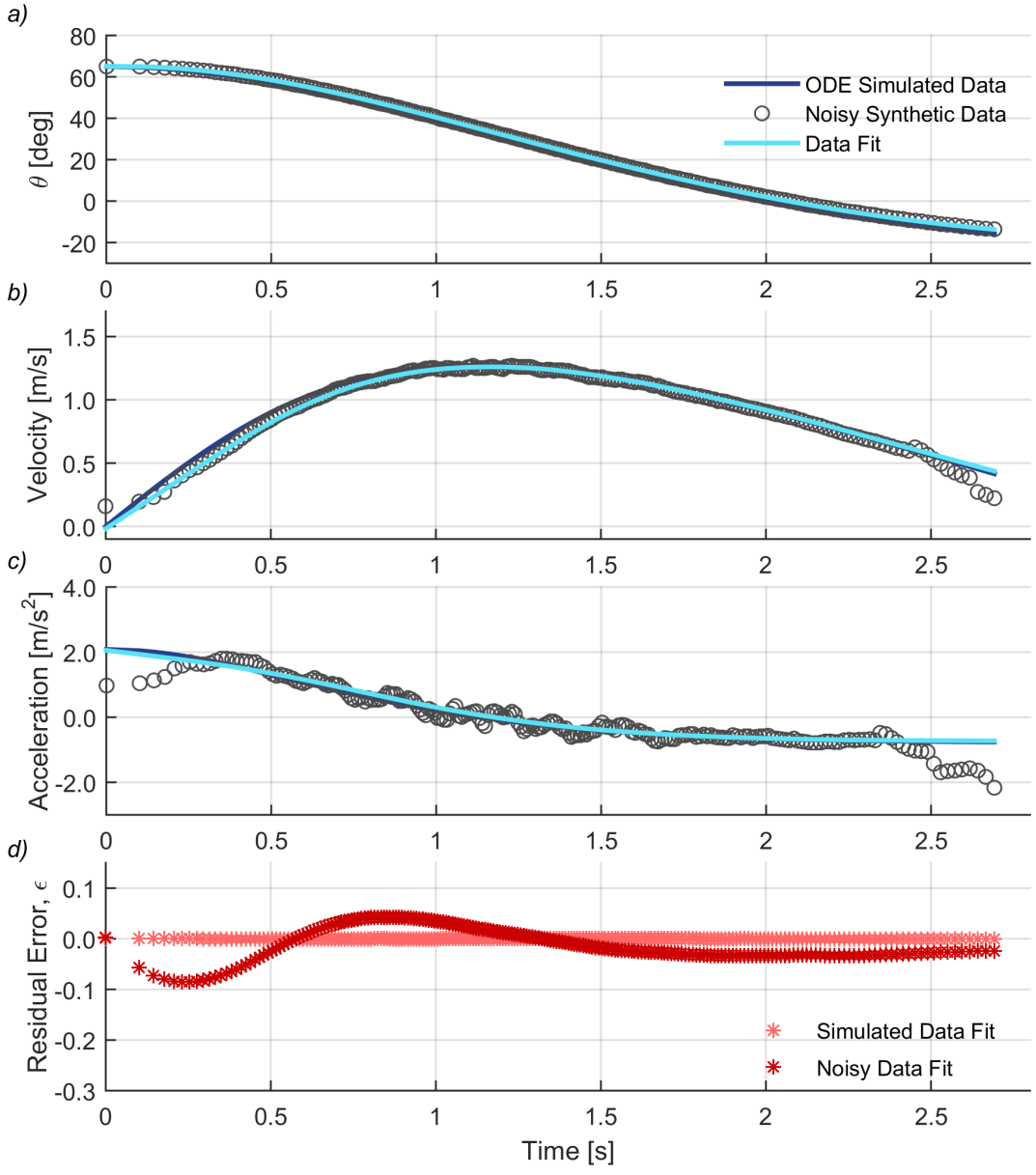

Figure 5.7: Synthetic data set for a pendulum swing of the sphere with Gaussian noise

simulation. Introducing synthetic Gaussian noise (encoder accuracy) and off-axis oscillations (small misalignment in pendulum release) to the synthetic data results in the data shown in Fig. 5.7 with estimates of 0.212 and 2.78 kg (6% and 3% greater than the true values) for the drag coefficient and added mass, respectively. The levels of noise and oscillation introduced into the synthetic data are representative of those observed in experiments.

5.1.3.2.2 ROV Figure 5.8 shows sample experimental data for a single swing of the full-size ROV in the surge direction. These results are summarized in Fig. 5.9 and Table 5.5 with the mean and standard deviation of the coefficients from each test case, along with a comparison to the CFD simulation results. As previously discussed, added mass values for the ROV do not include the mass of water enclosed within the perforated shroud (∼47 kg). Experimental results for the scale model ROV are also shown in Fig. 5.9 and Table 5.5. Added mass values for the scale-model are adjusted to the full-scale system using the $64x$ scaling factor for comparison.

5.1.4 Discussion

Free decay pendulum experiments are a relatively simple and economical method to experimentally measure added mass and drag coefficients in comparison to verification studies in a tow tank or water flume. This method does, however, require several thoughtful considerations.

5.1.4.1 Data Processing of Free Decay Pendulum Experiments

Encoder position output is inherently noisy and, in combination with off-axis oscillation, complicates differentiation to obtain rotational velocity and acceleration. By applying a smoothed spline curve fit to the position data, and analytically differentiating this fit, pendulum motion is well-resolved. Alternative methods of data filtering and curve fitting were explored as part of this analysis, and yielded almost identical hydrodynamic coefficients, but with greater residual errors. This suggests that the proposed method is robust. The

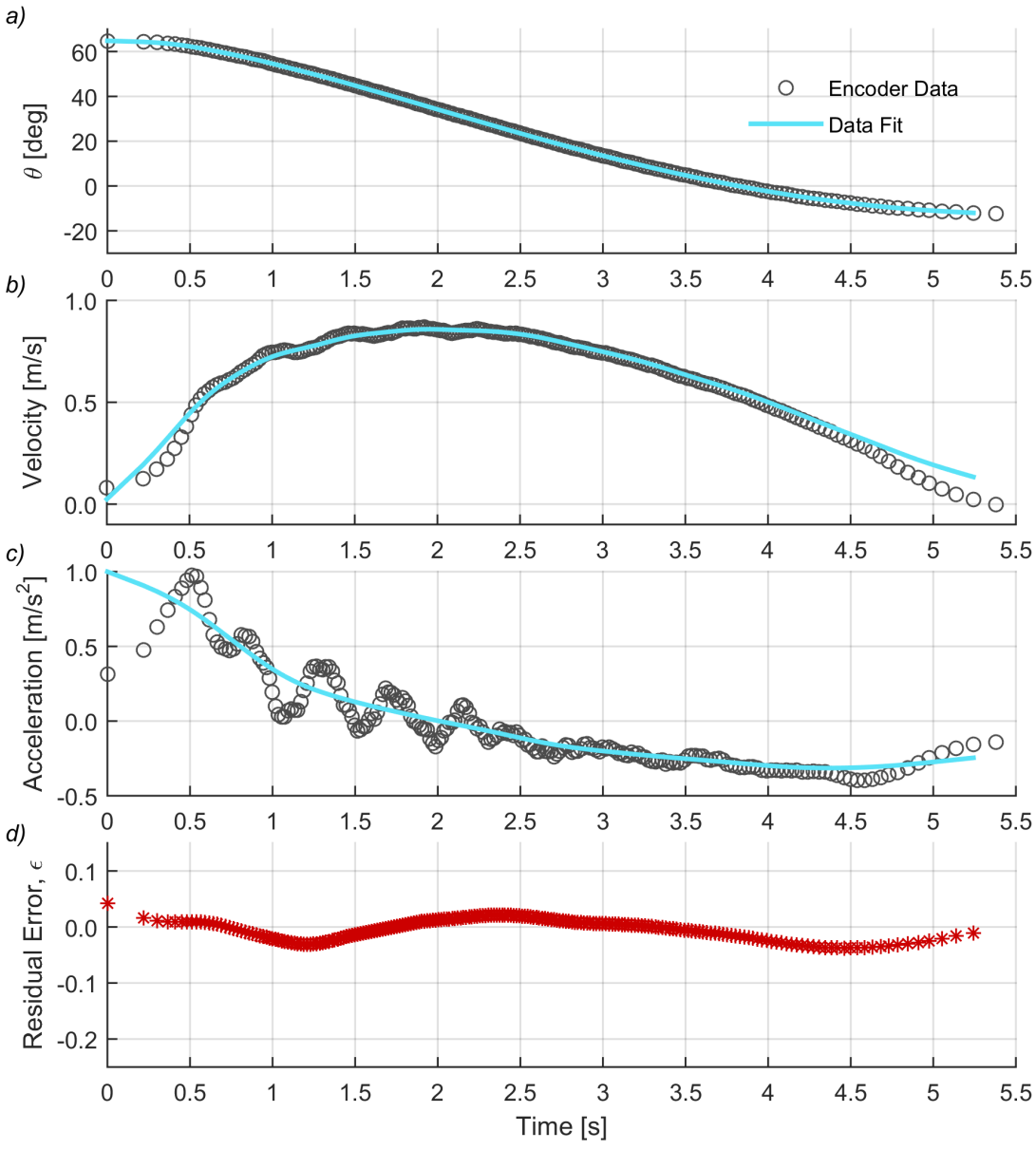

Figure 5.8: Sample data set for a pendulum swing of the ROV in the surge direction

Table 5.5: Pendulum experiment results for added mass and drag coefficients

		Added Mass, m_a [kg]		**Drag Coefficient, C_d**		
		1/4-scale	**Full-scale**	**Experimental**	**CFD**	**% Difference**
Cube		N/A	2.86±0.35	0.723±0.035	0.690	5%
Sphere		N/A	2.62±0.34	0.217±0.015	0.197	10%
Scale Model in	Surge	2.12±0.34	136±22	0.864±0.010	0.767	11%
	Sway	3.17±0.27	203±17	0.938±0.016	0.880	6%
	Heave	4.25±0.64	272±41	0.959±0.015	0.824	14%
ROV in	Surge	N/A	121±5.3	0.961±0.017	0.767	20%
	Sway	N/A	149±32.9	0.987±0.014	0.880	11%
Large Pendulum Arm		N/A	9.48±1.8	2.96±0.15	N/A	N/A
Small Pendulum Arm		N/A	2.68±0.96	2.98±0.19	N/A	N/A

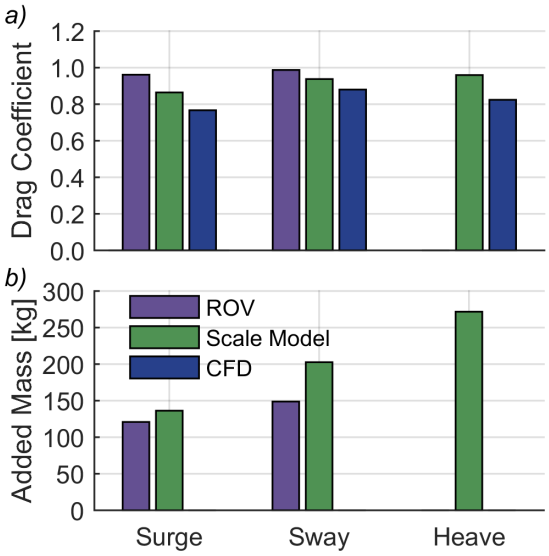

Figure 5.9: Comparison graph of the (a) drag coefficients and (b) and added mass (scaled by x64 for the scale model) from experiments with the full-size ROV, scale model, and from CFD simulations

residual errors in Fig. 5.5 and 5.7 suggest that the greatest uncertainty is during the initial, low velocity portion of the pendulum swing where off-axis oscillation is most probable. This suggests that uncertainty could be reduced by limiting the data to the latter portion of the swing. However, this initial portion has the greatest acceleration, which is necessary for accurate estimation of added mass. Estimations of added mass from data limited to the latter portion of the pendulum swing, where the acceleration is relatively small, are higher (by up to 200%) than the values estimated from the smooth spline curve fit to the entire pendulum swing.

5.1.4.2 Comparison of Experimental and Simulated Coefficients

Drag coefficients from CFD simulations are consistently lower than the experimental results (Fig. 5.6 and 5.9). The primary factors that likely contribute to this difference are model simplifications in the CFD simulations, measurement noise from encoder quantization, off-axis

oscillation of the pendulum, and Reynolds number dependence of the coefficients. Computational cost and potential numerical errors associated with adding smaller features to the CFD model limit the value of higher resolution simulations. Similarly, higher resolution encoders have a higher signal to noise ratio. Because the pendulum arm is not perfectly rigid, off-axis oscillations can occur and violate the underlying assumption of uniaxial rotation. Any off-axis motion of this sort decreases the component of the body's velocity measured by the encoder, which in turn increases the estimated drag coefficient and added mass. Off-axis motion may result from off-axis displacement when the pendulum is released or vortex shedding as the flow around the body transitions to turbulence. Finally Reynolds number dependence may result in higher drag coefficients at low velocities, but separating this effect from other sources of uncertainty at low velocity is not possible with this experimental setup. A more rigid pendulum setup might reduce off-axis motion and allow an investigation of Reynolds number dependence of the coefficients.

Analysis of the synthetic data set including encoder noise and off-axis motion show an increase in the hydrodynamic coefficients. For noiseless synthetic data, the curve fitting process increases the coefficients by $\sim$1.5% and the additional noise increased this difference to approximately 6%. This suggests that improving the experimental setup to reduce measurement noise and off-axis motion could reduce the experimentally derived coefficients and may account for a portion of the systematically higher results for experiments relative to simulation.

5.1.4.3 Benchmark Geometries

Results from the benchmark geometries demonstrate the relative effectiveness of this method for bodies with canonical solutions. Drag coefficients for a sphere in the transitional to turbulent Reynolds number regime vary with surface roughness but are generally consistent with the experimentally measured mean value of 0.217$\pm$0.015 [*Schlichting*, 1955]. The simulation results are within 0.02 or 10% of the experimental results, which verifies the simulation for these experimental conditions. For the added mass, the analytical solution for this sphere

of 2.69 kg is within 3% from the experimental solution of 2.62±0.34 kg. The numerical solution of the equation of motion using these coefficients (Fig. 5.7) matches closely to the experimental results shown in Fig. 5.5.

Given the sensitivity of spherical drag coefficients to surface roughness, the use of a cubic geometry, for which canonical solutions also exist, seems intuitively attractive. However, the high sensitivity of the drag coefficient to the sharpness of the edges of the cube renders this a poor benchmark, unless a cube with no edge fillets is available for testing. However, the drag coefficient does correspond well with the CFD simulation of a cube with filleted edges (within 5%) and the added mass is within 14% of the canonical solution for the perfect cube.

5.1.4.4 Effect of Model Scale

The measured mean drag coefficients for the quarter-scale model are up to 14% greater than the simulation results. In comparison, the full-size ROV drag coefficients are up to 20% greater. This difference may be attributed to the simplifications made to the ROV geometry for scale-model production and for the CFD simulations. For example, the shroud on the full-scale ROV is perforated to reduce the mass of water that must be accelerated with the ROV. These features are not present in the scale model or the CFD simulations, but increase the experimentally measured drag for the full-scale ROV. The quarter-scale experimental and simulation models have more limited differences, which is consistent with a smaller difference between the experimental and simulated drag coefficients. These differences may be accounted for by applying an empirical factor of safety to simulation results (e.g., increasing drag coefficients by ∼20%).

Comparison of the added mass values for the quarter-scale model and full-scale ROV requires adjustment for the mass of water entrained within the vehicle and for the volumetric scaling. The adjusted and scaled values in Table 5.5 are 11% lower in surge and 36% lower in sway for the full scale ROV relative to the quarter-scale model. As for the drag coefficient differences, this is consistent with differences between the geometry of the full-scale and quarter-scale ROV. Specifically, the perforations in the ROV shroud allow the mass of water

trapped within the vehicle to flow through the shroud, which may reduce the measured added mass.

5.1.5 Conclusions

Numerical modeling is a valuable tool in the early stages of underwater vehicle design. While verification of simulation results through experiments in a flume or tow tank can be cost prohibitive, free-decay pendulum experiments offer a potentially economical alternative. This paper demonstrates the advantages of these methods, as applied to a commercial ROV, and investigates the robustness of the method through simple geometrical benchmarks and model scaling. Methods are provided for performing CFD simulations, conducting free-decay pendulum experiments, and processing encoder data to estimate added mass and drag coefficients. Results from the analysis of the spherical benchmark show close agreement between the analytical and experimental results for added mass, as well as simulated, experimental, and canonical values for drag. Comparison of CFD and experimental results from a rapid prototyped quarter-scale model of the ROV and the full-scale vehicle shows the potential consequences of geometry simplifications and scaling. Neither method captures all of the complexities of the full-scale vehicle, such as the momentum imparted by the thrusters and the drag on the umbilical, but both can be beneficial during the vehicle design process.

5.2 Dynamic Stability Analysis

The text of the following chapter will be submitted for publication to the *Journal of Applied Ocean Research* in June, 2015. With the exception of reformatting the text and removing redundant information from the introduction, no changes were made to the content of the article to be submitted. The citation for the document, pending publication is as follows:

Joslin, J., B. Polagye, A. Stewart, and B. Fabien, Dynamic simulation of an underwater vehicle operating in turbulent currents, *J. Applied Ocean Research*, in preparation.

5.2.1 Introduction

Marine industries, such as marine renewable energy, ocean observatories, and off-shore oil and gas, rely heavily on underwater vehicles [*Elvander and Hawkes*, 2012; *Whitcomb*, 2000; *Howe and Mcginnis*, 2004; *Polagye et al.*, 2014]. As these industries expand into more energetic environments, vehicles are required to operate in areas with increasingly turbulent currents. Improved understanding of vehicle dynamics under these conditions can aid in vehicle and controller design to extend operating limits. While marine operations can often be performed by "work-class" vehicles with high (e.g., $>$ 1500 N) thrust capacities [*Yoerger et al.*, 2007; *Stoner et al.*, 2008; *Barnes et al.*, 2011], such vehicles are not always available or cost-effective, particularly for marine renewable energy applications. The optimization of "inspection-class" vehicles to perform "work-class" functions may offer a lower-cost alternative [*Christ and Wernli*, 2013]. In turbulent currents, vehicle design should be optimized to maximize stability and maneuverability within a limited thrust envelope [*Joslin et al.*, 2014b].

A common method for estimating vehicle performance is numerical simulation. Depending on the vehicle design parameter of interest, numerical simulations can model the fluid interaction with a body (computational fluid dynamics, CFD), wave interaction forces acting on a body (frequency-domain radiation and diffraction simulation), or the reaction of a body to external forces (time-domain dynamic simulation). The quality and applicability of simu-

lation results depends on the accuracy and completeness of the simulation. To fully analyze a vehicle's hydrodynamics, a combination of these simulations are generally performed along with verification experiments [*Long et al.*, 2008; *Jagadeesh et al.*, 2009; *Dropkin et al.*, 2011; *Eng et al.*, 2013].

Dynamic simulation software packages (e.g., ProteusDS by Dynamic Systems Analysis Ltd., Victoria, BC, Canada; Orcaflex by Orcina Ltd., Cumbria, UK; or WecSim by Open Energy Information) indirectly evaluate fluid-structure interactions by estimating the hydrodynamic forces acting on bodies given a prescribed current or wave forcing and solving the associated dynamic equations of motion in the time domain. These simulations can capture unsteady dynamics at low computational cost due to several simplifications. Primarily, fluid flow in the simulation is prescribed by the user and does not evolve in response to body interaction, as for CFD. This precludes interactions between body features (e.g., drag reduction in a wake region). Similarly, hydrodynamic coefficients are often estimated from canonical values for simplified geometries if experimental measurements are unavailable. Dynamic simulations of underwater vehicles have been used to evaluate designs and develop controllers for navigation and manipulation. Examples include*Prestero* [2001] for the REMUS autonomous underwater vehicle (AUV), *Evans and Nahon* [2004] for the C-SCOUT AUV, and *Jakuba et al.* [2007] for the Nereus hybrid ROV-AUV. *Antonelli* [2003] and *Wadoo and Kachroo* [2011] provide reviews of underwater vehicle modeling and motion controller design. More detailed discussion of the use of dynamic simulations in controller designs are found throughout the literature on underwater vehicles [*McMillan et al.*, 1995; *Wang and Lee*, 2003; *Loebis et al.*, 2004; *Yoerger et al.*, 1990; *Whitcomb and Yoerger*, 1999; *Soylu et al.*, 2008]. While these prior works demonstrate the efficacy of dynamic simulations, they generally assume uniform currents or neglect the effects of currents on vehicle motion.

This analysis applies ProteusDS to evaluate the performance of the AMP and deployment ROV described in Chapter 3. For tidal energy sites, slack water is ephemeral [*Thomson et al.*, 2013; *Joslin et al.*, 2014c] and the vehicle must be capable of conducting operations during limited windows of opportunity.

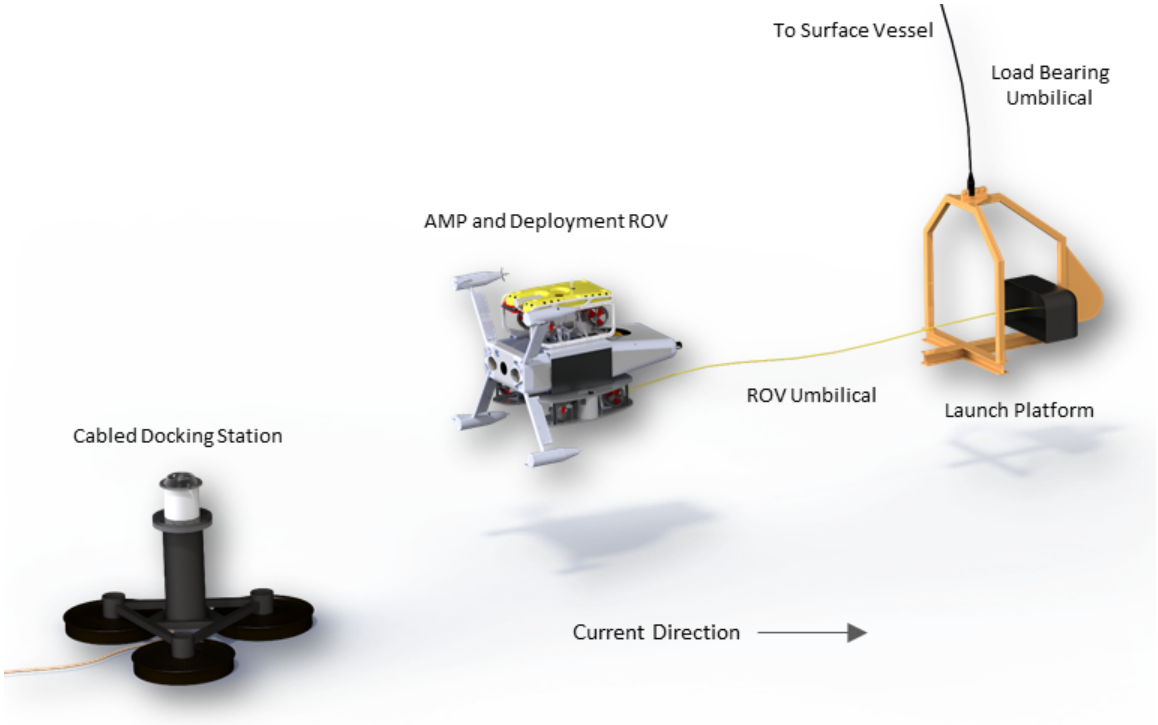

Figure 5.10: Illustration of simulated deployment operations

As discussed previously, deployment of the AMP with the Millennium Falcon ROV involves maneuvering from a launch platform to a docking station where the AMP is secured and remains for long term (e.g., multi-month) monitoring missions [*Rush et al.*, 2014; *Joslin et al.*, 2014c]. Figure 5.10 illustrates the components of this deployment operation. During the flight from the launch platform, the system is downstream of the docking station and must maintain heading and headway to reach the dock in a reasonable period of time (e.g., 5-10 minutes). The ROV umbilical is connected to the back of the skid and pays out of a tether management system located on the launch platform. By trailing the umbilical behind the ROV to the launch platform directly downstream, umbilical drag is minimized. A traveling distance of up to 30 m may be expected and a headway of 0.1 m/s is desirable to achieve a transit time of less than 5 minutes.

Turbulent current data are used to develop current forcing representative of deployments at tidal energy sites. These sites are likely to present the most challenging environment for

vehicle operations. Dynamic simulations are used to estimate the operational limits given a prescribed vehicle orientation controller and thrust capacity. In practice, this predicted limit would be used to select favorable deployment periods and operations in currents at the margin of the established limit would not be recommended.

This analysis is presented in the following sections. Section 5.2.2 presents the simulation methods, beginning with construction of the four-dimensional current forcing field from site data in Sec. 5.2.2.1. Four-dimensionally varying current fields (three-dimensional space and time) are shown to be necessary to predict thrust capacity required to maintain stability and maneuverability. An overview of the dynamic equations of motion for underwater vehicles is described in Sec. 5.2.2.2 and the parameters used to develop the vehicle model are given in Sec. 5.2.2.3. The dynamic simulations performed, including the configuration of ProteusDS and sensitivity studies, are described in Sec. 5.2.2.4. Section 5.2.3 presents the results of the simulations and interprets them in the context of future studies of vehicle operations in similar environments. ROV operations at marine energy sites has received limited attention to date. These results suggest that dynamic simulation can play an important role in optimizing designs that allow inspection-class ROVs to be used effectively in marine renewable energy applications.

5.2.2 Methodology

This section presents the methods used for the dynamic simulations of the system deployments.

5.2.2.1 Turbulent current forcing for dynamic simulations

Tidal current turbulence at marine energy sites, such as Admiralty Inlet, Puget Sound, WA (USA), have been the target of recent studies to inform the design of tidal turbines. While the intent of such studies is often to identify extreme conditions during peak mean currents (e.g., *Harding et al.* [2011]), they also can provide insight into conditions during potential ROV operations around "slack" water. *Thomson et al.* [2013] deployed a compliant mooring with

Table 5.6: Summary of current forcing data for simulations

Mean Current, $\bar{u}$ **[m/s]**	**Turbulent Intensity Range,** I
0.1	0.355-0.871
0.2	0.261-0.473
0.3	0.177-0.293
0.4	0.178-0.332
0.5	0.132-0.243
0.6	0.100-0.173
0.7	0.096-0.155
0.8	0.089-0.124
0.9	0.083-0.119
1.0	0.075-0.103
1.1	0.067-0.084

an Acoustic Doppler Velocimeter (ADV) to measure point current velocity approximately 10 m above the seabed in Admiralty Inlet for two days in June, 2012. The ADV data are collected at 32 Hz and post-processed to correct for the motion of the mooring. Motion-corrected data are binned into five minute bursts, over which time the mean current velocity is approximately constant [*McCaffrey et al.*, 2015]. The u, v, and w velocity components (x, y, and z axes, respectively, in the ROV coordinate frame in Figure 5.11) are oriented such that the direction of the mean current is aligned with the x axis. This dataset is used to generate the four-dimensional current fields for the dynamic simulations of deployment operations.

The five minute bursts are sorted by mean velocities from 0.1 to 1.1 m/s with a bin width of 0.1 m/s. Turbulence intensity, I, for each velocity bin is calculated as

$$I = \frac{\sigma}{\bar{u}} \tag{5.27}$$

where σ is the standard deviation of the current velocity magnitude and $\bar{u}$ is the mean velocity. Table 5.6 summarizes statistics for the ten five-minute data sets that are used in simulation. As the mean current increases, the turbulence intensity decreases because the standard deviation of current velocity is consistent at approximately 0.8 m/s over the range of mean currents.

The ADV data is down sampled to the simulation input time step (10 Hz) in Matlab (R2015a, Mathworks Inc., Natick, MA, USA) and filtered by a relevant length scale. Length scale filtering is performed with a low-pass filter with a cutoff frequency, f_c, estimated by Taylor's hypothesis [*Taylor*, 1937] as

$$f_c = \frac{\bar{u}}{L} \tag{5.28}$$

where L is the length scale. For this system, the turbulence of interest constitutes "engulfing gusts" which have length scales greater than the size of the vehicle (approximately 1.5 m). In dynamic simulation, the down sampled and filtered currents are taken as representative over a 100 m x 20 m $y-z$ plane, 30 m upstream of the vehicle. A sequence of frozen turbulent planes are propagated downstream (negative x-direction) with the mean currents. The resulting three dimensional field (uniform $y-z$ plane, 1 m discretization in x) defines the u, v, and w velocity components on each $y-z$ plane and at each input time step. The simulation software linearly interpolates between the defined current values in both space and time to estimate the current forcing on the vehicle at higher temporal and spatial resolution.

5.2.2.2 Underwater vehicle dynamics

Underwater vehicle dynamics are generally modelled by a Newton-Euler equation of motion for a rigid body with six degrees of freedom [*Antonelli*, 2003; *Alessandri et al.*, 1998; *Soylu et al.*, 2008]. The acceleration of the center of gravity of the rigid body is related to the forces acting on the body in a generalized matrix form as

$$M\dot{U} + F_C + F_D + F_G = F_T \tag{5.29}$$

where U is the linear and angular velocity vector ($\in R^{6x1}$), M is the matrix of mass and inertial terms ($\in R^{6x6}$), F_C is the Coriolis and centripetal force vector ($\in R^{6x1}$), F_D is the damping and drag force vector ($\in R^{6x1}$), F_G is the gravity and buoyancy restoring force vector ($\in R^{6x1}$) and F_T is the thruster force vector ($\in R^{6x1}$). Each of these terms are defined in either a global or body fixed reference frame and coordinate transformations are used to equate terms between different frames.

The location where the vector sum of each force is applied to the body is referred to as that force's center. For fully submerged bodies, the centers of mass (CoM) and buoyancy (CoB) are associated with the gravitational and buoyant restoring forces, which are constant. Buoyant forces are equal to the displaced volume of fluid and act about the center of volume of the body. The static components of the matrix of mass and inertia (M) include the body's mass (m) and moments of inertia (I_x, I_y, I_z, I_{xy}, I_{xz}, and I_{yz}), which are constants relative to the body's origin and the offset between that origin and the center of mass. Thruster forces are imparted on the vehicle at each thruster location and are prescribed by the vehicle operator or control system. Depending on the thruster configuration, centers of thrust (CoT) may be defined at the vector sum of the applied forces for each controlled degree of freedom.

Morison's hypothesis suggests that the remaining hydrodynamic forces of submerged bodies moving relative to a fluid may be represented as a simplified combination of drag and inertial forces acting on the body at the center of pressure (CoP) [*Morison et al.*, 1950]. This hypothesis neglects the potential for lift, which is assumed to be minimal for bluff bodies. For each degree of freedom, quadratic drag forces are estimated as

$$F_d = \frac{1}{2} C_d \rho A |U| U \tag{5.30}$$

where ρ is the fluid density, A is the cross sectional area normal to the fluid flow, C_d are the associated drag coefficients, and U is the relative fluid velocity. Similarly, the fluid inertial forces (F_i) are due to the added mass, which can be expressed in terms of added mass coefficients, C_a, as

$$F_i = C_a \rho V \dot{U} \tag{5.31}$$

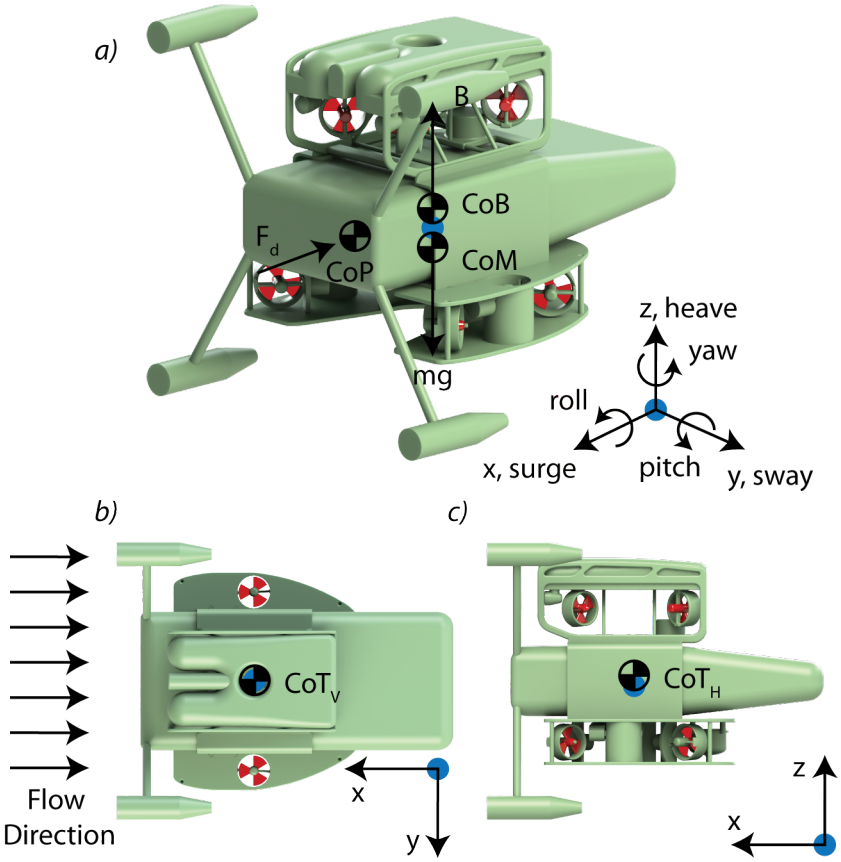

Figure 5.11: Vehicle free body diagram with thrusters highlighted in red and body origin highlighted in blue, axes and approximate centers of body forces from a (a) parametric view, (b) top view, and (c) side view

where V is the volume of fluid displaced by the body and $\dot{U}$ is the relative fluid acceleration. For underwater vehicles, these forces must be calculated for each of the six degrees of freedom. With the 6x1 velocity vector, the drag and added mass coefficients are represented by two 6x6 matrices, each containing up to 36 independent terms. For vehicles with port-starboard and fore-aft symmetry the number of independent terms is reduced to 12, and for low rotational velocities and accelerations, the forces associated with the off-diagonal coefficients may be negligible.

The complete model of an underwater vehicle uses each of these terms to calculate the

associated forces in Equation 5.29, where they act on the body, and the reaction of the body in response to these forces. Figure 5.11 shows the approximate locations of these centers along with a representative reference frame for the vehicle.

5.2.2.3 Model parameters

In dynamic simulation models, underwater vehicles are represented as a single rigid body, or an assembly of rigid bodies, for which separate parameters may be specified (e.g., vehicle and umbilical). In the presented simulations, rigid bodies are represented by meshed features created either from simple parametric shapes, such as cuboids, cylinders, or ellipsoids, or from custom geometries modelled in a separate CAD software. Meshing of the feature breaks the body surfaces into polygons for which hydrodynamic forces are calculated by applying Morison's hypothesis. The system modelled here is represented by a single rigid body for the instrumentation package and ROV with a trailing umbilical cable.

Table 5.7 summarizes the model parameters for the rigid body, as developed from measurements of a scale-model, the full-size prototype, or a solid model. The total system mass includes the dry mass of the vehicle measured in air and the mass of water entrained within the vehicle when submerged. By trimming to neutral buoyancy, the forces associated with gravity and buoyancy are equal and the mass of entrained water is calculated as the difference between the mass of the vehicle in air and the expected buoyancy due to the total external volume (measured from the solid model). The solid model is also used to calculate the moments of inertia and centers of mass, buoyancy, and thrust relative to the body origin which is assigned to the center of the docking station connection on the AMP.

For each controlled degree of freedom, the center of thrust is measured as the physical center of the thrusters that provide the control force. This simplified representation of the thruster forces assumes that each thruster contributes equally and without consideration for thruster dynamics [*Soylu et al.*, 2008]. The vehicle uses eight vectored horizontal thrusters positioned on two horizontal planes and two symmetrically oriented vertical thrusters (Figure 5.11). The vectored thruster configuration gives the vehicle control over four degrees of

Table 5.7: Vehicle parameters for dynamics simulation

Parameter			Basis	Value	Units
Water Density, ρ			Salt Water	1025	kg/m^3
System Mass, m	in Air		Measured Weight	445	kg
	Entrained Water		Solid Model	337	
	Total			782	
Buoyancy, B			Measured Weight	7674	N
Center of	Mass (x, y, z), CoM		Solid Model	(0, 0, 0.15)	m from body origin
	Buoyancy (x, y, z), CoB			(0, 0, -0.20)	
	Horizontal Thrust (x, y, z), CoT_H			(-0.04, 0, -0.03)	
	Vertical Thrust (x, y, z), CoT_V			(0, 0, 0.30)	
Moments of Inertia (about the body origin)		I_x	Solid Model	137.8	kg*m^2
		I_y		258.4	
		I_z		248.1	
		I_{xy}		0	
		I_{xz}		2.4	
		I_{yz}		0.1	
Drag Coefficients		C_{dx}	Free-decay	0.75	
		C_{dy}	Pendulum	1.04	
		C_{dz}	Experiments	1.40	
Added Mass Coefficients		C_{ax}	Free-decay	0.82	
		C_{ay}	Pendulum	0.82	
		C_{az}	Experiments	0.82	
Thrust Capacity		in Surge, F_{Tx}	Bollard	687	N
		in Sway, F_{Ty}	Thrust	579	
		in Heave, F_{Tz}	Experiments	579	

Table 5.8: Umbilical model parameters

Parameter	**Value**	**Units**
Diameter, d	0.015	m
Density, ρ	1025	kg-m^3
Normal Drag Coefficient, C_{dc}	1.5	
Skin Drag Coefficient, C_{dt}	0.01	
Added Mass Coefficient, C_{ac}	1	
Axial Rigidity, EA	2x10^6	N
Flexural Rigidity, EI	28	N-m^2
Torsional Rigidity, GJ	10	N-m^2

freedom while pitch and roll stability (i.e., rotation about the x and y axes) rely on the passive stability generated by the vehicles buoyant righting moment (separation between centers of mass and buoyancy).

Drag and added mass coefficients for the system are obtained from a combination of computational fluid dynamic (CFD) simulations and free-decay pendulum experiments with a quarter-scale rapid prototyped model[*Joslin et al.*]. While the drag and added mass coefficients form a 6x6 matrix, only the purely translational components on the three primary axes (x, y, and z) are available due to the complexity of measuring the off-diagonal terms experimentally. An approximation for off-diagonal terms in described in Section 5.2.2.4.1.

Bollard thrust measurements conducted with the Millennium Falcon ROV provide the maximum thrust capacities on the three primary axes [*Joslin et al.*, 2014c]. With the ROV tethered by a four point bridle to a fixed anchor, an in-line load cell measured the tension at full thrust along each primary axis.

Parameters for the ROV umbilical are summarized in Table 5.8. In the absence of detailed properties, these values are representative of a neutrally buoyant cable with flexibility similar

to a stranded wire rope (ProteusDS Manual) with the same diameter as the actual umbilical.

5.2.2.4 Dynamic simulations with ProteusDS

The description of the dynamic simulations with ProteusDS is presented in the following section in three parts: hydrodynamic model definition, setup and evaluation of the simulations, and sensitivity studies used to explore the simulation parameter space.

5.2.2.4.1 Hydrodynamic model The vehicle surface mesh is created in Rhinoceros 5 (McNeel North America, Seattle, WA, USA) from a SolidWorks model (Dessault Systemes SolidWorks Corp., 2014 x64 Edition). Simplifications are made to remove small and internal features that are a potential source of numerical instability, while preserving the general form factor. For accurate simulation, the body surfaces should be meshed by polygons with approximately equal surface area and minimal skew angles [Pro, 2015]. The system variables (Section 5.2.2.3) are assigned to the body in the simulations. Because the simplified model does not have identical dimensions to the actual system, hydrodynamic coefficients (drag and added mass) are multiplied by the ratios of cross-sectional area of the actual and modeled system for drag and volume for added mass. In this way, the prescribed hydrodynamic coefficients in simulation result in equivalent forces on the actual vehicle in the prescribed currents, which is necessary for the comparison against actual vehicle thrust capacity.

As only translational hydrodynamic coefficients are available, ProteusDS can approximate the rotational drag and added mass coefficients based on the body geometry. This simplification can result in inaccurate rotational force calculations for non-slender bodies [Pro, 2015], but is necessary given the difficulty of obtaining rotational coefficients experimentally. Due to the low rotational velocities and accelerations of the vehicle, the error associated with this simplification is expected to be minimal. Similarly, assigning a single drag coefficient for the translational axes of the full system simplifies the variations in drag coefficients between different components (e.g., cylindrical struts, streamlined body) [*Joslin et al.*, 2013].

To ensure the vehicle model accurately predicts the drag and added mass forces, the simulation results should be verified against physical experiments. However, collecting experimental data to match the simulations of deployment operations in turbulent currents is not feasible during the design stage and can entail substantial risk to a vehicle prototype. As a partial model verification, the free-decay pendulum experiment used to obtain the translational hydrodynamic coefficients [*Joslin et al.*] is simulated and the resulting pendulum motion is compared to the measured experimental motion.

During actual deployments, the umbilical is attached to the back end of the "Millennium" tool skid and paid out by a tether management system on the launch platform. A simple tether management system is represented in simulation as paying out or taking in umbilical to maintain a constant tension in the line. The tension is set by simulating hydrodynamic forces on the umbilical in a "worst case" scenario with the vehicle 30 m in front of the launch platform and 5 m off axis in 1 m/s uniform currents. This represents a poorly executed docking operation, in which the launch platform is not accurately deployed and the currents are likely to exceed the vehicle's thrust capacity. The maximum umbilical tension due to drag is 17 N and a conservative tensile force of 20 N is applied to the cable tension controller for simulations. By comparison, the forces acting on the vehicle in the same currents are > 600 N. Although the umbilical might be expected to significantly affect simulations, it is relative short (< 30 m) and has a maximum projected surface area only $\sim$6% of the vehicle. Also, with the umbilical connected to the back end of the tool skid, this tension helps to stabilize the system rotation by moving the center of pressure further back on the vehicle. Consequently, for the operational configuration simulated here, the umbilical is not expected to play a significant role in vehicle dynamics.

5.2.2.4.2 Dynamic simulations and operational limits In simulation, the vehicle starts at rest at its intended depth and drives against a prescribed turbulent current drawn from the cases in Table 5.6. To maintain the desired heading, headway, and depth during the simulations, proportional-integral-derivative (PID) controllers are implemented on the

Table 5.9: Controller gains

Degree of Freedom	K_p	K_i	K_d
Yaw	1000	10	5000
Surge	1500	400	0
Heave	200	0	500

associated degrees of freedom of the vehicle body (yaw, surge, and heave, respectively). While PID controllers are not optimal for autonomous navigation of underwater vehicles [*Antonelli*, 2003; *Soylu et al.*, 2008], they are implemented here as a simple mechanism to reject disturbances and maintain constant values of heading, surge velocity, and depth. For example, a more aggressive controller might make use of maximum vehicle thrust capacity to minimize flight time. This thruster implementation also neglects thruster dynamics, such as response time. For the yaw and surge controllers, both forces are generated by the vectored horizontal thrusters and the combination of forces needed for rotation and translation may not be linear on the actual system. However, current fluctuations that require large yaw corrections cannot occur simultaneously with large surge corrections due to the nature of turbulence (i.e., turbulent eddies may perturb mean flow direction or increase mean flow velocity, but cannot do both simultaneously). Controller gains given in Table 5.9 are found using the control system designer toolbox in Matlab and tuned in ProteusDS by simulating the system response to step inputs to the desired yaw angle, surge velocity, or depth. During the simulations, these controllers apply thruster forces to the degrees of freedom at the prescribed center of thrust (CoT_H for yaw and surge and CoT_V for heave), as limited by a specified thrust capacity on each axis.

For each mean current field simulated, the percent of time that the control force is at maximum capacity is calculated. For the baseline simulations (no umbilical), ten simulations are performed for each mean velocity and the percent time at capacity is calculated cumulatively. A threshold of 5% time at capacity is selected as a conservative measure of

the operational limit and the mean current at this point is found by linearly interpolating between the simulated mean currents. For the horizontal thrusters, the total thrust (F_{Th}) is calculated as

$$F_{Th} = F_x + \bar{r}T_x \tag{5.32}$$

where F_x is the surge control force, $\bar{r}$ is the average radius to the horizontal thrusters, and T_z is the yaw control torque. The thrust needed to maintain depth, as well as the passive stability on the pitch and roll axes, is similarly evaluated to assure stability is maintained for all degrees of freedom. The operational limit calculation excludes initial system acceleration from rest (conservative, because the controller takes ∼10 seconds to ramp up thrust forces). The simulation concludes when the vehicle leaves the prescribed current field. Although the turbulence data is collected in 300 second bursts, by prescribing the time series to the three dimensional field, the time that the vehicle is within the fully defined field is shortened. This occurs because the simulation starts only after the propagated currents reach the origin (initializing the entire field) and because the vehicle is advancing at approximately 0.1 m/s from the origin. Depending on the mean current velocity, which defines the rate at which the field is propagated, and the advancement of the vehicle, the system will leave the defined current field after varying lengths of time. For each simulated mean current velocity, the vehicle spends between 140 to 275 s in the prescribed current field.

5.2.2.4.3 Parameter sensitivity studies As previously described, the vehicle can be modeled with the umbilical paying out from a constant-tension tether management system. While this is the most complete representation of deployment operations, modeling the umbilical is computationally expensive and only one simulation is performed for each mean current case. These five-minute simulations have an average run time of 46.7 hours on a standard workstation computer. Due to the constantly changing umbilical forces, the numerical integrator uses a small time step ($\sim 10^{-6}$ s) to maintain stability. This time step is dynamically adjusted to regulate the integration truncation error, which is inherently less stable for simulations with turbulence. Without the umbilical, these same simulations have

Table 5.10: Hydrodynamic coefficients for parameter sensitivity studies

		Canonical Estimates	**CFD Results**	**Experimental Results**
Drag Coefficients	C_{dx}	0.8	0.63	0.75
	C_{dy}	1.05	0.84	1.02
	C_{dz}	1.05	1.17	1.40
Added Mass Coefficients	C_{ax}	0.57	NA	0.82
	C_{ay}	0.86	NA	1.41
	C_{az}	1.15	NA	2.09

an average run time of 0.5 hours. To characterize umbilical effects, additional simulations are performed both without the umbilical and with a constant tension force acting on the ROV at the umbilical connection point. This constant tension is set to the same value (20 N) as the umbilical tension controller and represents a simplified umbilical force acting on the ROV.

Sensitivity studies for the predicted operational limit are performed on model parameters, including the model mesh resolution for the vehicle body, the controller update rate, the length scale used for turbulence filtering, inclusion of turbulence in the simulations, and the vehicle hydrodynamic coefficients. Drag and added mass coefficients are varied as combinations of the experimentally measured values, approximate canonical values for a rectangular solid [*Blevins*, 1979], or CFD derived values (drag only), as shown in Table 5.10. Each of these studies is simulated without the umbilical and with the same set of turbulent current fields as for the umbilical sensitivity study.

5.2.3 Results and discussion

The results from the dynamic simulations are presented in this section for each of the simulated cases.

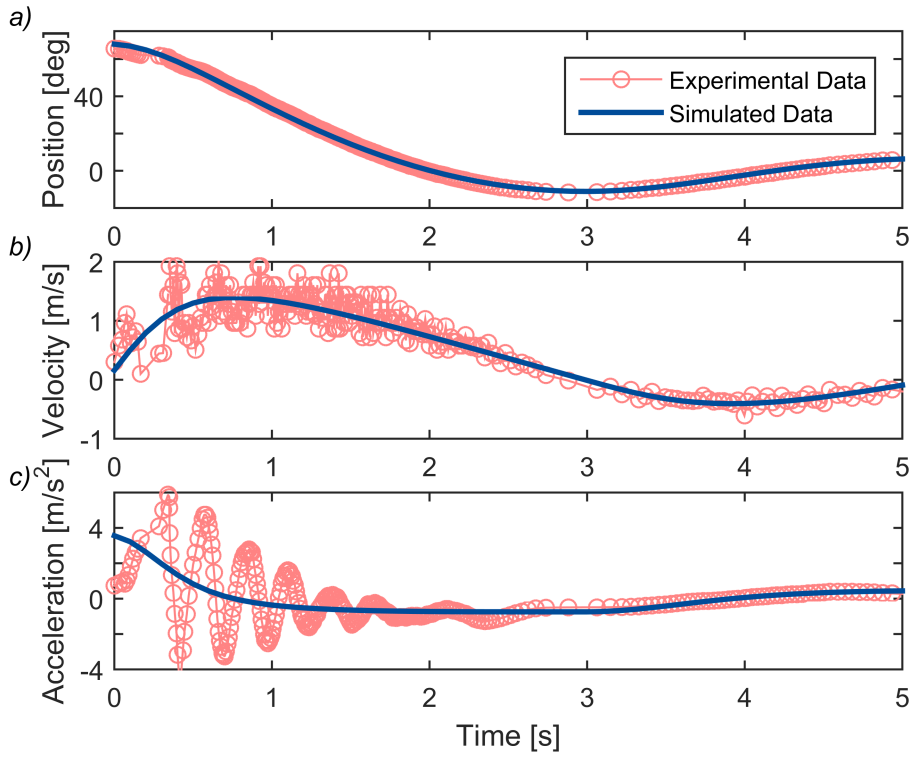

Figure 5.12: Comparison plot of pendulum simulation and experimental data on the surge axis with (a) position, (b) velocity, and (c) acceleration

5.2.3.1 Hydrodynamic model verification

A comparison of a dynamic simulation of free-decay pendulum motion versus the experimental data for the vehicle without the umbilical on the surge axis is shown in Figure 5.12. The experimental position and velocity are unfiltered (1000 count optical encoder resolution), but the acceleration data is smoothed with a 10 point center-averaging filter to reduce the effect of noise on the differentiation. The update rate in the dynamic simulation is at least 0.01 s. High frequency oscillations visible in the experimental acceleration are likely due to off-axis motion of the pendulum during the experiment [*Joslin et al.*]. Although the simulated data does not contain this motion, nor would it be expected due to simulation constraints, it tracks the mean trajectory well, with a root-mean-square (RMS) position error

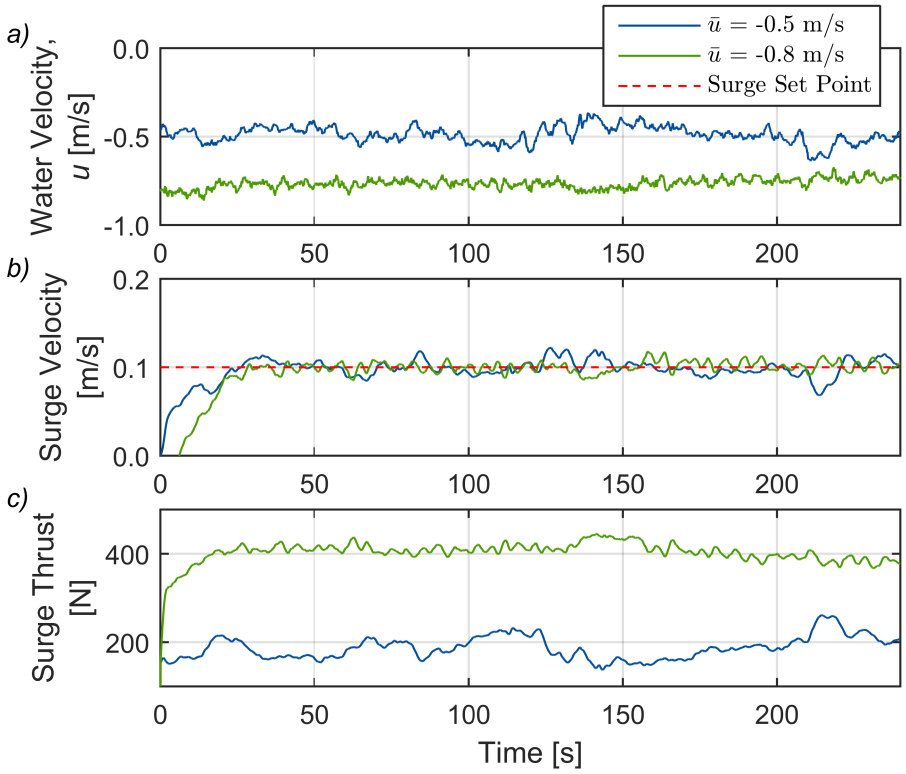

Figure 5.13: Representative surge controller simulation data, including acceleration from rest, with (a) the water velocity acting on the face of the vehicle, (b) the surge velocity of the system, and (c) the surge controller thrust force

of 1.1°. Similar comparisons for the sway and heave axes result in RMS errors of 1.1° and 1.2°, respectively.

5.2.3.2 Baseline results

For simulations with the vehicle and umbilical, the yaw, surge, and depth controllers can maintain the commanded heading, forward motion, and depth in turbulent currents with a mean velocity of up to 1.0 m/s. Beyond this point, both the horizontal and vertical thrust capacities are insufficient to maintain headway or depth respectively. Figure 5.13 shows a representative surge controller time series for 0.5 m/s and 0.8 m/s mean current simulations.

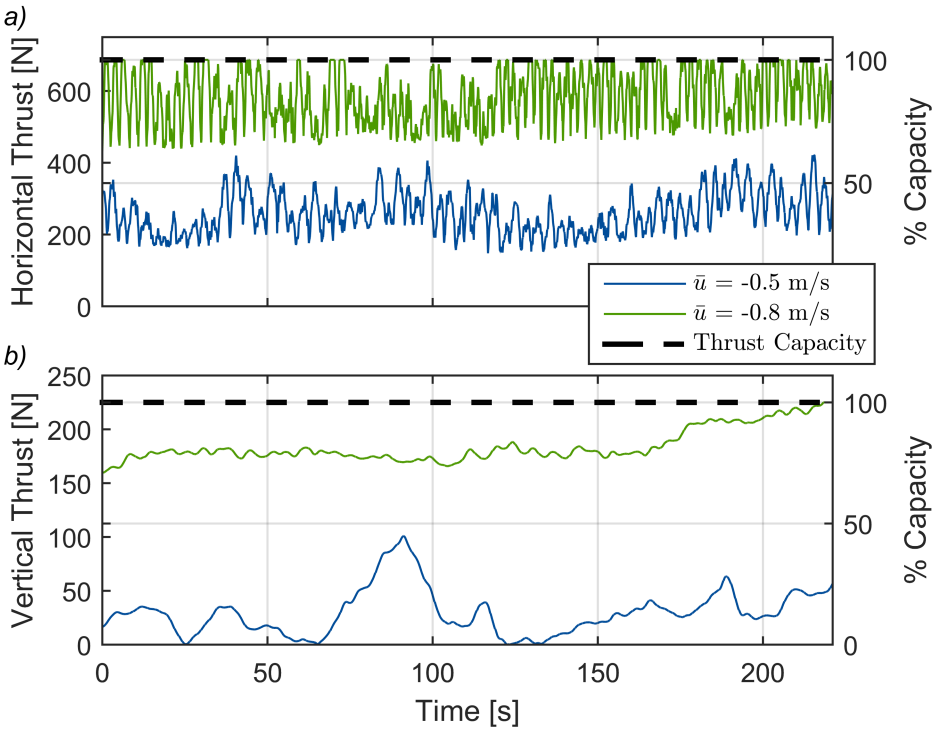

Figure 5.14: Representative simulation control thrust for the (a) combined surge and yaw thrusters and (b) vertical thrusters. Higher vertical thrust for elevated mean velocity associated with vehicle pitch response

For the 0.5 m/s case, the controllers reject the turbulent current disturbances and maintain the desired set points to within ± 1.5° in yaw orientation, ± 0.03 m/s in surge velocity, and ± 0.4 m in heave position. For the 0.8 m/s case, these same ranges are ± 1.5° in yaw, ± 0.02 m/s in surge, and ± 0.5 m in heave. The total horizontal and vertical thruster forces are shown in Figure 5.14 for the same mean current simulation along with the associated thrust capacity. While the 0.5 m/s mean current simulation remains within the thruster capacity, the 0.8 m/s simulation reaches the capacity at several points in the simulation.

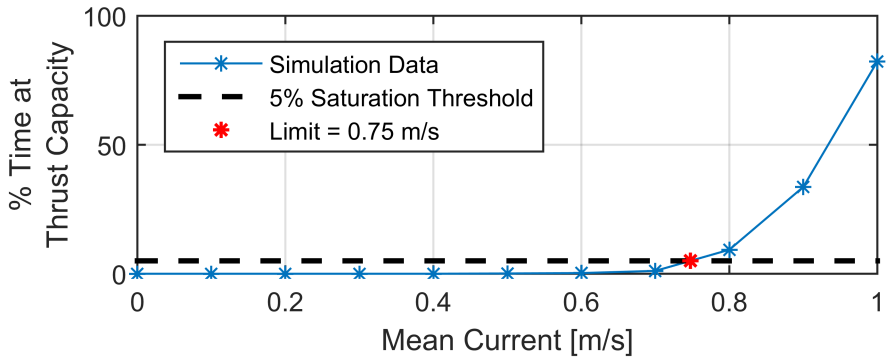

Figure 5.15: Predicted operational limit by percent time operating at thrust capacity

5.2.3.3 Predicted operational limits and stability analysis

The predicted, conservative operational limit (exceeding maximum thrust capacity for more than 5% of simulation time) in turbulent currents is 0.74 m/s. At this limit, the horizontal and vertical thrusters are operating, on average, at 74% and 67% of their respective capacities. Of the required horizontal thrust, 81% is dedicated to surge and 19% is dedicated to yaw control. This same operational limit is predicted when the umbilical is replaced by a constant tensile force acting on the ROV. If the umbilical is neglected, the predicted operating limit is 0.75 m/s and the horizontal and vertical thrust force require, on average, 71% and 73% of their respective capacities, with the horizontal thrust divided between surge and yaw by 79% and 21%. As summarized in Table 5.11, the difference between simulations with and without the umbilical is minimal. While the umbilical adds a small amount of drag to the system, the connection point on the back of the ROV increases passive stability to the pitch, roll, and yaw, thereby slightly reducing the associated yaw control force.

For the ten simulations performed without the umbilical at each mean current, the percentage of time the horizontal thrusters are operating at capacity is shown in Figure 5.15. The 5% saturation threshold is illustrated in this figure to demonstrate how the operational limit is determined. Although this represents an arbitrary limit, the rapid rise in percent time operating at capacity beyond this point indicates that the results are relatively robust.

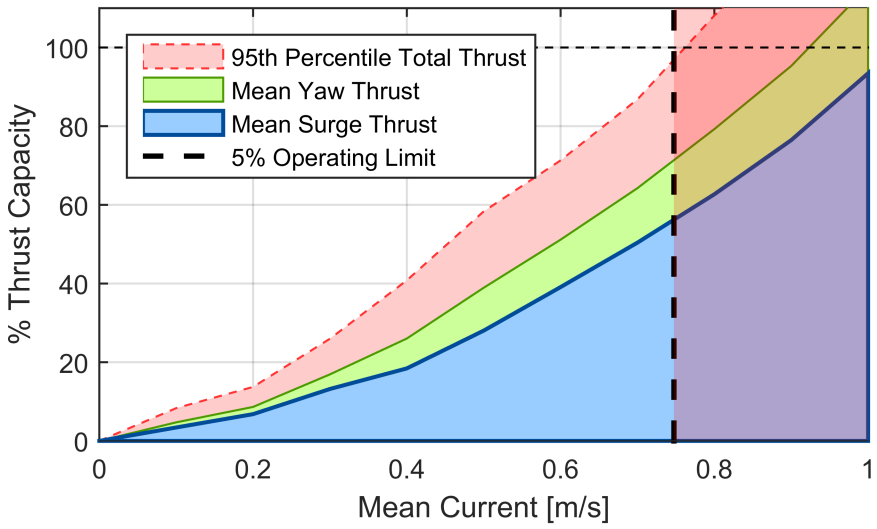

Figure 5.16: Mean and 95^{th} percentile of horizontal thrust capacity to maintain heading and headway

Figure 5.16 shows the division of the horizontal thrust capacity between the yaw and surge controllers along with the 95^{th} percentile of the combined thrust. Although the vehicle is able to maintain maneuverability in mean currents up to 1.0 m/s, the 5% saturation point represents a conservative limit, beyond which, a pilot would need to repeatedly reduce forward motion to less than 0.1 m/s, perhaps even losing ground, to make thrust available to maintain heading or depth.

Passive stability on the pitch and roll axes are shown in Figure 5.17 with the mean and 95^{th} percentile deviations for the ten sets of simulations without the umbilical. The negative mean pitch angle with increasing mean current is caused by the center of thrust being positioned above the center of pressure on the body. As more forward thrust is required to make headway, the vehicle pitches forward and the vertical thrusters compensate to maintain the desired depth. At the predicted operating limit, the system is pitched forward by $\sim 3.3°$. This pitch angle could be decreased by modifying the vehicle design to increase the buoyant righting moment or decrease the separation between the center of pressure and center of

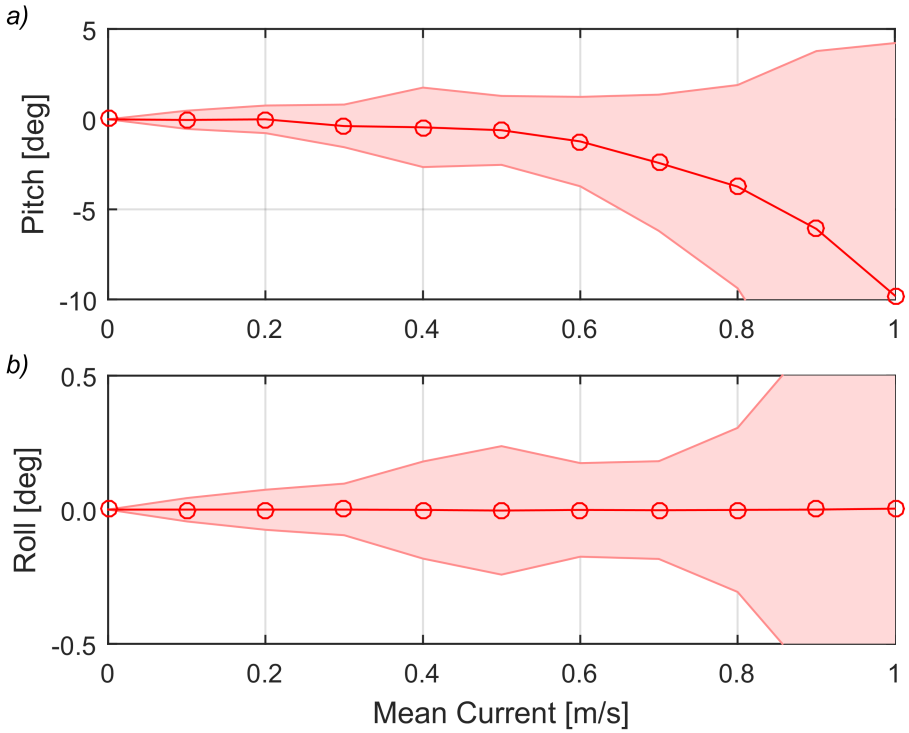

Figure 5.17: Passive stability with mean value (solid line) and 95^{th} percentile (shaded area) on the (a) pitch and (b) roll axes

thrust.

5.2.3.4 Parameter sensitivity studies

Table 5.11 lists the sensitivity study parameters with the resulting change in predicted operational limit and the percent difference from a baseline case that excludes the umbilical. Given the limited differences between the vehicle with and without the umbilical, sensitivity studies include only the vehicle to reduce computational cost. The percentage change of the horizontal thrust capacity dedicated to yaw and surge at the predicted operational limit are also tabulated to demonstrate the types of changes to system performance.

In uniform currents, the predicted operating limit is 1.01 m/s, which is an over-prediction

Table 5.11: Parameter sensitivity study results summary (baseline values in parentheses)

Study Variable	**Value**	**Change in Operational Limit**	**% Difference Operational Limit**	**Yaw Thrust**	**Surge Thrust**
Baseline Variables	NA	0.75	NA	NA	NA
With Umbilical Model	NA	-0.01	-1.3%	-11.7%	3.2%
Umbilical Tension [N](0)	20 N	-0.01	-1.3%	-6.5%	1.8%
Input Current (Turbulent)	Uniform Current	+0.26	34.7%	-100%	27.2%
Mesh Resolution [# of Polygons](7243)	Halved (3784)	0	0%	-1.4%	0.4%
	Doubled (18622)	0	0%	0.5%	-0.1%
Controller Update Rate [s](0.1)	0.001	+0.05	6.7%	-1.9%	0.5%
	0.01	0	0%	1.9%	-0.5%
Turbulence Filtering [Length scale, m](1.5)	No Filtering	-0.02	-2.7%	9.8%	-2.7%
	0.5 m	0	0%	3.3%	-0.9%
Hydrodynamic Coefficients [C_d and C_a](C_d and C_a = measured)	C_d = measured C_a = canonical	+0.14	18.7%	-39.7%	11.7%
	C_d = CFD C_a = canonical	+0.19	25.3%	-33.2%	9.0%
	C_d = CFD C_a = measured	+0.07	9.3%	16.8%	-4.6%
	C_d = canonical C_a = measured	-0.01	-1.3%	-7.9%	2.2%
	C_d = canonical C_a = canonical	+0.08	10.7%	-37.4%	10.2%

of 35% (+0.26 m/s). Without turbulence, the yaw control force is negligible and the surge control force is constant. This demonstrates that the turbulence effects are non-negligible in these environments, both in terms of the direct resistance to motion and thruster needs to maintain heading.

Operational limits are insensitive to mesh resolution and turbulence filtering length scale (i.e., less than 0.02 m/s change). A faster controller update rate does increase the operating limit, but requires rapid thruster action, which would be difficult to achieve with a human in the loop and may not be physically realizable due to thruster response time. The operational limit is, however, sensitive to the selection of the hydrodynamic coefficients. For example, in a simulation with CFD-derived drag coefficients and canonical estimates for added mass coefficients, the operating limit increases by 25%. This performance over-prediction is caused by the reduction in system inertial and drag forces. While the operational limit is relatively well-predicted with canonical values for drag and added mass, this appears to be coincidental, as the allocation of thrust to yaw and surge is inaccurate. Predicted limits with the measured added mass coefficients are much closer to the baseline case when paired with either canonical or CFD-derived drag coefficients. This suggests the added mass contributes predominantly to the hydrodynamic forces that must be overcome to maintain stability and maneuverability during deployments in turbulent currents and is worth the effort to quantify for specific vehicle geometries.

5.2.4 Conclusion

This analysis suggests that a relatively low-cost inspection class ROV is capable of deploying instrumentation packages at marine energy sites subject to turbulent currents. With a conservative threshold for allowable time at peak thrust capacity, an operating limit of 0.74 m/s is predicted. Passive stability from the buoyant righting moment results in minimal pitch and roll. Operational limits are significantly over-predicted if turbulent motions are neglected. Similarly, the sensitivity of the predicted operating limit to the prescribed hydrodynamic coefficients illustrates the importance of accurately defining these parameters.

While dynamic simulations have inherent limitations, they are computationally efficient for investigating broad parameter spaces for underwater vehicle designs.

Chapter 6

CONCLUSIONS

Cost-effective environmental monitoring of marine renewable energy projects is imperative to ensuring sustainable development. Industry developers, government regulators, and the general public alike stand to gain crucial information from the monitoring of early technology demonstration projects. The highly energetic conditions that typify marine energy sites pose a unique set of engineering challenges to deploying and maintaining instrumentation to conduct these monitoring missions. Strong tidal currents and ocean wave action generally preclude standard oceanographic monitoring methods. The research presented in this thesis supports the development of an innovative system addressing these challenges.

6.1 Instrumentation Sub-Systems

To determine the size and layout of the AMP, the instrumentation constraints are investigated, starting with the stereo-optical camera system. This system is capable of characterizing high velocity targets in the absence of ambient light with millimeter precision at up to several meter range. System capabilities to image, measure, and track targets are demonstrated both in a laboratory setting and in the field. Optimization of the stereographic layout increases the potential to obtain complete target information within a known range by maximizing the overlapping camera fields of view. While this system has been developed specifically for monitoring marine energy converters, the design and optimization methods apply generally to optimization and use of underwater optical systems.

Biofouling of camera optical ports deployed in marine environments generally leads to frequent maintenance to preserve image quality. While the mitigation methods employed on the optical camera system (copper rings and mechanical wipers) are not novel, documented

field evaluations using quantitative methods do not exist in the literature. The methods developed to quantitatively monitor fouling on the camera optical ports in real time through internal LED lighting apply to any underwater optical camera system and can predict the need for maintenance prior to image degradation. The four month field endurance test of the prototype camera system demonstrates the effectiveness of these mitigation methods to enable long term deployments.

Stereo-optical imagery in the near-field of marine energy converters enables detailed observations of marine animal interactions. This will facilitate species identification - a critical requirement for deployments in waters with a known presence of protected or endangered marine animals [*Polagye et al.*, 2014]. Stereographic information about fish size, combined with the optical images, will improve fisheries scientist's ability to distinguish between species. Target tracking of marine animals around tidal turbines will also allow for the distinction to be made between collisions and near misses with greater accuracy than active acoustic monitoring. By integrating the optical camera system with other, lower-bandwidth instruments on the AMP, targeted monitoring with instrument triggers will reduce behavioral effects due to strobe lighting.

While optical imagery is valuable, it also comes at a high cost for data storage and processing. Without appropriately targeted studies, camera triggering methods, and automated image processing, optical cameras will rapidly produce "data mortgages" [*Polagye et al.*, 2014]. For example, this stereo-optical camera system collecting images at 10 frames per second for a three month deployment would generate over 600 terabytes of uncompressed imagery. For this reason, along with the desire to minimize behavioral changes associated with artificial lighting, future work with the camera system will integrate it with other instrument triggers on the AMP.

6.2 Adaptable Monitoring Package and Millennium Falcon

The Adaptable Monitoring Package and Millennium Falcon deployment vehicle provide the benefits of a cabled instrumentation platform while maintaining the flexibility of an au-

tonomous system. High power and data bandwidth from a shore connection allow the use of instruments that would be otherwise impractical for environmental monitoring. The adaptable design of the AMP mechanical framework and electrical architecture allows the instruments incorporated into the system to evolve and be customized for specific monitoring missions. Designing the AMP to be deployed by an inspection-class ROV decreases mobilization time and cost for maintenance operations. Monitoring of marine energy converters with the AMP promises to generate valuable data to fill knowledge gaps around the risks of environmental impacts.

Hydrodynamic modeling of the AMP and deployment vehicle provides predictive capability for operational limits and vehicle dynamics. Operational conditions are evaluated for a tidal current site (Admiralty Inlet) and wave energy site (PMEC-NETS). Moderate-resolution CFD simulations are shown to predict hydrodynamic drag coefficients with acceptable accuracy (within 20% of experimental results). These simulations can inform design decisions at an early stage of system development. Experimental validation using free-decay pendulum experiments in a pool provide an economic alternative to the use of large testing facilities and can provide information about added mass for relatively complex bodies. These methods are generally applicable to the broader field of marine robotics. The continued growth of the marine renewable energy industry will likely rely heavily on the use of underwater vehicles which will require pushing the limits of vehicle operational capabilities.

Dynamic simulations provide insight into system performance without the costs or risks associated with field trials. For this system, the simulations can predict the stability and maneuverability limits in turbulent currents without risking damage by testing the vehicle to the point of instability. While simulation results should generally be verified through experiments, the risk associated with this type of testing can be prohibitive. The measured hydrodynamic coefficients result in higher accuracy simulations than the use canonical or computationally-derived values. Similarly, the use of tidal turbulence data from the mooring deployment in Admiralty Inlet ensures that the current forcing is representative of a potential tidal energy site. The simulation results suggest the ROV will be capable of maintaining

maneuverability for deployments in turbulent currents up to 0.7 m/s and that this limit is strongly related to turbulence. Continued development of marine energy industries will benefit from lower cost ROVs with extended capabilities for operations in turbulent currents, informed by dynamic simulations.

6.3 Future Work

The environmental monitoring potential of the AMP stands to be greatly expanded through instrument integration. Instrument operation and data collected during endurance testing will be used to develop novel integration methods and data processing algorithms. To reduce the potential for data mortgages, it may be possible to use instruments with a larger range and lower data bandwidth (e.g., the passive acoustics system) to trigger higher bandwidth instruments that provide more monitoring information (e.g., the optical camera system). In addition, automated target tracking algorithms may allow data to be processed in real time. Incorporating these capabilities into the AMP will ultimately improve environmental monitoring of marine energy converters and reduce the associated costs of technology development.

Initial field testing of the AMP and Millennium Falcon deployment ROV will be the true validation of the system. In February, 2015, AMP deployment and recovery operations were successfully conducted from the R/V Jack Robertson in the calm waters of Shilshole Bay Marina, Puget Sound, WA. In June 2015, the next stage of field trials will take place near Marrowstone Island, Admiralty Inlet, with moderate tidal currents. Over the following summer, the AMP will be deployed in Sequim Bay where it will be cabled to a shore facility for real time operation during an endurance trial. This trial will provide the opportunity to conduct the instrument integration investigation described above. Results from these field tests will inform future system design modifications to continue expanding the AMP's potential to contribute to a sustainable marine energy future.

BIBLIOGRAPHY

Standard practice for evaluating biofouling resistance and physical performance of marine coating systems - D6990-05(2011), *Tech. rep.*, ASTM International, West Conshohocken, PA, USA, doi:10.1520/D6990-05.2, 2011.

ANSYS Fluent 14.0 user's guide, vol. 14.0, 1–2498 pp., ANSYS, Inc., Canonsburg, PA, 2011.

Monthly energy review, 40th Anniversary Issue, *Tech. rep.*, US Energy Information Administration, 2014.

ProteusDS 2015 Manual, 2.15.2511 ed., Dynamic Systems Analysis Ltd., Victoria, BC, Canada, 2015.

Alessandri, A., R. Bono, M. Caccia, G. Indiveri, and G. Veruggio, Experiences on the modelling and identification of the heave motion of an open-frame UUV, in *MTS/IEEE Ocean. '98*, 2, pp. 1049–1053, Nice, France, doi:10.1109/OCEANS.1998.724396, 1998.

Alvertos, N., D. Brzakovic, and R. Gonzalez, Camera geometries for image matching in 3-D machine vision, *IEEE Trans. Pattern Anal. Mach. Intell.*, *11*(9), 897–915, doi:10.1109/34.35494, 1989.

Amaral, S., N. Perkins, D. Giza, and B. McMahon, Evaluation of fish injury and mortality associated with hydrokinetic turbines, *Tech. rep.*, Electric Power Research Institute, Palo Alto, CA, 2011.

Antonelli, G., *Underwater robots*, Springer, Berlin, 2003.

Ashton, I., J. Van-Nieuwkoop-McCall, H. Smith, and L. Johanning, Spatial variability of

waves within a marine energy site using in-situ measurements and a high resolution spectral wave model, *Energy*, *66*, 699–710, doi:10.1016/j.energy.2013.12.065, 2014.

Aylsworth, W. L., H. J. Postley, B. B. Sandrew, B. E. Dobrin, and W. Husak, Stereographic digital cinema: Production and exhibition techniques in 2012, *Proc. IEEE*, *101*(1), 169–189, doi:10.1109/JPROC.2012.2191610, 2013.

Baptista, A., B. Howe, J. Freire, D. Maier, and C. T. Silva, Scientific exploration in the era of ocean observatories, *IEEE Comput. Sci. Eng.*, *9*, 85–85, doi:10.1109/MCSE.2008.83, 2008.

Barnard, S. T., and M. a. Fischler, Computational stereo, *ACM Comput. Surv.*, *14*(4), 553–572, doi:10.1145/356893.356896, 1982.

Barnes, C. R., M. M. R. Best, B. D. Bornhold, S. K. Juniper, B. Pirenne, and P. Phibbs, The NEPTUNE Project - A cabled ocean observatory in the NE Pacific: Overview, challenges and scientific objectives for the installation and operation of Stage I in Canadian waters, *Int. Symp. Underw. Technol. UT 2007*, pp. 308–313, doi:10.1109/UT.2007.370809, 2007.

Barnes, C. R., M. M. R. Best, F. R. Johnson, L. Pautet, and B. Pirenne, Challenges, benefits, and opportunities in installing and operating cabled ocean observatories: Perspectives from NEPTUNE Canada, in *IEEE Symp. Underw. Technol. UT 2011*, pp. 1–7, IEEE, Tokyo, Japan, doi:10.1109/JOE.2012.2212751, 2011.

Barr, S., Short term behavioral responses in fish species to the open-centre turbine, *Tech. rep.*, Open Hydro unpublished memorandum, 2010.

Barrios, L., and A. Rodríguez, Behavioural and environmental correlates of soaring-bird mortality an an-shore wind turbines., *J. Appl. Ecol.*, *41*, 72–81, doi:10.1111/j.1365-2664.2004.00876.x, 2004.

Beer, A., Determination of the absorption of red light in colored liquids, *Ann. Phys. Chem.*, *86*, 78–88, 1852.

Beer, F. P., and E. R. Johnston, *Vector Mechanics for Engineers: Statics and Dynamics*, Mcgraw-Hill, 2004.

Belanger, P., P. Dobrovolny, A. Helmy, and X. Zhang, Estimation of angular velocity and acceleration from shaft-encoder measurements, *Int. J. Rob. Res.*, *17*, 1225–1233, doi: 10.1177/027836499801701107, 1998.

Blevins, R. D., *Formulas for natural frequency and mode shape*, Robert E. Krieger Publishing Company, 1979.

Boehlert, G. W., and A. B. Gill, Environmental and ecological effects of ocean renewable energy development: a current synthesis, *Oceanography*, *23*(2), 68–81, 2010.

Boehlert, G. W., G. R. McMurray, and C. E. Tortorici, Ecological effects of wave energy development in the Pacific Northwest, *Tech. rep.*, U.S. Department of Commerce, National Oceanic and Atmospheric Administration, National Marine Fisheries Service, NOAA Technical Memorandum NMFS-F/SPO-92, 2008.

Bouguet, J. Y., Camera calibration toolbox for Matlab, 2010.

Bowen, A. D., D. R. Yoerger, L. L. Whitcomb, and D. J. Fornari, Exploring the Deepest Depths : Preliminary Design of a Novel Light-Tethered Hybrid ROV for Global Science in Extreme Environments, *Mar. Technol. Soc. J.*, *38*(2), 92–101, doi: 10.4031/002533204787522776, 2004.

Breton, S. P., and G. Moe, Status, plans and technologies for offshore wind turbines in Europe and North America, *Renew. Energy*, *34*(3), 646–654, doi:10.1016/j.renene.2008.05.040, 2009.

Bridger, C., and R. Booth, The effects of biotelemetry transmitter presence and attachment procedures on fish physiology and behavior, *Rev. Fish. Sci.*, *11*(1), 13–34, doi: 10.1080/16226510390856510, 2003.

Brown, R. H., S. C. Schneider, and M. G. Mulligan, Analysis of algorithms for velocity estimation from discrete position versus time data, *IEEE Trans. Ind. Electron.*, *39*(1), 11–19, doi:10.1109/41.121906, 1992.

Cada, G., J. Ahlgrimm, M. Bahleda, T. Bigford, S. Damiani Stavrakas, D. Hall, R. Moursund, and M. Sale, Potential impacts of hydrokinetic and wave energy conversion technologies on aquatic environments, *Fisheries*, *32*(4), 174–181, 2007.

Chave, a. D., et al., Cyberinfrastructure for the US ocean observatories initiative: Enabling interactive observation in the ocean, in *Ocean. '09 IEEE Bremen Balanc. Technol. with Futur. Needs*, pp. 1–10, MTS-IEEE, doi:10.1109/OCEANSE.2009.5278134, 2009.

Christ, R. D., and R. L. Wernli, *The ROV manual: a user's guide to remotely operated vehicles*, Butterworth-Heinemann, 2013.

Conrado de Souza, E., and N. Maruyama, Intelligent UUVs: Some issues on ROV dynamic positioning, *IEEE Trans. Aerosp. Electron. Syst.*, *43*(1), 214–226, doi:10.1109/TAES.2007.357128, 2007.

Cornelius, T., D. Black, D. Harris, A. Crossley, B. Brewerton, A. Beagley, S. Blott, and J. Styles, 51 million Meygen financial close completed, *Tech. rep.*, Atlantis Resources Limited, 2014.

Coutant, C. C., and R. R. Whitney, Fish behavior in relation to passage through hydropower turbines: a review, *Transactions*, *129*(April 2015), 37–41, doi:10.1577/1548-8659(2000)129, 2000.

Cowles, T., J. Delaney, J. Orcutt, and R. Weller, The oceans observatories initiative: sustained ocean observing across a range of spatial scales, *Mar. Technol. Soc. J.*, *44*(6), 54–64, 2010.

Daborn, G., L. Isaacman, A. Redden, S. Macdougall, M. Swanburg, R. Karsten, and J. Colton, Best practice in MRE risk assessment : experience from the Bay of Fundy, in

2nd Int. Conf. Environ. Interact. Mar. Renew. Energy Technol., May, pp. 1–3, Stornoway, Isle of Lewis, Outer Hebrides, Scotland, 2014.

Dadswell, M. J., and R. a. Rulifson, Macrotidal estuaries: a region of collision between migratory marine animals and tidal power development, *Biol. J. Linn. Soc.*, *51*, 93–113, doi:10.1111/j.1095-8312.1994.tb00947.x, 1994.

Debiemme-Chouvy, C., Y. Hua, F. Hui, J.-L. Duval, and H. Cachet, Electrochemical treatments using tin oxide anode to prevent biofouling, *Electrochim. Acta*, *56*(28), 10,364–10,370, doi:10.1016/j.electacta.2011.03.025, 2011.

Delauney, L., C. Compère, and M. Lehaitre, Biofouling protection for marine environmental sensors, *Ocean Sci.*, *6*(2), 503–511, doi:10.5194/os-6-503-2010, 2010.

Dickey, T., and G. Chang, Recent advances and future visions: Temporal variability of optical and bio-optical properties of the ocean, *Oceanography*, *14*(3), 15–29, doi:10.5670/oceanog.2001.21, 2001.

Dobretsov, S., D. N. Williams, and J. Thomason, *Biofouling methods*, John Wiley & Sons, Ltd., Oxford, UK, doi:10.1002/9781118336144, 2014.

Dropkin, A. M., S. a. Huyer, and C. Henoch, Combined experimental/numerical development of propulsor evaluation capability, *J. Fluids Eng.*, *133*(8), 081,105, doi:10.1115/1.4004387, 2011.

Egeskov, P., A. Bjerrum, A. Pascoal, C. Silvestre, C. Aage, and L. W. Smitt, Design, construction and hydrodynamic testing of the AUV Marius, in *IEEE Symp. Auton. Underw. Veh.*, doi:10.1109/AUV.1994.518626, 1994.

Elvander, J., and G. Hawkes, ROVs and AUVs in support of marine renewable technologies, in *MTS/IEEE Ocean. '12*, pp. 1–6, IEEE, Hampton Roads, VA, doi:10.1109/OCEANS.2012.6405139, 2012.

EMEC, EMEC and ETI begin environmental monitoring survey, 2013.

Eng, Y.-h., W. Lau, E. Low, G. Seet, and C. Chin, Estimation of the hydrodynamics coefficients of an ROV using free decay pendulum motion, *Eng. Lett.*, *16*(3), 326, 2008.

Eng, Y.-h., M.-w. Lau, and C.-s. Chin, Added mass computation for control of an open-frame remotely-operated vehicle: Application using WAMIT and Matlab, *J. Mar. Sci. Technol.*, doi:10.6119/JMST-013-0313-2, 2013.

Evans, J., and M. Nahon, Dynamics modeling and performance evaluation of an autonomous underwater vehicle, *Ocean Eng.*, *31*, 1835–1858, doi:10.1016/j.oceaneng.2004.02.006, 2004.

Failla, G., and F. Arena, New perspectives in offshore wind energy, *Philos. Trans. R. Soc. A*, *373*, doi:10.1098/rsta.2014.028, 2015.

Fletcher, B., A. Bowen, D. R. Yoerger, and L. L. Whitcomb, Journey to the Challenger Deep: 50 years later with the Nereus hybrid remotely operated vehicle, *Mar. Technol. Soc. J.*, *43*(5), 65–76, doi:10.4031/MTSJ.43.5.26, 2009.

Furey, N. B., M. a. Dance, and J. R. Rooker, Fine-scale movements and habitat use of juvenile southern flounder Paralichthys Lethostigma in an estuarine seascape, *J. Fish Biol.*, *82*, 1469–1483, doi:10.1111/jfb.12074, 2013.

Gallager, S. M., H. Singh, S. Tiwari, J. Howland, P. Rago, and W. Overholtz, Report of the National Marine Fisheries Service Workshop on underwater video analysis, in *Rep. Natl. Mar. Fish. Serv. Work. Underw. Video Anal.*, pp. 50–53, U.S. Dept. of Commerce, NOAA Tech. Memo No. HMFS-F/SPO-68, 2005.

Goltz, J. D., P. J. Oshie, and P. B. Jones, Policy statement regarding processes for determining whether projects are eligible renewable resources, *Tech. rep.*, Washington State Utilities and Transportation Commission, 2011.

Greene, H. G., Habitat characterization of the SnoPUD turbine site-Admiralty Head, Washington State, *Tech. rep.*, Final Report, 2011.

Harding, S., J. Thomson, B. Polagye, M. Richmond, V. Durgesh, and I. Bryden, Extreme value analysis of tidal stream velocity perturbations, in *Eur. Wave Tidal Energy Conf.*, p. 7, Southampton, United Kingdom, 2011.

Harris, C., and M. Stephens, A combined corner and edge detector, in *Procedings Alvey Vis. Conf. 1988*, pp. 147–151, The Plessey Company, Roke Manor, UK, doi:10.5244/C.2.23, 1988.

Harvey, E. S., M. Cappo, J. J. Butler, N. Hall, and G. a. Kendrick, Bait attraction affects the performance of remote underwater video stations in assessment of demersal fish community structure, *Mar. Ecol. Prog. Ser.*, *350*, 245–254, doi:10.3354/meps07192, 2007.

Henderson, A. R., and D. Witcher, Floating offshore wind energy - a review of the current status and an assessment of the prospects, *Wind Eng.*, *34*(1), 1–16, doi:10.1260/0309-524X.34.1.1, 2010.

Howe, B. M., and T. Mcginnis, Sensor networks for cabled ocean observatories, in *Int. Symp. Underw. Technol.*, pp. 113–120, IEEE, doi:10.1109/UT.2004.1405499, 2004.

Howland, J., S. Gallager, H. Singh, A. Girard, L. Abrams, and C. Griner, Development of a towed survey system for deployment by the fishing industry, in *MTS/IEEE Ocean. 2006*, IEEE, Boston, MA, 2006.

Huang, P. X., J. B. Boom, and R. B. Fisher, Underwater live fish recognition using a balance-guaranteed optimized tree, in *Comput. Vision-ACCV*, pp. 422–433, Springer, Berlin, 2012.

Inger, R., et al., Marine renewable energy: Potential benefits to biodiversity? An urgent call for research, *J. Appl. Ecol.*, *46*, 1145–1153, doi:10.1111/j.1365-2664.2009.01697.x, 2009.

Jaffe, J. S., Underwater optical imaging: the design of optical systems, *Oceanography*, *1*(2), 40–41, doi:http://dx.doi.org/10.5670/oceanog., 1988.

Jaffe, J. S., Multi autonomous underwater vehicle optical imaging for extended performance, in *MTS/IEEE Ocean. 2007*, 2007.

Jagadeesh, P., K. Murali, and V. Idichandy, Experimental investigation of hydrodynamic force coefficients over AUV hull form, *Ocean Eng.*, *36*(1), 113–118, doi:10.1016/j.oceaneng.2008.11.008, 2009.

Jakuba, M. V., D. R. Yoerger, and L. L. Whitcomb, Longitudinal control design and performance evaluation for the Nereus 11,000 m underwater vehicle, in *MTS-IEEE Ocean. 2007*, vol. 351, IEEE, Vancouver, BC, Canada, doi:10.1109/OCEANS.2007.4449305, 2007.

Johnson, R. L., et al., Chief Joseph Kokanee enhancement project; strobe light deterrent efficacy test and fish behavior determination at Grand Coulee Dam third powerplant forebay, *Tech. Rep. January*, Bonneville Power Administration, US Deparment of Energy, Contract DE-AC06-76RL01830, 2003.

Jones, G. a., Constraint, optimization, and hierarchy: reviewing stereoscopic correspondence of complex features, *Comput. Visoin Image Underst.*, *65*(1), 57–78, doi:10.1006/cviu.1996.0482, 1997.

Jonkman, B., TurbSim User's Guide : Version 1.50, *Tech. rep.*, National Renewable Energy Laboratory, Golden, CO, USA, 2009.

Joslin, J., and B. Polagye, Demonstration of biofouling mitigation methods for long-term deployments of optical cameras, *Mar. Technol. Soc. J.*, *49*(1), 88–96, 2015.

Joslin, J., B. Polagye, and A. Stewart, Hydrodynamic coefficient determination for an open-framed underwater vehicle, *Ocean Eng.*

Joslin, J., E. Celkis, C. Roper, A. Stewart, and B. Polagye, Development of an adaptable monitoring package for marine renewable energy, in *MTS/IEEE Ocean. '2013*, MTS-IEEE, San Diego, CA, 2013.

Joslin, J., B. Polagye, and S. Parker-Stetter, Development of a stereo-optical camera system for monitoring tidal turbines, *SPIE J. Appl. Remote Sens.*, *8*(1), 083,633–1–25, doi: 10.1117/1.JRS.8.083633, 2014a.

Joslin, J., B. Polagye, and A. Stewart, Development of an adaptable monitoring package for marine renewable energy, in *5th Int. Conf. Ocean Energy*, Halifax, NS, Canada, 2014b.

Joslin, J., B. Rush, A. Stewart, and B. Polagye, Development of an adaptable monitoring package for marine renewable energy projects part II : hydrodynamic performance, in *2nd Mar. Energy Technol. Symp. Glob. Mar. Renew. Energy Conf.*, Seattle, WA, 2014c.

Juang, P.-N., *Applied system identification*, Prentice Hall PTR, 1994.

Kawase, M., P. Beba, B. C. Fabien, B. Batten, and B. Langley, Finding an optimal placement depth for a tidal in-stream energy conversion device in an energetic , baroclinic tidal channel, *Tech. Rep. Report #7*, Northwest National Marine Renewable Energy Center, Seattle, WA, USA, 2011.

Kelley, N. D., *Turbulence-turbine interaction : the basis for the development of the TurbSim stochastic simulator*, nrel/tp-50 ed., National Renewable Energy Laboratory, Golden, CO, USA, 2011.

Khan, M. J., G. Bhuyan, M. T. Iqbal, and J. E. Quaicoe, Hydrokinetic energy conversion systems and assessment of horizontal and vertical axis turbines for river and tidal applications: A technology status review, *Appl. Energy*, *86*(10), 1823–1835, doi: 10.1016/j.apenergy.2009.02.017, 2009.

Lamb, H., *Hydrodynamics*, Cambridge University Press, 1932.

Lehaitre, M., and C. Compere, Biofouling and underwater measurements, in *Real-Time Obs. Syst. Ecosyst. Dyn. Harmful Algal Bloom.*, 2005.

Loebis, D., R. Sutton, J. Chudley, and W. Naeem, Adaptive tuning of a Kalman filter via fuzzy logic for an intelligent AUV navigation system, *Control Eng. Pract.*, *12*, 1531–1539, doi:10.1016/j.conengprac.2003.11.008, 2004.

Long, J., B. Wu, J. Wu, T. Xiao, and L. Wang, Estimation of added mass and drag coefficient for a small remotely operated vehicle, in *2008 Int. Conf. Inf. Autom.*, 2, pp. 337–342, Ieee, doi:10.1109/ICINFA.2008.4608021, 2008.

López, I., J. Andreu, S. Ceballos, I. n. Martínez De Alegría, and I. n. Kortabarria, Review of wave energy technologies and the necessary power-equipment, *Renew. Sustain. Energy Rev.*, *27*, 413–434, doi:10.1016/j.rser.2013.07.009, 2013.

Manov, D., G. Chang, and T. Dickley, Methods for reducing biofouling of moored optical sensors, *J. Atmos. Ocean. Technol.*, *21*, 958–968, 2004.

Marchesan, M., M. Spoto, L. Verginella, and E. a. Ferrero, Behavioural effects of artificial light on fish species of commercial interest, *Fish. Res.*, *73*, 171–185, doi:10.1016/j.fishres.2004.12.009, 2005.

Matai, J., R. Kastner, G. C. Jr, and D. Demer, Automated techniques for detection and recognition of fishes using computer vision algorithms, *Tech. rep.*, NOAA Technical Memorandum NMFS-F/SPO-121, Seattle, WA, 2010.

McCaffrey, K., B. Fox-Kemper, P. E. Hamlington, and J. Thomson, Characterization of turbulence anisotropy, coherence, and intermittency at a prospective tidal energy site: observational data analysis, *Renew. Energy*, *76*, 441–453, doi:10.1016/j.renene.2014.11.063, 2015.

McMichael, G. a., et al., The juvenile salmon acoustic telemetry system: a new tool, *Fisheries*, *35*(April 2015), 9–22, doi:10.1577/1548-8446-35.1.9, 2010.

McMillan, S., D. Orin, and R. McGhee, Efficient dynamic simulation of an underwater vehicle with a robotic manipulator, *IEEE Trans. Syst. Man. Cybern.*, *25*(8), 1194 – 1206, doi:10.1109/21.398681, 1995.

Morison, J., J. Johnson, and S. Schaaf, The force exerted by surface waves on piles, *J. Pet. Technol.*, *2*(5), doi:10.2118/950149-G, 1950.

Morrison, A. T. I., and D. R. Yoerger, Determination of the hydrodynamic parameters of an underwater vehicle during small scale, nonuniform, 1-dimensional translation, in *MTS/IEEE Ocean. '93*, pp. 11,277–11,282, IEEE, doi:10.1109/OCEANS.1993.326105, 1993.

Myers, J. J., C. H. Holm, and R. F. McAllister, *Handbook of ocean and underwater engineering*, McGraw-Hill Book Company, 1969.

Nelson, R. A., and M. Olsson, The pendulum - rich physics from a simple system, *Am. J. Phys.*, 1986.

Ng, K. W., W. H. Lam, and K. C. Ng, 2002-2012: 10 years of research progress in horizontal-axis marine current turbines, *Energies*, *6*(3), 1497–1526, doi:10.3390/en6031497, 2013.

Normandeau Associates, An estimation of survival and injury of fish passed through the Hydro Green Energy Hydrokinetic System, and a characterization of fish entrainment potential at the Mississippi Lock and Dam No. 2 Hydroelectric project (P-4306), *Tech. Rep. 21288*, Hastings, MN, 2009.

O'Driscoll, R. L., P. D. Joux, R. Nelson, G. J. Macaulay, A. J. Dunford, P. M. Marriott, C. Stewart, and B. S. Miller, Species identification in seamount fish aggregations using moored underwater video, *ICES J. Mar. Sci.*, *69*(4), 648–659, doi:10.1093/icesjms/fss010, 2012.

Perveen, R., N. Kishor, and S. R. Mohanty, Off-shore wind farm development: present status and challenges, *Renew. Sustain. Energy Rev.*, *29*, 780–792, doi:10.1016/j.rser.2013.08.108, 2014.

Phang, I. Y., N. Aldred, A. S. Clare, and G. J. Vancso, Effective marine antifouling coatings: studying barnacle cyprid adhesion with atomic force microscopy, *Nanos*, *01*, 36–41, 2007.

Polagye, B., and J. Thomson, Tidal energy resource characterization: methodology and field study in Admiralty Inlet, Puget Sound, WA (USA), *Proc. Inst. Mech. Eng. Part A J. Power Energy*, *227*(June 2007), 352–367, doi:10.1177/0957650912470081, 2013.

Polagye, B., M. Kawase, and P. Malte, In-stream tidal energy potential of Puget Sound, Washington, *Proc. Inst. Mech. Eng. Part A J. Power Energy*, *223*(5), 571–587, doi: 10.1243/09576509JPE748, 2009.

Polagye, B., B. V. Cleve, A. Copping, and K. Kirkendall, Environmental effects of tidal energy development, *Tech. rep.*, 2011.

Polagye, B., A. Copping, R. Suryan, J. Brown-Saracino, and C. Smith, Instrumentation for monitoring around marine renewable energy converters : workshop final report, *Tech. Rep. January*, Pacific Notherwest National Laboratory, Seattle, WA, 2014.

Prestero, T., Verification of a six-degree of freedom simulation model for the REMUS autonomous underwater vehicle, Ph.D. thesis, Massachusetts Institute of Technology and Woods Hole Oceanographic Institution, 2001.

PUD, S., Final pilot license application for the Admiralty Inlet pilot tidal project, *Tech. rep.*, FERC Project No. 12690000, 2012.

Rosenkranz, G. E., S. M. Gallager, R. W. Shepard, and M. Blakeslee, Development of a high-speed, megapixel benthic imaging system for coastal fisheries research in Alaska, *Fish. Res.*, *92*(2-3), 340–344, doi:10.1016/j.fishres.2008.03.014, 2008.

Rush, B., J. Joslin, A. Stewart, and B. Polagye, Development of an adaptable monitoring package for marine renewable energy projects part I : conceptual design and operation, in *2nd Mar. Energy Technol. Symp. Glob. Mar. Renew. Energy Conf.*, Seattle, WA, 2014.

Ryer, C. H., Laboratory evidence for behavioural impairment of fish escaping trawls: A review, *ICES J. Mar. Sci.*, *61*(7), 1157–1164, doi:10.1016/j.icesjms.2004.06.004, 2004.

Ryer, C. H., A. W. Stoner, P. J. Iseri, and M. L. Spencer, Effects of simulated underwater vehicle lighting on fish behavior, *Mar. Ecol. Prog. Ser.*, *391*, 97–106, doi:10.3354/meps08168, 2009.

Salta, M., J. a. Wharton, Y. Blache, K. R. Stokes, and J.-F. Briand, Marine biofilms on artificial surfaces: structure and dynamics., *Environ. Microbiol.*, *15*(11), 2879–2893, doi: 10.1111/1462-2920.12186, 2013.

Salter, S. H., Are nearly all tidal stream turbine designs wrong?, in *4th Int. Conf. Ocean Energy*, pp. 1–7, ICOE, Dublin, Ireland, 2012.

Schjolberg, I., and T. I. Fossen, Modelling and Control of underwater vehicle-manipulator systems, in *Conf. Mar. Cr. manuevering Control*, 1994.

Schlichting, H., *Boundary Layer Theory*, McGraw-Hill Book Company, 1955.

Shives, M., and C. Crawford, Developing an empirical model for ducted tidal turbine performance using numerical simulation results, *Proc. Inst. Mech. Eng. Part A J. Power Energy*, *226*, 112–125, doi:10.1177/0957650911417958, 2012.

Simmons, M., Chief Joseph Kokanee enhancement project; strobe light deterrent efficacy test and fish behavior determination at Grand Coulee Dam third powerplant forebay, 2005-2006 Annual Report, *Tech. rep.*, BPA Report DOE/BP - 00000652-33, 2006.

Soylu, S., B. J. Buckham, and R. P. Podhorodeski, A chattering-free sliding-mode controller

for underwater vehicles with fault-tolerant infinity-norm thrust allocation, *Ocean Eng.*, *35*, 1647–1659, doi:10.1016/j.oceaneng.2008.07.013, 2008.

Soylu, S., B. J. Buckham, and R. P. Podhorodeski, Dynamics and Control of Tethered Underwater-Manipulator Systems, in *MTS/IEEE Ocean. '10*, pp. 1–8, IEEE, doi: 10.1109/OCEANS.2010.5664366, 2010.

Steiner-Dicks, K., FAST2014, 2014.

Stoner, A. W., C. H. Ryer, S. J. Parker, P. J. Auster, and W. W. Wakefield, Evaluating the role of fish behavior in surveys conducted with underwater vehicles, *Can. J. Fish. Aquat. Sci.*, *65*, 1230–1243, doi:10.1139/F08-032, 2008.

Streeter, V. L., *Handbook of fluid dynamics*, McGraw-Hill Book Company, 1961.

Taylor, G., The statistical theory of isotropic turbulence, *J. Aeronaut. Sci.*, *4*(8), 311–315, 1937.

Thomson, J., B. Polagye, V. Durgesh, and M. C. Richmond, Measurements of turbulence at two tidal energy sites in Puget Sound, WA, *IEEE J. Ocean. Eng.*, *37*(3), 363–374, doi:10.1109/JOE.2012.2191656, 2012.

Thomson, J., L. Kilcher, M. Richmond, J. Talbert, A. DeKlerk, B. Polagye, M. Guerra, and R. Cienfuegos, Tidal turbulence spectra from a compliant mooring, in *1st Mar. Energy Technol. Symp.*, Washington, D.C., USA, 2013.

Viehman, H. a., and G. B. Zydlewski, Fish Interactions with a commercial-scale tidal energy device in the natural environment, *Estuaries and Coasts*, *38*(Suppl 1), S241–S252, doi: 10.1007/s12237-014-9767-8, 2014.

Wadoo, S. A., and P. Kachroo, *Autonomous underwater vehicles: modeling, control design, and simulation*, CRC Press, Boca Raton, FL, USA, 2011.

Wang, J.-S., and C. Lee, Self-adaptive recurrent neuro-fuzzy control of an autonomous underwater vehicle, *IEEE Trans. Robot. Autom.*, *19*(2), 283–295, doi:10.1109/TRA.2003.808865, 2003.

Westheimer, G., Three-dimensional displays and stereo vision, *Proc. Biol. Sci.*, *278*(April), 2241–2248, doi:10.1098/rspb.2010.2777, 2011.

Whelan, A., and F. Regan, Antifouling strategies for marine and riverine sensors, *J. Environ. Monit.*, *8*(9), 880–886, doi:10.1039/b603289c, 2006.

Whitcomb, L., Underwater robotics: out of the research laboratory and into the field, *Proc. 2000 ICRA. Millenn. Conf. IEEE Int. Conf. Robot. Autom. Symp. Proc. (Cat. No.00CH37065)*, *1*, doi:10.1109/ROBOT.2000.844135, 2000.

Whitcomb, L. L., and D. R. Yoerger, Preliminary experiments in model based thruster control for underwater vehicle positioning, *IEEE J. Ocean. Eng.*, *24*(4), 495–506, 1999.

Wiggins, S. M., M. a. McDonald, and J. a. Hildebrand, Beaked whale and dolphin tracking using a multichannel autonomous acoustic recorder, *J. Acoust. Soc. Am.*, *131*(1), 156–163, doi:10.1121/1.3662076, 2012.

Williams, K., C. N. Rooper, and R. Towler, Use of stereo camera systems for assessment of rockfish abundance in untrawlable areas and for recording pollock behavior during midwater trawls, *Fish. Bull.*, *108*(3), 352–362, 2010.

Williamson, B., and P. Blondel, Multibeam imaging of the environment around marine renewable energy devices, in *11th Eur. Conf. Underw. Acoust.*, pp. 1271–1277, Institute of Acoustics, St. Albans, 2012.

Williamson, B. J., P. Blondel, E. Armstrong, P. S. Bell, C. Hall, J. J. Waggitt, and B. E. Scott, A self-contained subsea platform for acoustic monitoring of the environment around marine renewable energy devices field deployments at wave and tidal energy sites in Orkney , Scotland, *IEEE J. Ocean. Eng.*, pp. 1–15, 2015.

Witt, M. J., et al., Assessing wave energy effects on biodiversity: the Wave Hub experience, *Philos. Trans. R. Soc. A Math. Phys. Eng. Sci.*, *370*, 502–529, doi:10.1098/rsta.2011.0265, 2012.

Wohler, C., *3D computer vision: efficient methods and applications*, 2nd ed ed., Springer, London, doi:http://dx.doi.org/10.1007/978-1-4471-4150-1, 2013.

Woodroffe, A. M., S. W. Pridie, and G. Druce, The NEPTUNE Canada junction box - interfacing science instruments to sub-sea cabled observatories, in *Ocean. MTS/IEEE Kobe-Techno-Ocean'08 - Voyag. Towar. Futur.*, MTS-IEEE, Kobe, Japan, doi:10.1109/OCEANSKOBE.2008.4531021, 2008.

Xu, G., and Z. Zhang, *Epipolar geometry in stereo, motion, and object recognition: a unified approach*, Kluwer Academic, Norwell, MA, doi:http://dx.doi.org/10.1007/978-94-015-8668-9, 1996.

Yoerger, D., A. Bradley, M. Jakuba, M. Tivey, C. German, T. Shank, and R. Embley, Mid-ocean ridge exploration with an autonomous underwater vehicle, *Oceanography*, *20*(4), 52–61, doi:10.5670/oceanog.2007.05, 2007.

Yoerger, D. R., J. G. Cooke, and J. J. E. Slotine, Influence of thruster dynamics on underwater vehicle behavior and their incorporation into control system design, *IEEE J. Ocean. Eng.*, *15*(3), 167–178, doi:10.1109/48.107145, 1990.

Appendix A

HYDRODYNAMIC CONDITIONS FOR TIDAL CURRENT AND WAVE ENERGY SITES

The analysis of the site conditions presented in Section A.1 has been used for the loading conditions presented in Section 5.1 and form the basis of the analysis used for Section 5.2. Modeling of four dimensional current forcing for dynamic simulations is presented in Section 5.2.2.1 and extended in Section A.2 to include alternate data sources and wave conditions.

A.1 Design Loads for Deployments and Long-Term Operation

The AMP's hydrodynamic performance is evaluated in the context of forces associated with the dominant currents at the Pacific Marine Energy Center's South Energy Test Site (PMEC-SETS) of the coast of Newport, OR and in Admiralty Inlet, WA. While PMEC-SETS will be a wave energy test site, the site experiences moderate ocean currents and, in general, the forces acting on infrastructure at either a wave or tidal energy site will be a combination of loads imposed by waves and currents. Wave orbital velocities decay exponentially with depth. For a bottom-mounted tidal turbine in deep, sheltered, inland waters, loads associated with surface waves are likely to be negligible. For a deployment in open ocean conditions, wave loads may be periodically significant, but most monitoring objectives are likely to be satisfied by a package deployed on the seabed. This analysis considers the currents likely to be encountered by the AMP during deployment and operations at either PMEC-SETS or in Admiralty Inlet.

Current data for PMEC consists of a one-month time series obtained from a surface-mounted acoustic Doppler current profiler in the fall of 2012 at a location north of PMEC-SETS. Current data for Admiralty Inlet consists of a twenty-two month time series obtained

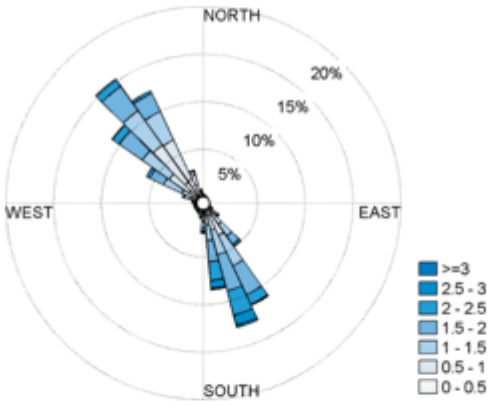

a) Admiralty Inlet mean currents (10 m above seabed)

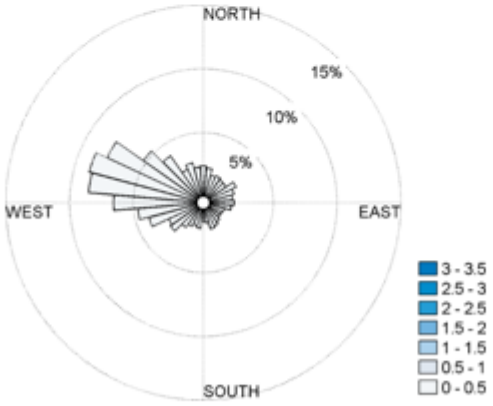

b) PMEC mean currents (2 m above seabed

Figure A.1: Mean current magnitude and direction for early adopter wave and tidal energy sites

from a bottom-mounted acoustic Doppler current profiler between fall 2011 and summer 2013 (described, in part, in *Polagye and Thomson* [2013]). The magnitude and direction of the mean (non-turbulent) currents at these two locations are shown in Figure A.1 for representative AMP deployment depths (2 m above the seabed for observations of wave converters at PMEC and 10 m above the seabed for observations of tidal converters in Admiralty Inlet). Mean sustained currents in Admiralty Inlet exceed 3 m/s and are less than 1 m/s at PMEC. For Admiralty Inlet, the maximum loads on the AMP during deployment are given by the superposition of mean currents, turbulence, and an allowance for currents in a storm surge. The maximum mean currents in Admiralty Inlet approach 4 m/s. The maximum storm surge current at this location is likely no greater than 0.4 m/s and unlikely to occur during the epoch maximum tidal currents (as a matter of probability). Consequently, a storm surge current with half this intensity is included in the design loads. Turbulence intensity in Admiralty Inlet is approximately 10% [*Thomson et al.*, 2012] meaning that turbulent perturbations up to 1.3 times the mean current velocity are probable, assuming that turbulent perturbations follow a normal distribution. These considerations lead to a design current of approximately 5.4 m/s for AMP operation (with substantially lower currents during deployment). For bottom mounted deployments of the AMP at PMEC-SETS (maximum 2 m above the seabed in a minimum of 55 m of water), operational loads will peak during extreme wave events. At PMEC-SETS the extreme wave case could be up to a 15 m wave (trough-to-crest) with a 16 s period, which would result in orbital velocities of approximately 2.3 m/s, less than half of the velocity associated with the tidal energy test site at Admiralty Inlet.

To be effectively utilized for adaptive management, hydrodynamic conditions amenable to recovery and redeployment should occur with relatively high frequency (e.g., at least one per week). For deployment at a tidal energy site, the AMP would be deployed with the currents fully set in one direction (either on a tide falling towards slack or rising towards peak currents), but with currents less than the operating limit for the deployment system. For Admiralty Inlet, if the AMP is able to operate in mean currents of at least 0.7 m/s, the

criteria for deployment window frequency can be met. This operating criterion would also allow the AMP to be deployed under most conditions at PMEC given weather conditions appropriate for surface vessel operations.

A.2 Alternate Turbulent Current Forcing Data for Dynamic Simulations

The development of turbulent current fields presented in Section 5.2.2.1 uses ADV data collected from the Admiralty Inlet tidal energy site. In the absence of site specific turbulence data sets, TurbSim, an open source turbulence simulation software maintained by the National Renewable Energy Laboratory (Golden, CO, USA), could be used to generate similar data sets [*Jonkman*, 2009; *Kelley*, 2011]. Given turbulence statistics for a marine energy site, TurbSim will generate a time-varying current grid with the number of vertices defined by the user. The resulting dataset are converted to a four dimensional forcing input field by applying the grid vertices to the $y - z$ plane and propagating the frozen turbulence field downstream (negative x direction) as with the ADV data from Admiralty Inlet (Section 5.2.2.1).

Wave orbital velocities are not included in the simulations for Admiralty Inlet as their contribution is negligible at the anticipated depth of operations ($\sim$50 m). As this is not the case for all marine energy sites, it is important to note that wave models may be added to the ProteusDS simulations by way of adding orbital velocities to the prescribed current field. Given basic wave spectrum statistics (e.g., wave heading, period, and height), the corresponding orbital velocities may be added to the turbulent currents in the simulations. Modeling environmental conditions with both wave and current features allows the contributions of each case to be evaluated and compared.

Appendix B

DESIGN OPTIMIZATIONS THROUGH CFD DRAG ANALYSIS

Initial optimization of the AMP and Millennium Falcon ROV design relied on steady-state CFD simulations to determine drag forces during deployments and long-term operation. The design condition for system deployment was assumed to be a head-on mean relative velocity of 1 m/s with turbulence intensity of 15% and a 1 m dominant length-scale[a]. For operational monitoring at a tidal energy site, the AMP will be exposed to much stronger currents, with turbulent peaks up to 5.4 m/s. The force of these currents on the AMP body drives the design loads for the docking clamp and the AMP's internal structure. Optimization could include adjusting the shape of different AMP components to reduce the cross-sectional area exposed to the strongest currents or incorporating passive farings that reduce form drag by aligning with the direction of the mean currents.

B.0.1 Methods

CFD modelling of the system followed the same procedural methods as for the Falcon ROV described in Section 5.1.2.2. Solid models of all the instrumentation, AMP support structure, and shroud were used to calculate the center of mass and center of buoyancy (or volume). CFD simulations were used to calculate lift and drag coefficients and obtain the center of pressure. The lift and drag coefficients, C_l and C_d, for the various components are calculated as

[a]In practice, the dominant length scale for turbulence at tidal current sites is on the order of 10's of meters [*Thomson et al.*, 2012].

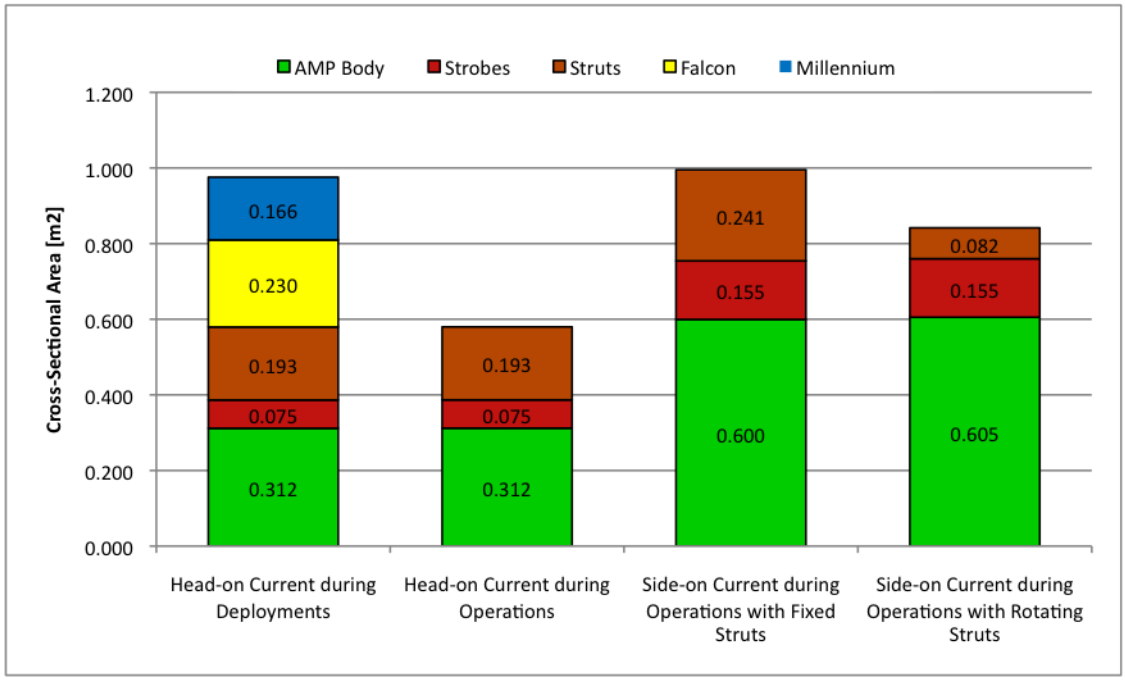

Figure B.1: Component cross-sectional areas for flow simulations

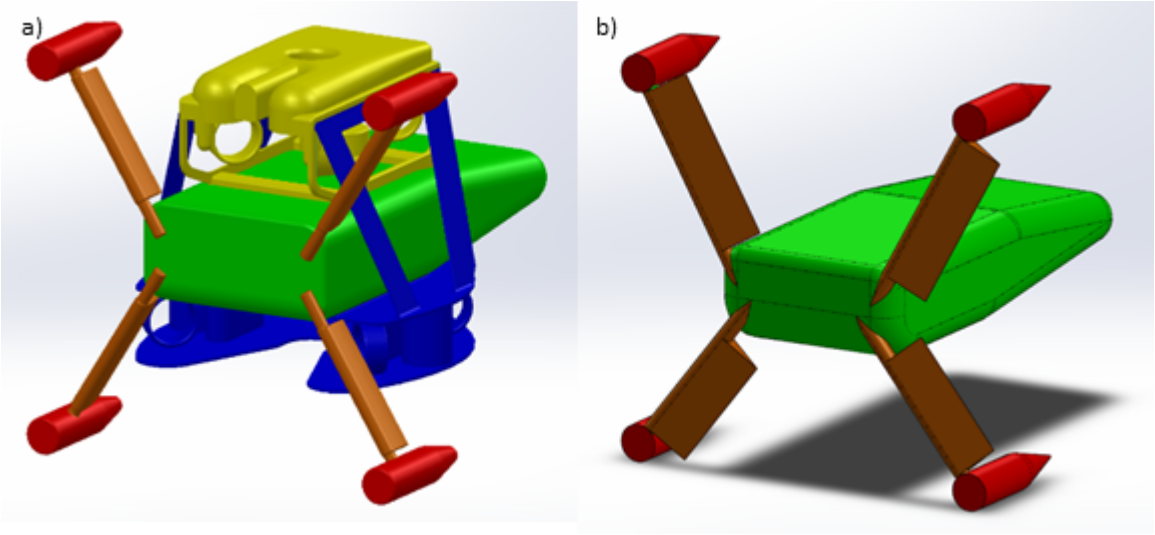

Figure B.2: Simplified AMP and Millennium Falcon geometries for CFD with colors indicating separate components (yellow for Falcon, blue for Millennium, green for AMP body, orange for struts, and red for strobes) (a) for deployment simulations and (b) with rotated strut farings for side-on current during docked operations

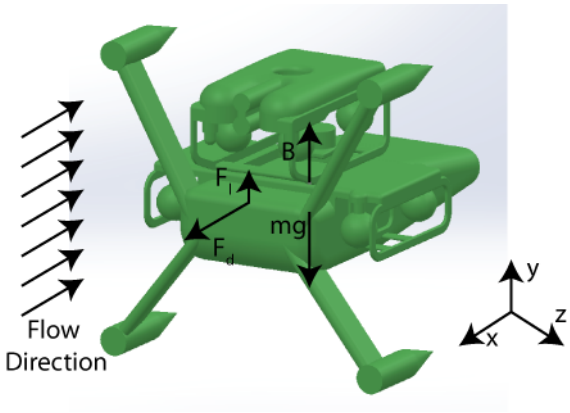

Figure B.3: System free body diagram with approximate locations of lift, drag, buoyancy, and mass forces

$$C_l = 2F_l/\rho AU^2 \tag{B.1}$$

$$C_d = 2F_d/\rho AU^2 \tag{B.2}$$

where F_l and F_d are the lift and drag forces, ρ is the fluid density, A is the cross sectional area normal to the flow, and U is the mean fluid flow velocity. Cross-sectional areas used in the calculation of lift and drag coefficients are provided in Figure B.1 for each of the simulation models and broken down into the five primary system components shown in Figure B.2: the Falcon, the Millennium, the central AMP body, the strobes, and the strobe support struts. Figure B.3 illustrates the location and direction of the lift, drag, buoyancy and mass forces in the case of a head-on fluid flow. An analysis of the centers of buoyancy, pressure, and thrust is used to estimate system stability prior to performing dynamic simulations.

For this initial design optimization, the modeling results were used to compare design features and to understand how the drag forces on various components (e.g., strobes, struts, and AMP body) interact when exposed to the design currents. As a case study for system optimization, CFD simulations were performed for a head-on and side-on flow of the AMP, spanning the range of mounting options during monitoring missions. For the side-on flow case, the faring on the strobe struts was modeled as fixed, as shown in Figure B.2a, or passively aligned with the flow, as in Figure B.2b.

B.0.2 Results and Discussion

CFD visualizations of the normalized flow velocity and total pressure for a 1 m/s head-on mean flow over the Millennium Falcon and AMP are shown in Figure B.4. The flow over the surfaces of the system in Figure B.4a shows a large eddy forming in the wake of the Millennium Falcon and around the edge of the strobe faces. This flow separation is a significant source of drag on the system. Flow over the fared struts, however, shows little to no separation. The high pressure on the frontal faces of the system shown in Figure B.4b indicates the location of form drag which may be reduced through increased faring of these

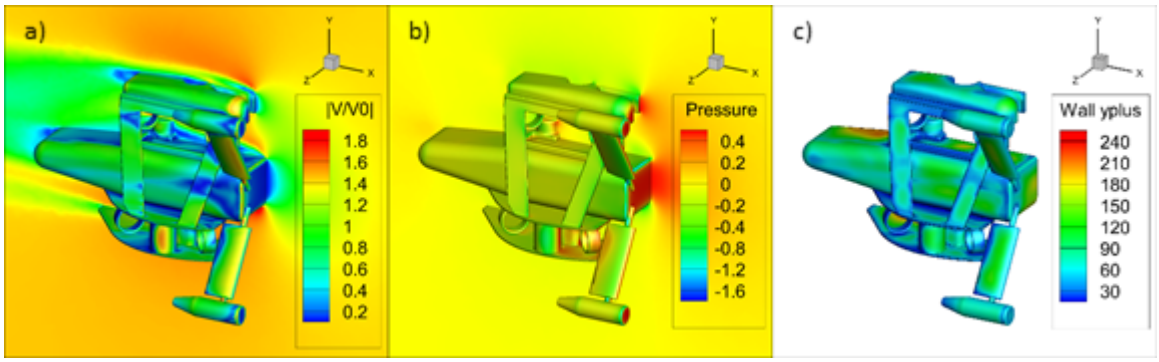

Figure B.4: CFD simulation results for a head-on current of 1 m/s on the Millennium Falcon and AMP with (a) normalized velocity over the body surfaces, (b) total pressure [Pa] on the body surfaces, and (c) wall y^+ values on the body surfaces

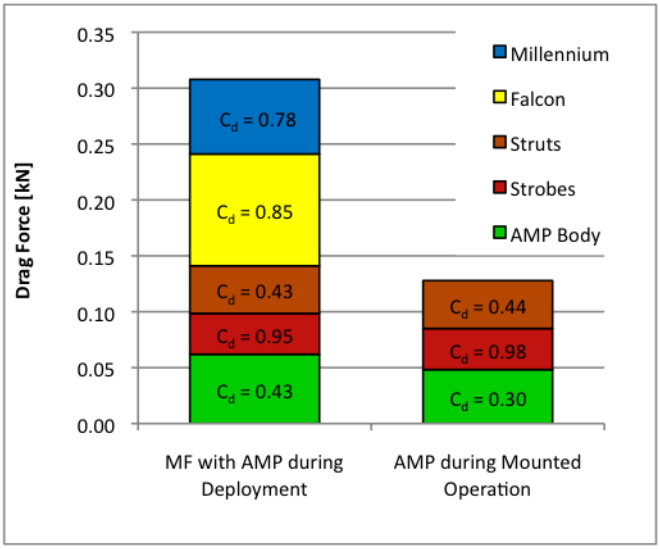

Figure B.5: Drag force and coefficient for the AMP and Millennium Falcon during deployments and mounted operations in a 1 m/s current

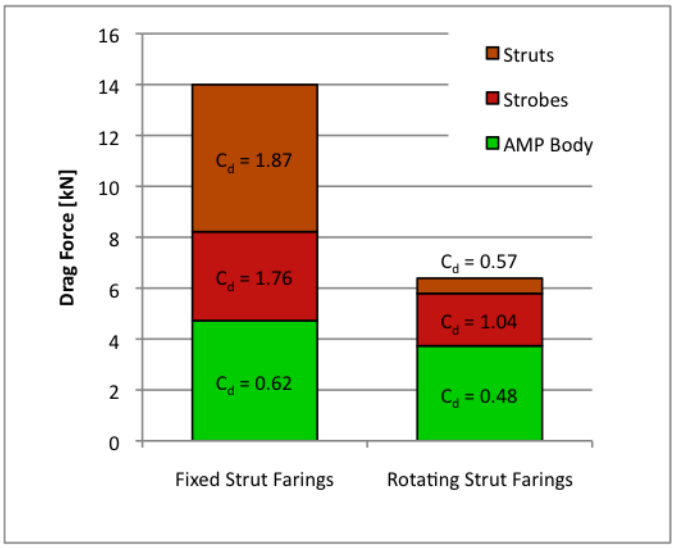

Figure B.6: Drag force and coefficients for a side-on current of 5 m/s over the mounted AMP during operation with fixed or rotating struts

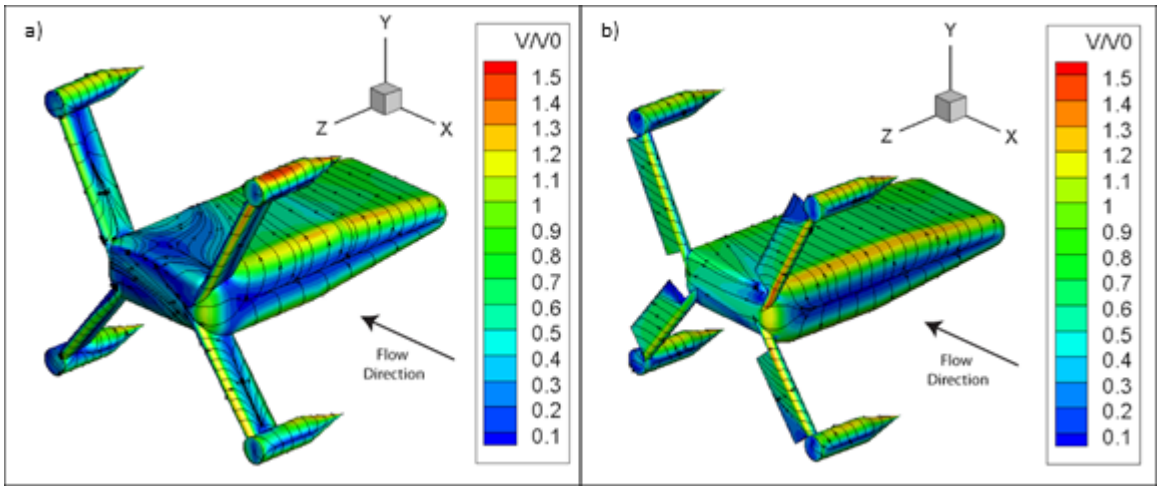

Figure B.7: Optimization case study for a side-on flow over the AMP showing normalized velocity with streamlines for the AMP with (a) fixed strut farings and (b) rotating strut farings

surfaces. The lift forces calculated in these simulations were negligible and within the range of error since all of the modeled conditions were either a head-on or side-on flow.

The total estimated system drag coefficient is 0.67 for deployment operations. To better understand the drag contributions of the individual components, the forces acting on the associated surfaces are shown in Figure B.5 for the AMP in a head-on current of 1 m/s both during deployments with the Millennium Falcon and during mounted operation. It is notable that the draft force on the AMP body is significantly decreased when the Millennium Falcon is disengaged due to the interaction between these sub-systems.

The case study analysis for the AMP during docked operation in 5 m/s currents is summarized in Figure B.6 and indicates a reduction in drag forces of up 54% for the case of side-on current by allowing the strut faring to rotate. Normalized velocity over the AMP bodies for a side-on flow in the negative x direction is visualized in Figure B.7, showing a greater decrease in flow behind the fixed strut faring than the rotating strut faring. The combination of the increased form drag and the increased cross-sectional area of the fixed struts magnifies the drag of this component by 9.6 times when compared to the rotating farings. Similarly to the interaction between the AMP body and the Millennium Falcon, allowing the faring to rotate reduces the drag forces on the strobes and AMP body by reducing blockage at the points where the struts connect.

B.0.3 Conclusion

Comparison of numerical simulations to evaluate design options can assist in system optimization without physical prototyping. The case study of the faring on the strobe struts shows that the drag forces on the AMP during docked operation may be reduced up to 54% by allowing the faring to rotate with the current. This reduction is greater than the individual drag contribution of the struts because the drag forces on the AMP body and the strobes are similarly reduced due to interactions between the components.